UNIVERSITY OF CALIFORNIA
RIVERSIDE

Manipulation and Electrical Detection of the Néel Vector in Magnetoelectric Antiferromagnet Heterostructures for Advanced Spintronics

A Dissertation submitted in partial satisfaction
of the requirements for the degree of

Doctor of Philosophy

in

Physics

by

Wei-Cheng Liao

December 2025

Dissertation Committee:
Dr. Jing Shi, Chairperson
Dr. Igor Barsukov
Dr. Peng Wei

Copyright by
Wei-Cheng Liao
2025

The Dissertation of Wei-Cheng Liao is approved:

Committee Chairperson

University of California, Riverside

ACKNOWLEDGEMENTS

The pursuit of a PhD is a long and challenging journey. I lost count of how many times I felt overwhelmed or doubted whether I could make it to the end. What ultimately carried me through was the support and encouragement of the many people I met along the way. Without all of you, I would not have reached this milestone.

First and foremost, I would like to express my deepest gratitude to my PhD advisor, Dr. Jing Shi. He has consistently been available to support me, offering guidance whenever I encounter obstacles. He not only advised me on research and coursework, but also supported me on grant applications, job searches, family, life, and much more. He embodies the qualities of a true scientist: deep expertise, rigorous thinking, intellectual curiosity, and thoughtful judgement. His example has profoundly shaped my growth as a researcher and as a person.

I would like to express my sincere appreciation to the members of my dissertation committee, Dr. Igor Barsukov and Dr. Peng Wei, for their insightful and constructive feedback, which greatly strengthened and broadened my research and dissertation. I am also grateful to Dr. Vivek Aji and Dr. Alexander Balandin for generously dedicating their time to serve on my oral exam committee.

I would also like to extend my heartfelt thanks to the former PhD students and postdoc researchers who generously shared their expertise with me. They are Dr. Mark Lohmann, Dr. Mohammed Alghamdi, Dr. Junxue Li, Dr. Wei Yuan, Dr. Mina Rashetnia, Dr. Jacky Wan, and Jonathan Turner. Their guidance in fabrication techniques and

measurement methods laid the foundation for my research and helped me grow into an independent experimentalist. I am deeply grateful for the time, patience, and knowledge they invested in my training.

I would like to give special appreciation to my labmates, Dr. Haoyu Liu, Josiah Keagy, Jia-Mou Chen, and Weilun Tan. Over the years, we worked side-by-side, supported each other, ran into troubles, and overcame countless obstacles. I truly cherish the time we spent working together. The completion of my dissertation is not solely my achievements, but genuinely a shared effort with all of you.

I‘m also thankful to other PhD students I met along the journey, Dr. Ming-Feng Ho, Dr. Chia-Wei Liu, Dr. Chia-Feng Chang, Dr. Wei-Xiang Feng, En-De Chu, Yen-Wen Lu, Dr. Li-Ren Liu, Dr. Zong-Jhen Ye, and many other people I cannot list all here for their friendship and kind help in all aspects of my PhD that has meant a great deal to me.

I am grateful to my collaborators both at UCR and from other institutions. I would like to thank Dr. Boniface Fokwa, Dr. Pingyun Feng, and their students for their work on the synthesis of rare-earth-free magnetic materials and metal–organic frameworks; Dr. Sinisa Coh for his theoretical works and calculations; Dr. Igor Barsukov and his students, Rundong Jiang and Alexandra Korotneva, for the Cr_2O_3 spin simulations and valuable discussions; Dr. Ran Cheng and his student Dr. Hantao Zhang for valuable discussions. I also appreciate the support of Dr. Yongtao Cui and his students with atomic force microscopy. My thanks extend to Dr. Peng Wei, Dr. Andrew Joe, Dr. Nathaniel Gabor, Dr. Joshua Lui, Dr. Ward Beyermann, Dr. Richard Wilson, and their students for all experimental and technical support. I am grateful to Dr. Jhen-Yong Hong and his student

Chun-Yen Chen from Tamkang University for the XMCD and XMLD measurements, and to Dr. Yinming Shao from the Pennsylvania State University for the scanning near-field optical measurements.

I want to thank Dr. Dong Yan for his invaluable assistance with the nanofabrication aspects of my PhD research. I am also thankful to Dr. Derek Beving, as well as the many staff members and faculty in the Department of Physics and Astronomy at UCR, for their support and the help they provided throughout my studies.

I would like to thank all the teachers and staff at the UCR Center for Early Childhood Education for taking such good care of my child and supporting his early learning. I am also grateful to the members of the Holy Son's Love Church and The Grove Community Church in Riverside for the support they have given to my family's life and faith.

I am truly fortunate to have a warm and caring family who has always supported me in pursuing my goals. I wish to extend my heartfelt thanks to my mother, father, brother, sister, mother-in-law, father-in-law, brother-in-law, and sister-in-law for providing the emotional and financial support that sustained me throughout the many years of my academic journey.

Most importantly, I want to express my deepest love and appreciation to my wife, Jou-Hsuan Chiang, and my son, Daniel Liao. Your love and support have motivated me to become a better person. I could not have reached this point without you, and I am deeply grateful for all the sacrifices you have made. I love you, and I look forward to embracing the next chapter of life together with you.

ABSTRACT OF THE DISSERTATION

Manipulation and Electrical Detection of the Néel Vector in Magnetoelectric Antiferromagnet Heterostructures for Advanced Spintronics

by

Wei-Cheng Liao

Doctor of Philosophy, Graduate Program in Physics
University of California, Riverside, December 2025
Dr. Jing Shi, Chairperson

Antiferromagnetic (AFM) materials offer exciting opportunities for spintronic applications, yet the absence of net magnetization fundamentally hinders both the manipulation and detection of their order parameter, the Néel vector, compared to the ferromagnetic and ferrimagnetic counterparts. The coupling between electric and magnetic orders, known as the magnetoelectric effect, provides a promising route to control and detect the Néel vector electrically.

In my dissertation, I present studies on heterostructures based on magnetoelectric antiferromagnets, including Cr_2O_3 and the two-dimensional (2D) van der Waals material $MnPS_3$. In Cr_2O_3, we investigate the electrical detection of the Néel vector across the spin-flop transition in adjacent Pt layers, enabling a clear separation of multiple spin transport contributions. We further demonstrate electrical control of the Néel vector through linear magnetoelectric coupling, realizing an analog of electrical read/write operations in a

functional AFM-based memory device. For epitaxial Cr_2O_3 thin films grown by pulsed laser deposition, the top and bottom Pt Hall sensing layers exhibit inverted hysteresis loops, reflecting Néel vector reversal driven only by an external magnetic field, with a distinct thickness-dependent crossover behavior.

Finally, I present preliminary results on two types of heterostructures containing antiferromagnetic $MnPS_3$, i.e., $MnPS_3$/Pt and $WTe_2/MnPS_3$, where $MnPS_3$ imprints its magnetism on the anomalous Hall effect in Pt layers and on the quantum oscillations in the 2D Weyl semimetal WTe_2. Collectively, these studies advance our understanding of spin transport signatures and magnetoelectric coupling associated with the Néel vector in AFM systems spanning bulk crystals, epitaxial films, and 2D materials, highlighting the promise of magnetoelectric antiferromagnets for advanced spintronic devices.

TABLE OF CONTENTS

Chapter 1 Introduction 1
1.1 A Historic Overview of Spintronics 2
1.2 Spin Transport and Interfacial Phenomena 10
1.2.1 Anomalous Hall Effect 10
1.2.2 Magnetic Proximity Effect 16
1.2.3 Spin Hall Effect and Spin Hall Magnetoresistance 20
1.2.4 Exchange Bias 23
1.3 Antiferromagnetic Spintronic 24
1.3.1 Current-Driven Electrical Switching 25
1.3.2 Long-Range Nonlocal Spin Transport 26
1.3.3 Sub-THz Spin Pumping 27
1.3.4 Magnetoelectric Control of the Néel Vector 28
1.4 Properties and Dynamics of Uniaxial Antiferromagnets 30
1.4.1 Néel Vector 31
1.4.2 Spin-Flop Transition 32
1.4.3 Dynamics and Resonance 34
Chapter 2 Electrical Detection of Single-Domain Néel Vector Reorientation across the Spin-Flop Transition in Cr_2O_3 Crystals 37
2.1 Background and Motivation 38
2.2 Methods 39
2.3 Spin Seebeck and Magnetoresistance at Spin-Flop Transition 40
2.4 Hall Detection of the Néel Vector 43
2.4.1 Hall Resistance in $50\mu m \times 50\mu m$ Active Area 44
2.4.2 Hall Resistance in $10\mu m \times 10\mu m$ Active Area 47
2.4.3 Controlling Néel Vector by Field Cooling and Magnetoelectric Coupling 51
2.4.4 Temperature Dependance of AHE and PHE 53
2.5 Summary 55
2.6 Supporting Information 56
2.6.1 Magnetometry Characterization of Cr_2O_3 Bulk Single Crystal 56
2.6.2 Fabrication and Characterization of $Cr_2O_3(1010)$/Pt Heterostructures 58
2.6.3 Fabrication and Characterization of $Cr_2O_3(0001)$/Pt Heterostructures 59

2.6.4 Magnetoresistance and Hall Measurements 60
2.6.5 Spin Seebeck Effect Measurements 62
2.6.6 Temperature Dependence of Magnetostriction Effect 63
2.6.7 Planar Hall Effect and Geometry-Induced Mixing Signals 64
2.6.8 A Brief Summary of the Hall Resistance 66
2.6.9 On the Anomaly in AHE 68
Chapter 3 Dual Ferromagnetic and Ferroelectric Dynamics in Linear Magnetoelectric Cr_2O_3 70
3.1 Background and Motivation 71
3.2 Methods 73
3.3 Néel Vector Controlled by Magnetoelectric Annealing 74
3.4 Néel Vector Switching in FM-Like Mode 77
3.5 Néel Vector Switching in FE-like Mode 82
3.6 Mode-Dependent Dynamics and Energy of the Néel Vector 84
3.7 Summary 88
3.8 Discussions 89
3.8.1 Linear Magnetoelectric Effect in Cr_2O_3 89
3.8.2 Estimation of Magnetoelectric Threshold for Coherent Switching 93
3.8.3 Comparison of Magnetoelectric Threshold Energy 94
Chapter 4 Temperature and Thickness Dependence of The Anomalous Hall Effect in Epitaxial Cr_2O_3 and Pt Heterostructures 96
4.1 Background and Motivation 97
4.2 Epitaxial Growth of Cr_2O_3(0001) Thin Films 98
4.3 AHE in Cr_2O_3/Pt (Top Detector) 101
4.4 AHE in Pt/Cr_2O_3/Pt (Both Top and Bottom Detectors) 103
4.5 Thickness and Temperature Dependence of AHE 106
4.6 Crossover Behavior of Anomalous Hall Hysteresis 112
4.7 Summary 117
4.8 Supporting Information 118
4.8.1 Pulsed Laser Deposition and Reflective High Energy Electron Diffraction 118
4.8.2 Device Fabrication 120
4.8.3 Spin-Flop Transition in Epitaxial Cr_2O_3 Thin Films 121
4.8.4 Simulation Details 122

4.8.5 Magnetometry Characterization on Epitaxial Cr_2O_3 Thin Film 123
4.8.6 Magnetoelectric Effect in Cr_2O_3 Thin Films 125
Chapter 5 Probing Magnetism and Proximity Phenomena in 2D Antiferromagnetic $MnPS_3$ Heterostructures 128
5.1 Motivation and Background 129
5.2 Magnetic Properties of $MnPS_3$ Bulk Crystal 130
5.3 Fabrication of $MnPS_3$ Heterostructure Devices 131
5.4 Magnetoresistance and AHE in $MnPS_3$/Pt 132
5.5 Quantum Oscillations in WTe_2/$MnPS_3$ 136
5.6 Summary 139
5.7 Supporting Information 140
5.7.1 2D Materials Exfoliation and Stacking Techniques 140
5.7.2 Comparison of AHE Between Cr_2O_3/Pt and $MnPS_3$/Pt 141
5.7.3 Determination of Carrier Mobility from Quantum Oscillations 142

LIST OF FIGURES

Figure 1.1 First-Generation “Toggle MRAM” 4

Figure 1.2 CoFeB/MgO/CoFeB MTJ Device 6

Figure 1.3 Datta–Das Spin FET and Domain-Wall Racetrack Memory 9

Figure 1.4 AHE for Two-Dimensional Van Der Waals Ferromagnets 11

Figure 1.5 Three Main Mechanisms for AHE 13

Figure 1.6 AHE Conductivity in Different Conductivity Regimes 14

Figure 1.7 Different Mechanisms for AHE in HM/MI Bilayers 17

Figure 1.8 AHE in Graphene/YIG Heterostructure 19

Figure 1.9 Spin Hall Magnetoresistance 22

Figure 1.10 Exchange Bias in FM/AFM 23

Figure 1.11 Electrical Switching of the Antiferromagnet CuMnAs 26

Figure 1.12 Electrical Detection of Néel Vector in Cr_2O_3 29

Figure 1.13 Different Types of Magnetic Order 30

Figure 1.14 Phase Diagram of Spin-Flop Transition 33

Figure 1.15 AFM Resonance in Cr_2O_3 36

Figure 2.1 Spin-flop Transition of $Cr_2O_3(\mathbf{10\bar{1}0})$ Crystal 42

Figure 2.2 Hall Resistance of Cr_2O_3(0001)/Pt in 50μm×50μm Active Area 46

Figure 2.3 Hall Resistance of Cr_2O_3(0001)/Pt in 10μm×10μm Active Area 50

Figure 2.4 Néel Vector Orientations under Different Conditions 52

Figure 2.5 Temperature Dependence of AHE and PHE 54

Figure 2.6 Magnetometry Characterization of the (0001)-Oriented Cr_2O_3 Single Crystal 57

Figure 2.7 Fabrication and Characterization of $Cr_2O_3(\mathbf{10\bar{1}0})$/Pt Heterostructures 58

Figure 2.8 Fabrication and Characterization of Cr_2O_3(0001)/Pt Heterostructures.....60

Figure 2.9 Physical Properties Measurements System.....61

Figure 2.10 Spin Seebeck Measurements.....62

Figure 2.11 Temperature Dependence of Magnetostriction Effect.....63

Figure 2.12 Comparison Between R_{xx} and R_{PHE}.....65

Figure 2.13 A Brief Summary of the Hall Resistance.....67

Figure 2.14 Temperature Dependence of R_{AHE_A}.....69

Figure 3.1 Magnetoelectric Annealing Experiments.....75

Figure 3.2 Isothermal Switching of the Néel Vector.....78

Figure 3.3 Magnetoelectric Switching for FM-Like Mode.....81

Figure 3.4 FE-Like Néel Vector Switching.....83

Figure 3.5 Dynamics and Energy of FM-Like and FE-Like Switching.....85

Figure 3.6 The Crystal and Spin Structure of Cr_2O_3 in the AFM Phase.....90

Figure 3.7 Temperature Dependence of the $\alpha_{\parallel}$ and $\alpha_{\perp}$ in Cr_2O_3.....92

Figure 4.1 Structural Characterization of $Al_2O_3(\mathbf{0001})/Cr_2O_3$.....99

Figure 4.2 Structural Characterization of Al_2O_3(0001)/Pt/Cr_2O_3.....100

Figure 4.4 Anomalous Hall Effect of Cr_2O_3/Pt.....102

Figure 4.5 Anomalous Hall Effect in Pt/Cr_2O_3/Pt.....105

Figure 4.6 R_{AHE} Loops for Cr_2O_3 Samples with Different Layer Thickness.....108

Figure 4.7 Temperature and Thickness Dependence of R_{AHE} and H_c.....110

Figure 4.8 Ferrimagnetism in Cr_2O_3 Thin Film.....113

Figure 4.9 Macrospin Simulations with DMI.....116

Figure 4.10 Pulsed Laser Deposition (PLD) and Reflection High Energy Electron Diffraction (RHEED).....119

Figure 4.11 Spin-Flop Transition in Cr_2O_3 Thin Film.....121

Figure 4.12 Simulation Detail.....122

Figure 4.13 Magnetometry Characterization of 600 nm Cr_2O_3 Thin Film.....124

Figure 4.14 Magnetoelectric Effect and Spontaneous Ferrimagnetism in Cr_2O_3 Thin Films.....127

Figure 5.1 Magnetic Properties of $MnPS_3$ Single Crystal.....130

Figure 5.2 Comparison Between Pt and $MnPS_3$/Pt Magnetoresistance and Hall.....132

Figure 5.3 Magnetoresistance of the $MnPS_3$/Pt Device Measured at T = 10 K.....133

Figure 5.4 Anomalous Hall Effect in $MnPS_3$/Pt.....135

Figure 5.5 Magnetoresistance and SdH Oscillations in $WTe_2/MnPS_3$.....136

Figure 5.6 Proximity-Enhanced Quantum Oscillations in $WTe_2/MnPS_3$.....138

Figure 5.7 Comparison Between AHE in Cr_2O_3/Pt and $MnPS_3$/Pt.....141

Figure 5.8 Determination of Carrier Mobility.....142

Chapter 1 Introduction

Antiferromagnets have recently emerged as promising candidates for spintronic applications due to their ultrafast spin dynamics, robustness against external magnetic fields, and absence of stray magnetic fields, which can enable high-density, high-speed, and energy-efficient devices. Meanwhile, the linear magnetoelectric effect provides a potential pathway for low-power manipulation and detection of the Néel vector in certain AFMs.

A Particular emphasis of this dissertation is placed on the antiferromagnetic order parameter, the Néel vector, and its imprint on interfacial spin transport phenomena when magnetoelectric antiferromagnets form heterostructures with certain sensing materials. Such interfacial coupling governs key effects such as exchange bias, spin Hall magnetoresistance, and proximity-induced magnetism, thereby linking the Néel vector orientation to macroscopic electrical observables. The overarching goal of this dissertation is to elucidate how these interactions can be harnessed and engineered to realize future spintronic technologies.

In this introductory chapter, I provide an overview of the broader background of spintronics, together with the fundamental concepts required to understand antiferromagnetism, the linear magnetoelectric effect, and their associated spin transport phenomena.

1.1 A Historic Overview of Spintronics

Spintronics, or spin electronics, is a vital subfield of condensed matter physics that goes beyond the paradigm of charge-based electronics by exploiting the intrinsic spin degree of freedom of electrons. While traditional electronic devices rely solely on charge transport, spintronic systems seek to manipulate both charge and spin to enable new paradigms of information processing and storage.

The historical foundation of spintronics can be traced back to the study of magneto-transport phenomena in the 19th century. William Thomson (Lord Kelvin) first reported the change in resistance of a metal under the presence of external magnetic fields, known as magnetoresistance (MR) effect in 1857 [1]. His observation includes both ordinary magnetoresistance (OMR) in non-magnetic metals and anisotropic magnetoresistance (AMR) in ferromagnets. Later, Edwin H. Hall discovered the transverse voltage in normal metal now known as the ordinary Hall effect (OHE) in 1879 [2], and the anomalous Hall effect (AHE) in ferromagnet in 1881 [3]. These early findings revealed an important connection between magnetism and electrical conduction.

While the OMR and the OHE can be explained by charge orbital motion in a magnetic field, a spin-based theoretical framework was provided by Nevill F. Mott in 1930s [4]. Mott's two-current model introduced the fundamental concept of spin-polarized current and spin-dependent scattering by providing a microscopic picture to explain how the resistivity of a ferromagnet depends on the distinct scattering rates of majority and minority spins. His pioneering work is essential to the modern understanding of spin-

dependent transport phenomena like the AMR in ferromagnet metals and laid the groundwork for the discoveries that would launch spintronics in the late 20th century.

Since the discovery of MR, the resistance change has been limited to a few percent for over a century [5]. In 1988, the giant magnetoresistance (GMR) effect was independently discovered by Albert Fert et al. and Peter Grünberg et al. in Fe/Cr magnetic multilayer structures and Fe/Cr/Fe trilayer structures [6,7]. The enormous resistance changes relative to conventional MR, depending on the alignment of the spin orientation in adjacent magnetic layers, enabled practical applications and marked the birth of spintronics. The achievement was later recognized by the 2007 Nobel Prize in Physics awarded to Fert and Grünberg.

Following the discovery of GMR, spin-valve devices using nonmagnetic metal as a spacer in ferromagnet/metal/ferromagnet structures were rapidly developed and optimized throughout the 1990s for practical applications. As an important progress, Stuart S. P. Parkin et al. introduced pinned magnetic layers through exchange bias and synthetic antiferromagnetic reference structures [8]. The resulting GMR spin-valve read sensors revolutionized magnetic recording, leading to an exponential increase in hard disk storage density.

Parallel progress occurred in tunnel magnetoresistance (TMR), which employs magnetic tunnel junctions (MTJs), a ferromagnet/insulator/ferromagnet structure to replace the spacer in spin-valve device with an insulating tunnel barrier. Though the basic TMR effect was first observed by Jullière in 1975 [9], the critical breakthrough of room-temperature high TMR were experimentally realized two decades later using amorphous

Al_2O_3 barriers, led by J. Moodera et al. at MIT [10] and T. Miyazaki et al. at Tohoku University [11]. This discovery was quickly adopted by semiconductor companies for the development of magnetoresistive random access memory (MRAM) [12,13]. In 1998-1999, Motorola demonstrated the first 256 Kb MRAM test chip based on Al_2O_3 MTJs. In 2006, Freescale Semiconductor, a spin-off from Motorola, introduced the first commercial 4-Mbit MRAM product. This first-generation MRAM, known as Toggle MRAM (see **Figure 1.1**), employed external magnetic fields from copper bit lines to switch the magnetic state of the MTJ free-layer, which limited its power consumption and scalability [12,13].

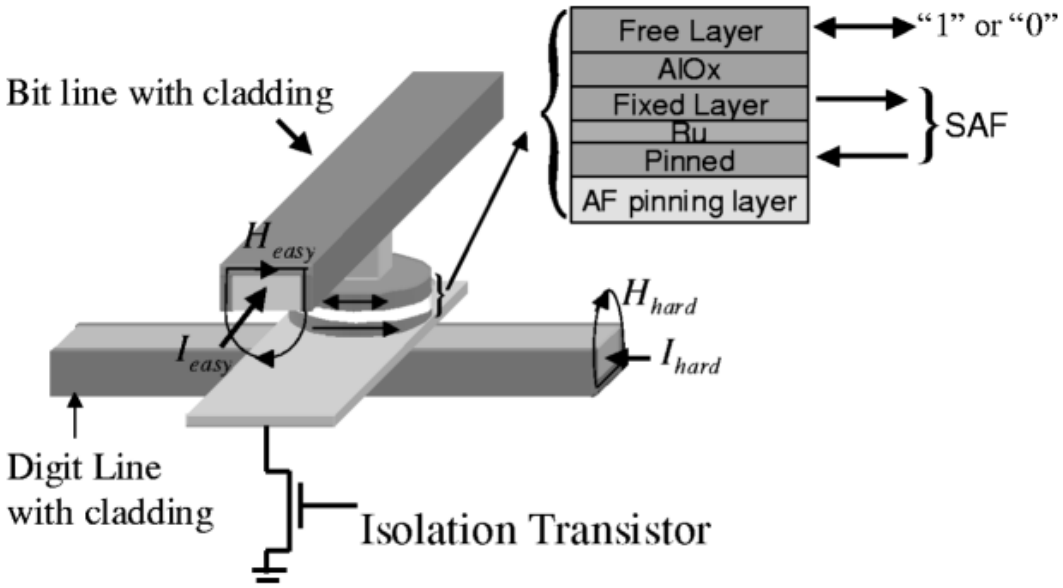


Figure 1.1 First-Generation "Toggle MRAM" Copper bit line is used to generate magnetic field for information writing. Reproduced from Ref. [13].

A major advance came with the realization of spin-transfer torque (STT). The concept of STT was introduced in 1996, when John C. Slonczewski and Luc Berger independently proposed that a spin-polarized current could exert a torque on a magnetization, enabling current-driven magnetization reversal [14,15]. Experimental demonstrations of STT switching in magnetic nanopillars [16,17] and MTJs [18,19] followed soon after. In parallel, coherent tunneling through crystalline MgO barriers was predicted [20] and demonstrated [21,22], leading to TMR ratios exceeding several hundred percent at room temperature. MgO-based MTJs not only replaced GMR sensors in read heads but also became the foundation of the second-generation MRAM, known as STT-MRAM.

STT-MRAM represents one of the most important and mature technological achievements in spintronics, marking the successful translation of spintronic concepts from fundamental research to large-scale commercial applications. Owing to its nonvolatile nature, high endurance, and low power consumption, STT-MRAM has the potential to compete with mainstream memory technologies such as DRAM, SRAM, and Flash. In 2010, S. Ikeda and H. Ohno et al. demonstrated the first CoFeB-MgO MTJs (**Figure 1.2**) with perpendicular magnetic anisotropy (PMA) and low switching current [23]. This achievement established the first reliable, scalable, and CMOS-compatible prototype of STT-MRAM. Since then, both IBM and Everspin Technologies (a spin-off from Freescale) have played key roles in the following development and commercialization.

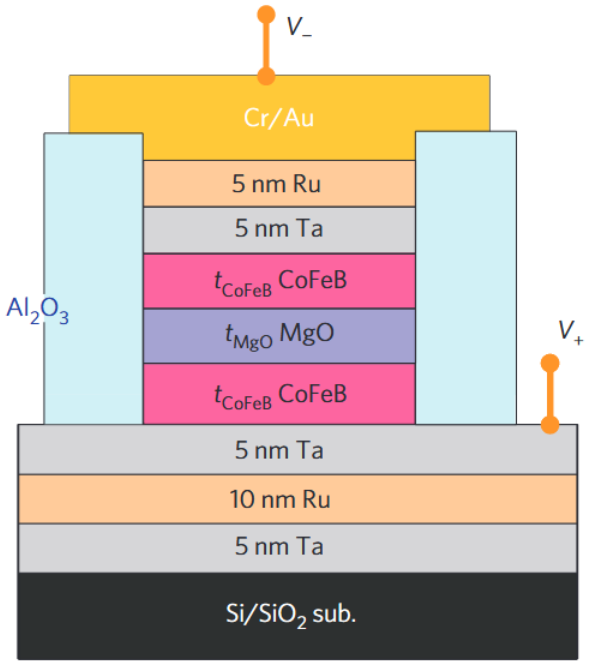


Figure 1.2 CoFeB/MgO/CoFeB MTJ Device This device architecture forms the core element of STT-MRAM. Reproduced from Ref. [23].

In recent years, attention has turned to spin current generation and manipulation by spin–orbit coupling (SOC), giving rise to the area known as spin–orbitronics. In these systems, transverse spin currents are generated through the spin Hall effect (SHE) by injecting charge currents into nonmagnetic heavy metals such as Pt, Ta, or W. The SHE was first proposed by Dyakonov and Perel in 1971 [24] and revisited in 1999 [25], with experimental observations in semiconductors [26,27] and metals [28,29] in the 2000s. These milestones established the charge–spin interconversion as a universal phenomenon, extending spin transport beyond the boundaries of ferromagnet.

Clearly distinct from STT, the ability of the SHE to generate spin currents from charge flow enabled magnetization switching by the spin-orbit torque (SOT) [30] without charge current passing through the magnetic layer itself. In this process, a spin current

produced in a heavy metal by the SHE diffuses into an adjacent ferromagnetic layer, where the resulting torque can tilt or reverse its magnetization. This effect was experimentally demonstrated by I. M. Miron *et al.* in Pt/Co/AlOx structures in 2011 [31] and by L. Liu *et al.* in Ta/CoFeB/MgO in 2012 [32], and later in 2D magnet such as Fe_3GeTe_2 [33,34]. Beyond manipulation, SHE has also been harnessed to probe insulating magnets through effects known as the spin Hall magnetoresistance (SMR), first reported in yttrium iron garnet (YIG) and Pt bilayer systems in 2013 [35]. In SMR, spin accumulation at the interface depends sensitively on the magnetization direction of the insulator, allowing electrical detection of spin orientation in magnetic insulators.

The exploration of spin–orbitronics also revolutionized the field known as magnonics, effectively folding it into the broader spintronic family. Magnonics studies the generation, propagation, and manipulation of collective spin oscillations known as spin waves or magnons in magnetic materials. The field originated from classical magnetism and microwave physics in the mid-20th century, when researchers investigated ferromagnetic resonance and spin wave dynamics [36,37]. For decades, magnonics remained largely decoupled from charge-based electronics, focusing instead on wave-based information transport in magnetic insulators. The resurgence of interest came with the discoveries of the spin pumping [38,39], SHE [26] and its inverse counterpart [40], and spin Seebeck effect (SSE) [41]. Recent studies have shown efficient generation and electrical detection of antiferromagnetic magnons [42,43] and magnetization switching through magnon-mediated spin torque [44]. These findings unified spintronics and

magnonics, bridging charge, spin, and collective excitations for future low-power information technologies.

The evolution of spintronics continues to inspire a wide range of emerging concepts and device architectures. Proposals such as the Datta–Das spin field-effect transistor [45] and S. Parkin's domain-wall racetrack memory [46,47] have demonstrated the potential of controlling spin degrees of freedom for both logic and memory applications (**Figure 1.3**). More recently, research has expanded toward topological spintronics and antiferromagnetic spintronics, leveraging complex spin structures and interfacial textures for ultrafast, low-power information processing, while spintronic elements are being integrated into neuromorphic and quantum architectures. In parallel, spin caloritronics explore the coupling between spin and heat. Together, these developments illustrate how spintronics has evolved from a fundamental study of magnetoresistance into a central platform for next-generation information technologies.

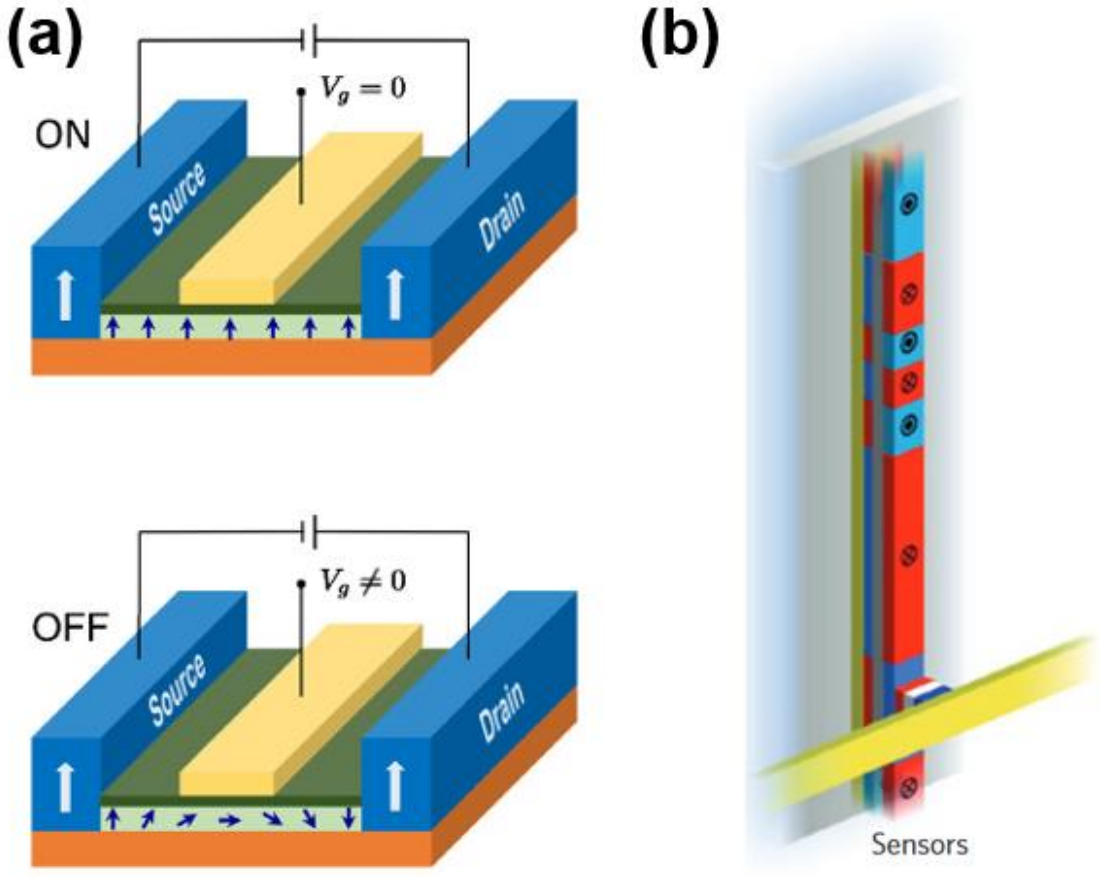


Figure 1.3 Datta–Das Spin FET and Domain-Wall Racetrack Memory (a) Datta-Das spin field-effect transistor use the top gate to control the Rashba SOC in the transport channel. Graph reproduced from Ref. [48]. (b) Racetrack memory stores digital data in the magnetic domain walls of nanowires. Graph reproduced from Ref. [47].

1.2 Spin Transport and Interfacial Phenomena

The modern frontier of spintronics lies at the interfaces, where heterostructure engineering plays a crucial role. Within magnetic heterostructures, numerous studies have uncovered a rich variety of interfacial spin phenomena and emergent functionalities. Key among these are proximity-induced magnetism and the anomalous Hall effect, spin Hall effect and spin Hall magnetoresistance, Dzyaloshinskii-Moriya interaction, the Rashba effect, and exchange bias. These interfacial phenomena offer promising pathways toward advanced data storage and computing technologies with ultralow power consumption.

1.2.1 Anomalous Hall Effect

The Hall effect, first observed by Edwin H. Hall in 1879 [2], describes the generation of a transverse voltage across a current-carrying conductor when subjected to a perpendicular magnetic field. This phenomenon, now known as the ordinary Hall effect (OHE), arises from the Lorentz force acting on moving charge carriers, deflecting them to one side of the conductor. Shortly after this discovery, Hall reported an additional, unexpected transverse voltage in ferromagnetic metals even in the absence of an external magnetic field, a phenomenon that later became known as the anomalous Hall effect (AHE) [3]. This observation revealed that the internal magnetization of a ferromagnet can itself act as an effective magnetic field for the charge carriers, giving rise to a Hall voltage proportional to the sample's magnetization (See **Figure 1.4** for an example).

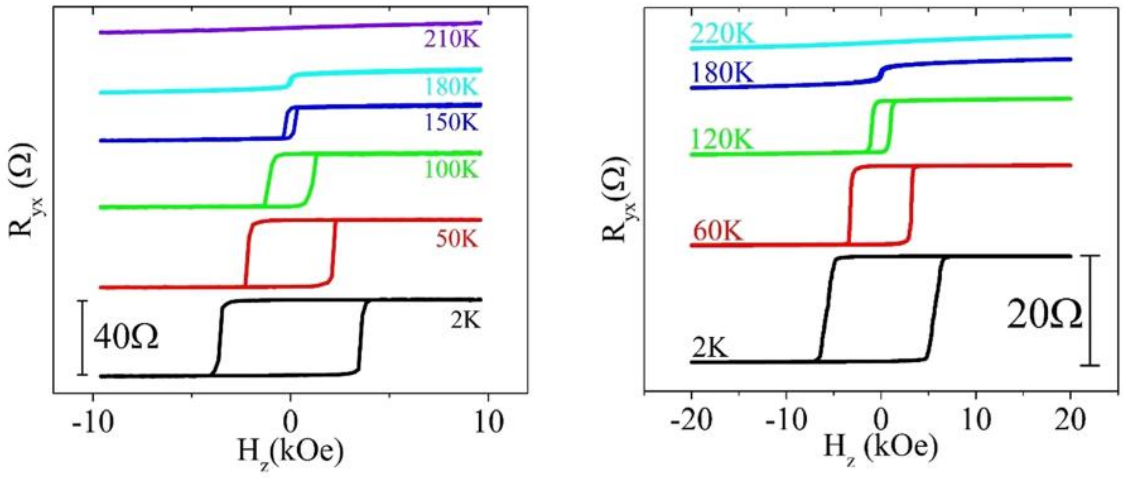


Figure 1.4 AHE for Two-Dimensional Van Der Waals Ferromagnets Fe_3GeTe_2 (left) and $Fe_5Ge_2Te_2$ (right) exhibit magnetic hysteresis loops in their transverse (Hall) resistance below their respective Curie temperatures when an out-of-plane magnetic field is applied. The results demonstrate robust perpendicular magnetic anisotropy down to the three-layer limit. Reproduced from Ref. [49].

Phenomenologically, the Hall resistivity (ρ_{xy}) in a ferromagnetic metal can be expressed as the sum of ordinary and anomalous contributions [50]:

$$\rho_{xy} = R_0 H + R_s M_z,$$

where R_0 is the ordinary Hall coefficient, H is the external magnetic field, R_s is the anomalous Hall coefficient, and M_z is the magnetization perpendicular to the measurement plane. The first term originates from the Lorentz force, while the second originates from the spin-dependent scattering or band structure effects associated with the magnetization and spin–orbit coupling. Experiments revealed that R_s has a subtle dependence on the longitudinal resistivity ρ_{xx} in the form of a power law $R_s \propto \rho_{xx}^n$. In the absence of external magnetic field, this is equivalent to $\rho_{xy} \propto \rho_{xx}^n$. We can convert this to the relation between

the anomalous Hall conductivity σ_{xy} and longitudinal conductivity σ_{xx}, yielding the expression $\sigma_{xy} \propto \sigma_{xx}^{2-n}$ under resistivity tensor inversion.

The microscopic origin of the AHE has been extensively studied and can be broadly classified into extrinsic and intrinsic mechanisms (see **Figure 1.5**). The extrinsic mechanisms arise from spin–orbit coupling during impurity scattering. Among them, skew scattering, proposed by Smit in 1955 [51] and 1958 [52], produces an anomalous Hall conductivity that scales linearly with the longitudinal conductivity ($\sigma_{xy} \propto \sigma_{xx}$). Side-jump scattering, introduced by Berger (1970) [53], results from a lateral displacement of the electron trajectory during scattering and is independent of the scattering time, yielding $\sigma_{xy} \propto \sigma_{xx}^{0}$. On the other hand, the intrinsic contribution, formulated by Karplus and Luttinger (1954) [54], originates from the Berry curvature of occupied electronic bands, which acts as an effective magnetic field in momentum space. This contribution is also independent of the scattering rate, yielding $\sigma_{xy} \propto \sigma_{xx}^{0}$, and typically dominates in materials with strong spin–orbit coupling and high crystallinity.

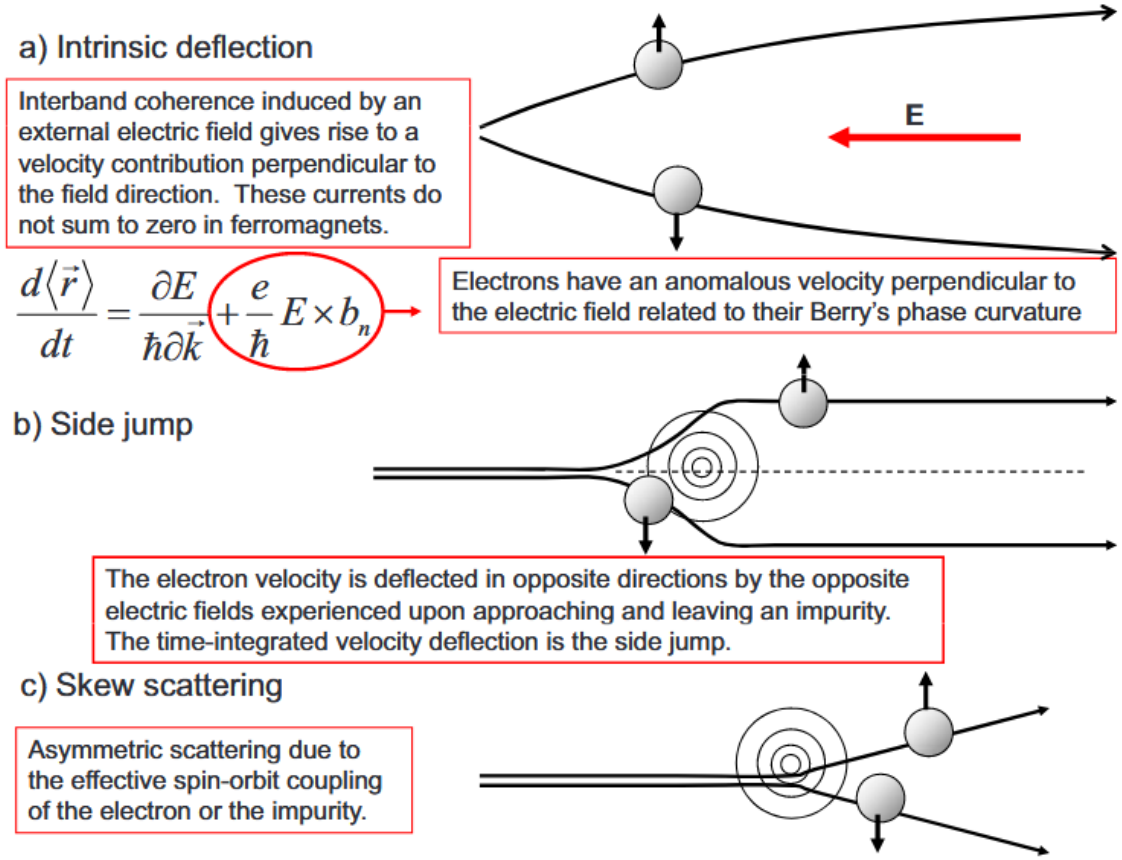


Figure 1.5 Three Main Mechanisms for AHE (a) Intrinsic deflection (b) Side jump (c) Skew scattering. Reproduced from Ref. [50].

Depending on the conductivity regime, different mechanisms dominate the AHE [49,50,55] (see **Figure 1.6**). In highly conductive metals ($\sigma_{xx} > 10^6$ S/cm), skew scattering tends to prevail. In the intermediate regime ($10^4 < \sigma_{xx} < 10^6$ S/cm), the intrinsic and side-jump mechanisms are often comparable. In contrast, in dirty "poor metal" regime where conductivity is dominant by hopping transport ($\sigma_{xx} < 10^4$ S/cm), a characteristic scaling of $\sigma_{xy} \propto \sigma_{xx}^{1.6}$ is reported [56,57]. These dependencies provide powerful experimental means to identify the dominant mechanism in different materials.

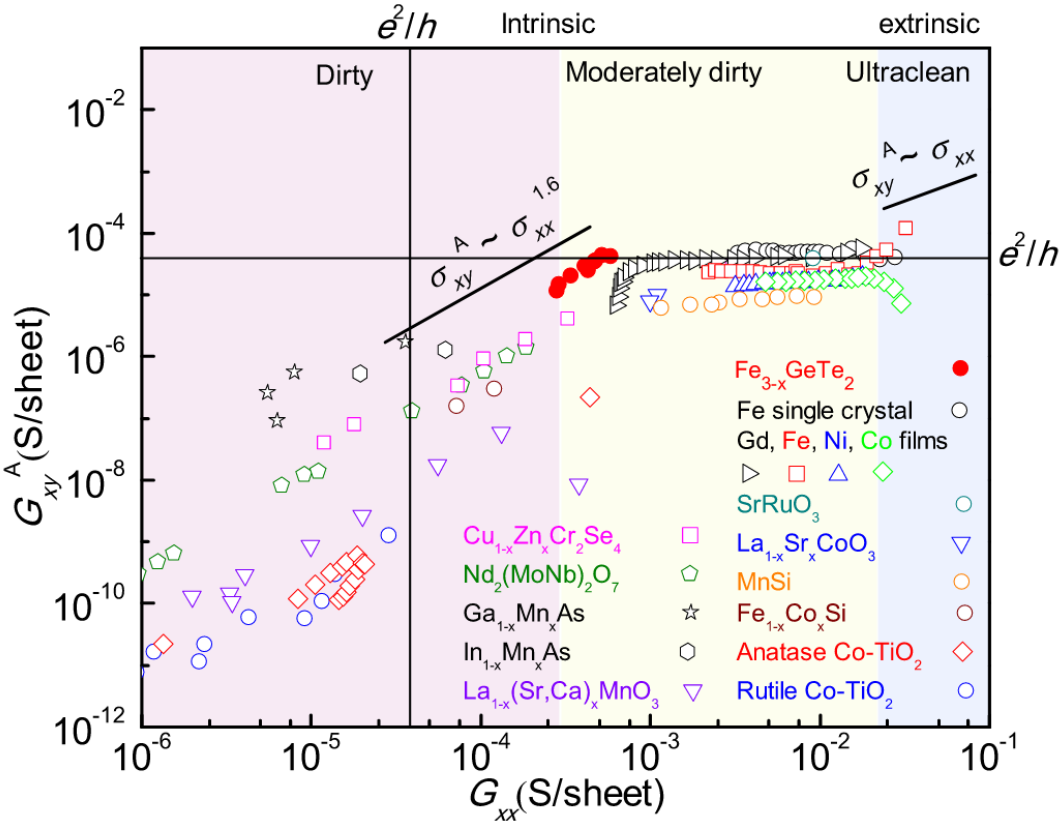


Figure 1.6 AHE Conductivity in Different Conductivity Regimes The longitudinal and transverse conductivities per atomic layer, G_{xx} and G_{xy}, for various ferromagnets are plotted. Reproduced from the Supplementary Information of Ref [55].

In recent years, the concept of AHE has evolved beyond the realm of conventional ferromagnets with magnetization perpendicular to the measurement plane, revealing its profound connection to the topology of electronic band structures. Studies of noncollinear AFMs such as Mn_3X [58–63] and collinear AFMs such as RuO_2 [64,65] (also referred to as altermagnets) have led to the discovery of large unconventional AHE signals in materials without net magnetizations, known as anomalous Hall antiferromagnets [66]. Moreover, in-plane anomalous Hall effect (IPAHE) has been predicted [67] and observed [68], where

the out-of-plane Berry curvature is induced by in-plane magnetization due to sufficiently low point-group symmetry. Such IPAHE is odd under time reversal, which is different from planar Hall effect.

On the other hand, the quantum anomalous Hall effect (QAHE) represents the quantized limit of the AHE, realized when magnetism is introduced to a topologically protected boundary states, producing a dissipationless Hall current in the absence of an external magnetic field [69]. QAHE was first experimentally realized in magnetically doped topological insulators $(Bi,Sb)_2Te_3$ [70] and later in $MnBi_2Te_4$ [71] and Moiré systems [72,73]. Meanwhile, the topological Hall effect (THE) arises from a real-space analogue of Berry curvature generated by chiral spin textures such as skyrmions [74,75], where the emergent effective field gives rise to an additional Hall contribution distinct from both the ordinary and anomalous terms.

These developments extend the AHE from a classical ferromagnetic phenomenon to a universal probe of band topology, spin–orbit coupling, and symmetry breaking in a broad range of quantum materials. As a result, the AHE now serves not only as a fundamental transport signature of magnetism, but also as a key tool in exploring and engineering topological and spintronic functionalities in emerging materials systems.

1.2.2 Magnetic Proximity Effect

Proximity effects refer to the emergence of new physical properties in a material when placed in contact with another, arising from interfacial coupling and wave function overlap without the need for chemical modification. One well-known example is the superconducting proximity effect, where Cooper pairs leak from a superconductor into an adjacent normal metal, inducing superconducting correlations over a short distance. Similarly, spin–orbit coupling (SOC) proximity effects can occur when a material with weak intrinsic SOC (such as graphene) is interfaced with a heavy-element substrate, resulting in enhanced Rashba SOC [48,76]. In another manifestation, charge-transfer proximity arises when two materials with different work functions form a heterostructure, leading to interfacial charge redistribution that modifies carrier density, band alignment, and even magnetic or topological properties.

The magnetic proximity effect (MPE) refers to the induction of magnetic order in a non-magnetic material when it is placed in contact with a magnetic layer. Through interfacial exchange interaction, the electronic states of the non-magnetic layer can become spin-polarized, thereby acquiring an effective magnetization. This interfacial magnetism provides a unique route to integrate magnetic functionalities into otherwise non-magnetic materials, enabling new types of spintronic devices.

A common strategy to realize MPE in heterostructures is to interface a heavy metal with strong spin-orbit coupling (e.g., Pt, Pd, W, or Ta) and a ferromagnetic insulator. The induced interfacial magnetization can lead to measurable changes in transport properties such as the AHE and AMR, even though the metallic layer itself is nominally non-

magnetic. For example, Huang et al. reported an anomalous Hall effect in Pt/YIG bilayers and attributed it to proximity-induced ferromagnetism [77]. Later, Lu et al. confirmed the observed magnetization induced in Pt adjacent to YIG using x-ray magnetic circular dichroism (XMCD) [78]. The approach has since been applied to other similar systems such as TmIG/Pt and TmIG/W bilayers to identify AHE contributions from different microscopic mechanisms [79] (see **Figure 1.7**).

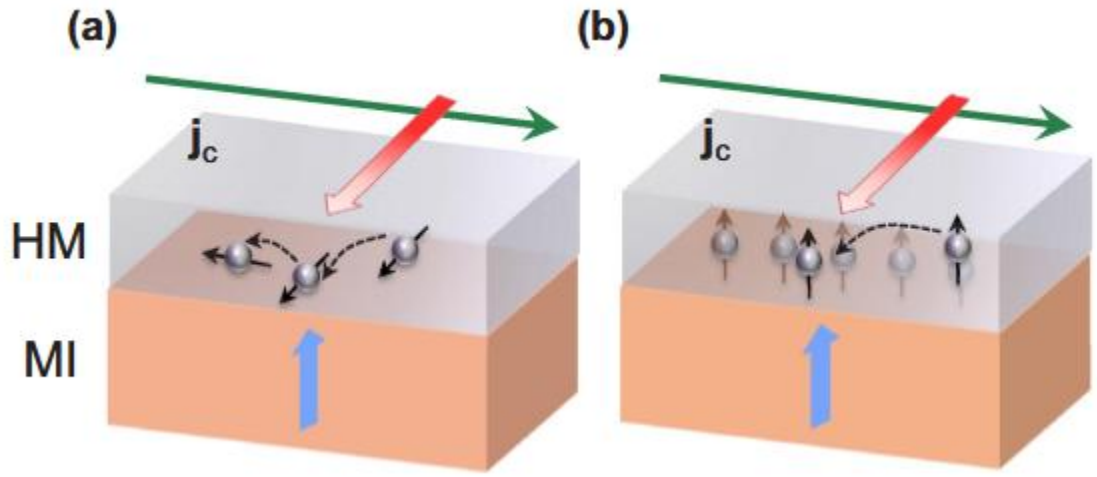


Figure 1.7 Different Mechanisms for AHE in HM/MI Bilayers (a) Spin Hall anomalous Hall effect. (b) Magnetic proximity effect-induced anomalous Hall effect. Reproduced from [79].

The discovery of 2D van der Waals magnetic materials [80–84] launched a new frontier in condensed matter physics and provided new platforms to explore proximity-induced magnetism in atomically sharp and contamination-free interfaces. Subsequent studies have revealed induced magnetic signatures in heavy metals interfaced with these 2D magnets. For instance, Lohmann *et al.* reported an anomalous Hall effect (AHE) in Pt/$Cr_2Ge_2Te_6$ (CGT) heterostructures, serving as a sensitive probe of the CGT magnetic

order [85]. Later, Su *et al.* observed a spin-flop transition in CrI_3 that could be electrically detected through magnetoresistance in an adjacent Pt layer and further manipulated via current injection, demonstrating efficient spin-current transfer and its interplay with 2D magnetic order [86].

More recent works have extended MPE studies to the heterostructures of magnetic materials and quantum materials, where proximity-induced exchange gaps or spin splitting can open new avenues for topological or quantum spintronic devices. One of the representative quantum materials that attracts huge attention is graphene, which exhibits quantum Hall effect because of its exceptional topology of the band structure [87]. Despite weak intrinsic SOC [88,89], topological nontrivial states such as quantum spin Hall effect (QSHE) [90] and quantum anomalous Hall effect (QAHE) [91] can be realized in graphene when a sizable SOC and spin polarization is introduced by MPE [76,92,93].

The first successful introduction of spin polarization in graphene by magnetic proximity effect was reported by Z. Wang et al. in 2015, in which single layer graphene coupled to an atomically flat YIG thin film shows ferromagnetism evidenced by an anomalous Hall effect [94], which can be observed up to room temperature (see **Figure 1.8**). Later studies revealed spin-polarized transport in graphene on various magnetic insulators (BiFeO3, EuO, EuS) [95–97] and van der Waals magnets ($Cr_2Ge_2Te_6$, $CrBr_3$) [98,99].

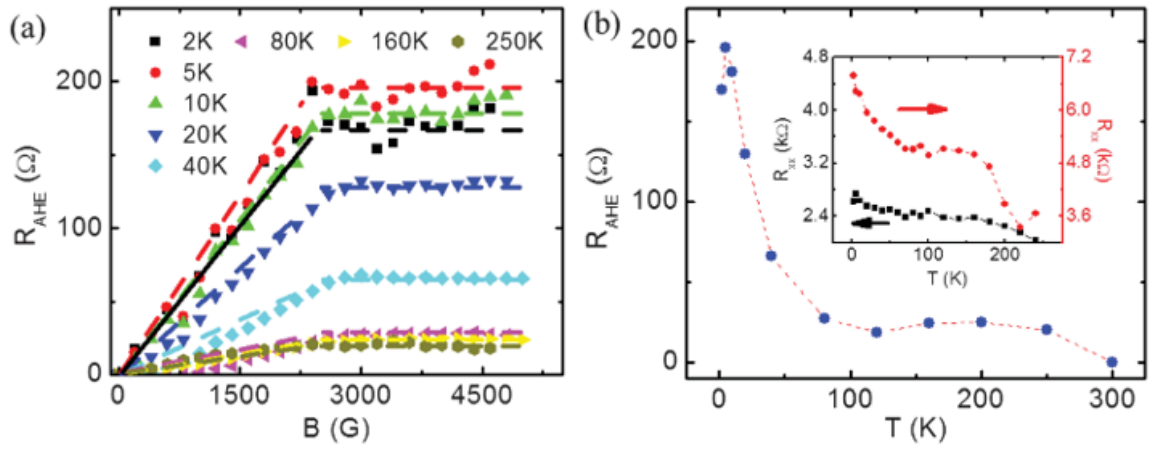


Figure 1.8 AHE in Graphene/YIG Heterostructure (a) $R_{AHE} - B$ at different temperatures. (b) $R_{AHE} - T$. Reproduced from Ref. [94].

Beyond graphene, topological insulators (TIs) that exhibit long spin coherence and consequently fault-tolerant information storage are also extensively studied for topological spintronics [100]. TIs such as $(Bi,Sb)_2(Se,Te)_3$ interfaced with ferromagnetic insulators (YIG, EuS, TmIG) exhibit MPE-induced gap opening in surface states and AHE [101–103], offering a potential route to realize the QAHE without magnetic doping. In recent years, 2D TIs, also known as quantum spin Hall insulators (QSHIs), have emerged as a new class of materials hosting topologically protected helical edge states within an insulating bulk. A well-established example is monolayer WTe_2, which behaves as a type-II Weyl semimetal in its bulk form [104,105] but becomes a 2D TI in its single-layer limit [106–108], therefore attracting strong research interest in exploring novel physics when the helical edge states is brought into close proximity with magnetic materials, such as CrI_3 [109] or $Cr_2Ge_2Te_6$ [110].

Together, these developments highlight the central role of MPE in modern spintronics. Understanding how proximity-induced magnetism manifests in heterostructures is crucial for advancing next-generation spintronic and topological devices that harness magnetic functionalities without the drawbacks of magnetic doping.

1.2.3 Spin Hall Effect and Spin Hall Magnetoresistance

When a charge current J_c flows through a heavy metal such as Pt, Ta, or W, the spin–orbit interaction deflects electrons with opposite spins to opposite transverse edges, generating a pure spin current flowing perpendicular to the charge current. This phenomenon, known as the spin Hall effect (SHE), was first observed experimentally in semiconductors [26,27] and later in metals [28,29]. Conversely, when a spin current enters a heavy metal, the inverse spin Hall effect (ISHE) [40] converts it back into a measurable transverse charge voltage. The discovery of the SHE and ISHE marked a major milestone in spintronics, revealing that spin and charge currents can be interconverted in materials with strong spin–orbit coupling (SOC).

Building on these concepts, Spin Hall Magnetoresistance (SMR) was discovered by Nakayama et al. [35] in Pt/YIG (Yttrium Iron Garnet, $Y_3Fe_5O_{12}$, a ferrimagnetic insulator) bilayers. Unlike conventional magnetoresistance effects that originate from spin-dependent scattering within a ferromagnet, SMR arises from the modulation of spin current reflection and absorption at the interface between a non-magnetic metal (NM) with strong SOC and an adjacent magnetic insulator (MI). (see **Figure 1.9**) When a charge current $\boldsymbol{J_c}$

flows in the NM layer, the SHE generates a spin current $\boldsymbol{J_s}$ with polarization $\boldsymbol{\sigma} \perp \boldsymbol{J_c}$. Upon reaching the NM/MI interface, part of this spin current is absorbed if $\boldsymbol{\sigma}$ is non-collinear with the local magnetization $\boldsymbol{M}$, while it is reflected if $\boldsymbol{\sigma} \parallel \boldsymbol{M}$. The reflected spin current is then converted back into a charge current through the ISHE, modifying the longitudinal resistance of the NM layer. This interplay between SHE, ISHE, and spin transfer at the interface gives rise to a magnetization-dependent resistance change known as the SMR.

In the case of ferromagnetic insulator (FMI)/heavy metal (HM) bilayers such as YIG/Pt, the longitudinal and transverse resistivities can be described phenomenologically as [35,111]:

$$\rho_{xx} = \rho_0 + \Delta\rho_1(1 - m_y^2)$$

$$\rho_{xy} = \Delta\rho_1\, m_x m_y + \Delta\rho_2 m_z$$

where ρ_0 is the baseline resistivity, $\Delta\rho_1$ quantifies the SMR amplitude, m_i are the vector components of the magnetization unit vector $\boldsymbol{m} = \frac{\boldsymbol{M}}{\boldsymbol{M_s}}$, and $\Delta\rho_2$ represents a contribution to the transverse voltage known as the spin Hall anomalous Hall effect [111]. This expression predicts characteristic angular dependences of R_{xx} and R_{xy} when the magnetization unit vector $\boldsymbol{m}$ is rotated with respect to the charge current $\boldsymbol{J_c}$. Specifically, R_{xx} shows a $\cos^2\phi$ dependence, while R_{xy} exhibits a $\sin\phi\cos\phi$ behavior, where ϕ is the angle between $\boldsymbol{m}$ and $\boldsymbol{J_c}$. These angular dependencies are widely used as experimental signatures to distinguish SMR from other magnetoresistive effects [112–114].

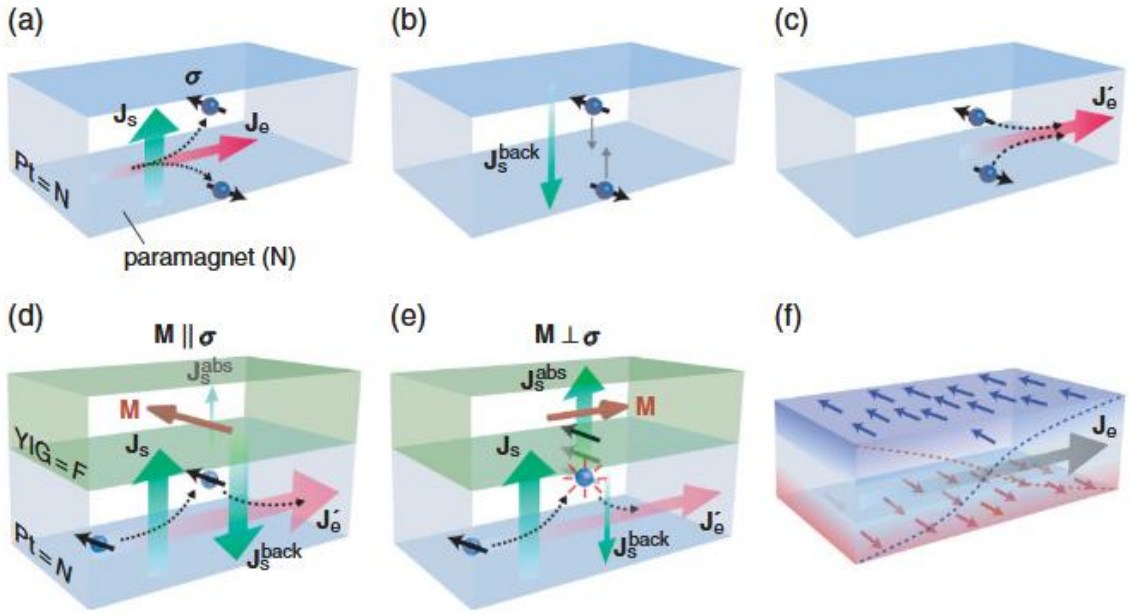


Figure 1.9 Spin Hall Magnetoresistance (a) Spin Hall effect. (b)(c) Inverse spin Hall effect. (d) When $\boldsymbol{\sigma} \parallel \boldsymbol{M}$, J_s is mostly reflected at NM/MI interface and converted back to charge current. (e) When $\boldsymbol{\sigma} \perp \boldsymbol{M}$, J_s is mostly absorbed at NM/MI interface. (f) Spin accumulation by SHE. Reproduced from Ref. [35].

The concept of SMR has been extended to antiferromagnetic (AFM) systems, where the relevant order parameter is the Néel vector $\boldsymbol{L}$ (or unit vector $\boldsymbol{l}$) rather than the magnetization $\boldsymbol{M}$. In AFM/HM bilayers, the same spin current reflection mechanism applies, but the resistance depends on the orientation of $\boldsymbol{l}$ with respect to $\boldsymbol{J_c}$. The corresponding resistivities can be expressed as [115]:

$$\rho_{xx} = \rho_0 - \Delta\rho(1 - l_y^2)$$

$$\rho_{xy} = \Delta\rho\, l_x l_y$$

which share the same mathematical form as in FM systems, with $\boldsymbol{m}$ replaced by $\boldsymbol{l}$. This AFM SMR has emerged as a powerful tool for probing the Néel vector orientation and

magnetic phase transitions in insulating AFMs [115–117], establishing SMR as a cornerstone technique in AFM spintronics.

1.2.4 Exchange Bias

Exchange bias is a phenomenon that arises at the interface between a FM and an AFM, where interfacial exchange coupling leads to a shift of the FM hysteresis loop along the magnetic field axis [118,119]. This shift, quantified as the exchange bias field H_E, reflects the unidirectional anisotropy imposed on the FM by the AFM (see **Figure 1.10**). The effect is typically established by cooling the FM/AFM bilayer through the Néel temperature of the AFM in the presence of an external magnetic field, which aligns the AFM spins at the interface. The magnitude and direction of exchange bias depend on factors including interfacial quality, AFM thickness, crystallographic orientation, and temperature, making it a sensitive probe of interfacial magnetic interactions.

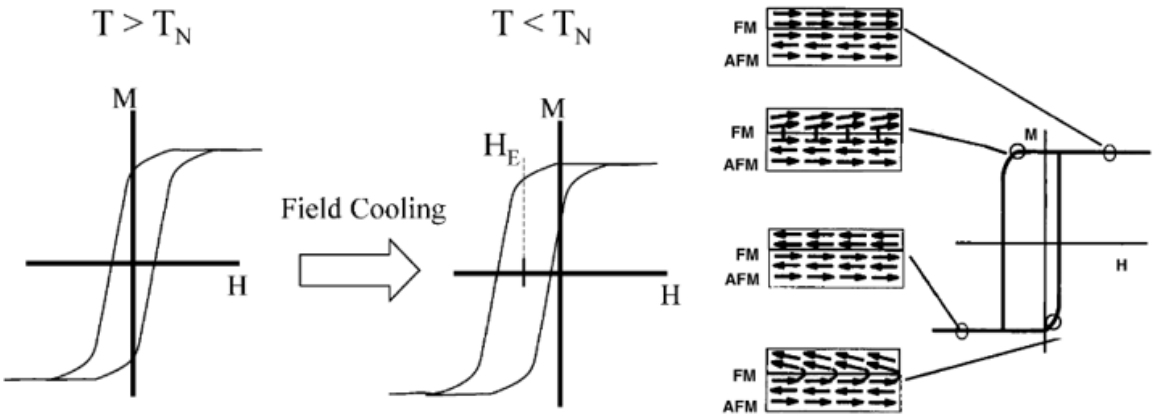


Figure 1.10 Exchange Bias in FM/AFM Exchange bias is established by field cooling the FM/AFM bilayer through the AFM Néel temperature. Reproduced from Ref. [118].

1.3 Antiferromagnetic Spintronic

Antiferromagnetism was identified and systematically explained by Louis Néel in the 1930s. In his Nobel lecture, Néel emphasized the conceptual importance of staggered (Néel) order while noting that, for a long time, antiferromagnets (AFMs) appeared to be of no practical use [120]. Néel's famous assessment that AFMs were “interesting but useless” set the tone for decades of research.

The primary reason for this historical pessimism and the central technical challenge is the difficulty in controlling and detecting the AFM order parameter, the Néel vector. Unlike FMs, which possess a net magnetization and couple strongly to an external magnetic field, AFMs have zero net magnetization. This inherent property makes AFM immune to conventional magnetic field control and invisible to standard magnetometers and readout techniques. How to electrically write, read, and propagate spin information therefore became the key to realizing AFM spintronics.

Despite the challenges, AFMs found an early and still critical practical role as passive elements in spintronics. The discovery of exchange bias by Meiklejohn & Bean in 1956 [121] showed that coupling an AFM to a FM pins the FM’s magnetization and gives rise to a shifted hysteresis loop, a phenomenon that became central to read-heads, sensors and later MRAM stacks including spin-valves and magnetic tunnel junctions [8].

More recently the field has inverted the question: instead of using AFMs only as passive pinning layers, researchers have asked whether AFMs can be active functional materials for information storage and manipulation. AFM spintronics offers several intrinsic advantages over conventional ferromagnetic systems as emphasized in several

influential reviews [43,122–125]. The absence of net magnetization and stray fields makes AFMs robust and minimizes interference, enabling high-density device integration. Their characteristic ultrafast spin dynamics, often in the terahertz regime, opens the possibility for high-speed logic operation and communications. Moreover, AFMs naturally provide non-volatility, maintaining their spin configuration without power consumption. Together, these features directly address key demands of modern electronics, positioning AFM-based devices as highly promising candidates for next-generation spintronic technologies.

1.3.1 Current-Driven Electrical Switching

In 2014, Železný et al. predicted that in crystals with the right symmetry a lateral electrical current can generate staggered, sublattice-opposite torques, known as Néel SOT, capable of reorienting the Néel vector, opening a clear route to electrical writing in AFMs [126]. Building on this idea, Wadley et al. demonstrated current-induced switching of the transverse signals of multi-terminal CuMnAs devices [127] (see **Figure 1.11**), which they interpreted as signatures of Néel vector reorientation driven by the Néel SOT. Later, similar current-driven electrical switching are achieved in other AFM systems such as Mn_2Au [128,129] and extended to HM/AFM bilayers such as Pt/NiO [130,131] and Pt/α-Fe_2O_3 [132].

Later investigations by Chiang et al. examined the HM/AFM multi-terminal device response and showed that comparable switching-like transverse signals can also arise from anisotropic thermal effects even without AFM layer, highlighting that such electrical measurements may admit both magnetic and thermal interpretations [133]. This result

underscored the need for complementary magnetic characterization to unambiguously distinguish Néel-vector switching from thermal artifacts.

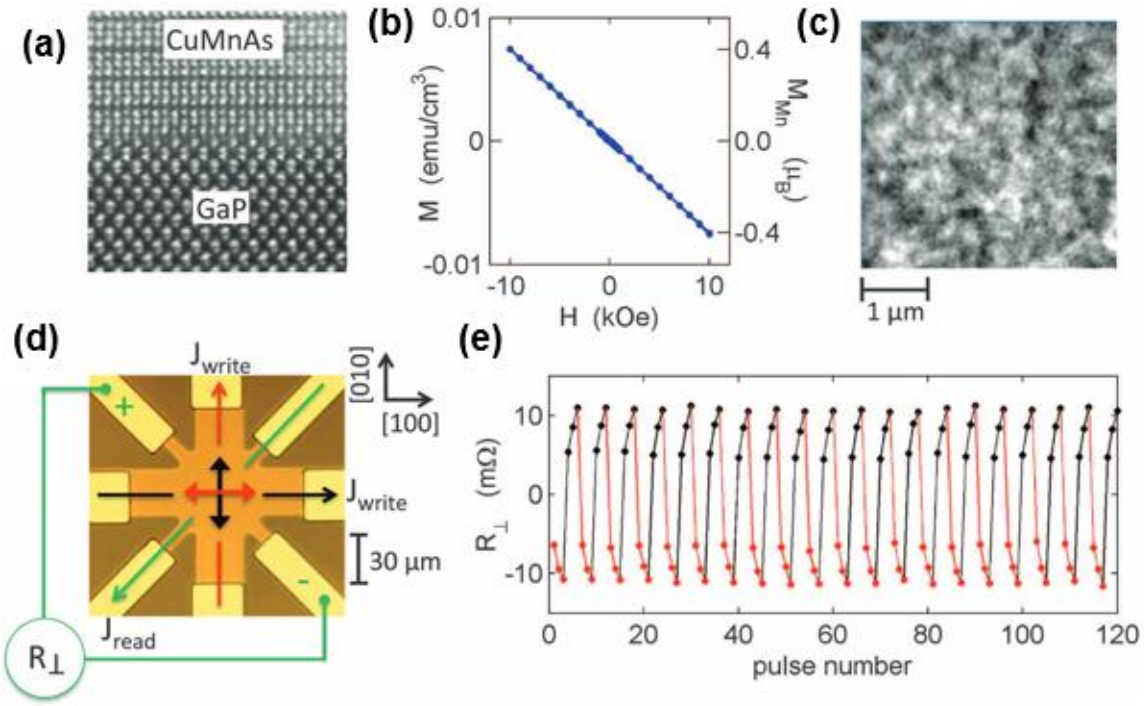


Figure 1.11 Electrical Switching of the Antiferromagnet CuMnAs (a) STEM image of CuMnAs/GaP. (b) M vs. H of the CuMnAs/GaP bilayer. (c) XMLD-PEEM image of the CuMnAs film. (d) Optical microscopy image of the device and schematic of the measurement geometry. (e) Electrical switching of the transverse resistance by applying writing pulses. Reproduced from Ref. [127].

1.3.2 Long-Range Nonlocal Spin Transport

Experiments showed that AFM insulators can carry spin information via magnons over tens of micrometers, a surprisingly long distance, and that transport can be turned on/off electrically, paving the way for AFM-based magnonic interconnects and logic. A representative demonstration from Lebrun et al. shows electrically controllable long-

distance spin transport through a crystalline AFM α-Fe_2O_3 [134]. Another study from Yuan et al. demonstrated long-distance spin transport and signatures of spin superfluid ground state in AFM Cr_2O_3 [135].

1.3.3 Sub-THz Spin Pumping

AFMs operate in the native terahertz (THz) frequency range, which is orders of magnitude higher than conventional FMs. This high-frequency operation positions AFMs as a premier platform for ultrafast spintronic devices. The key to accessing these dynamics is spin pumping: the process where a precessing magnetization dynamically injects a pure spin current into an adjacent heavy metal like Pt. The injected spin current is then converted into a measurable electrical voltage via the Inverse Spin Hall Effect (ISHE). Extending this crucial spin-charge conversion mechanism to the sub-THz regime of AFMs is central to the field.

The theoretical possibility of this mechanism was established by Cheng et al. in 2014 [136]. Contrary to the initial intuition that the antiparallel spin dynamics would cancel, the theory showed that the coherent precession of the two sublattices at the antiferromagnetic resonance (AFMR) frequency can, in fact, constructively add up, resulting in a net, pumped spin current.

This fundamental prediction was definitively confirmed by two landmark experimental studies in 2020. Li et al. demonstrated sub-THz spin pumping in a Cr_2O_3/Pt heterostructure by coherently exciting the AFMR at 0.240 THz [42]. They verified the

nature of pure spin current by observing a polarity reversal in the ISHE voltage when switching the spin detector from Pt to β-Ta. Simultaneously, Vaidya et al. utilized circularly polarized sub-THz radiation on MnF_2/Pt interfaces to selectively excite magnon modes with a specific chirality [137]. Observing that the ISHE voltage polarity depended directly on the magnon's handedness provided the clean, definitive proof of coherent dynamical spin pumping from an AFM.

Together, these pioneering works validate the use of THz AFM dynamics for practical spin current generation. They shift AFMs into the role of active, ultra-high-frequency components, paving the way for ultrafast, compact, and energy-efficient spintronic devices.

1.3.4 Magnetoelectric Control of the Néel Vector

The magnetoelectric (ME) effect links electronic and magnetic properties, offering unique opportunities to control magnetism through applied electric fields, or vice versa. This dual control mechanism has attracted significant attention from both applied and fundamental perspectives. Many known magnetoelectric materials are antiferromagnets (AFMs) [138–140]. As the first theoretically predicted and experimentally confirmed magnetoelectric material, Cr_2O_3 has been extensively studied for more than six decades, yielding a wealth of insights into its fundamental properties.

Early investigations in the last century laid the groundwork for understanding the magnetoelectric characteristics of Cr_2O_3 [141–145]. In 2005, Borisov *et al.* demonstrated the electric-field control of perpendicular exchange bias in FM/Cr_2O_3 heterostructures

through magnetoelectric coupling [146], highlighting the ability to manipulate and detect the Néel vector in Cr_2O_3. Building on this progress, He *et al.* achieved isothermal magnetoelectric switching in Cr_2O_3 single crystals in 2010 [147], followed by Ashida *et al.* who extended this result to thin films in 2015 [148]. These studies primarily relied on exchange bias in FM/AFM systems, where the presence of a ferromagnetic layer provided indirect readout but limited the realization of truly AFM-based spintronic devices.

A major breakthrough came in 2017, when Kosub *et al.* demonstrated a purely AFM magnetoelectric memory based on Cr_2O_3, achieving both magnetoelectric switching and electrical detection of the surface uncompensated moment using a Pt Hall layer [149]. This work established magnetoelectric antiferromagnets as strong candidates for next-generation memory technologies. Recently, we reported the electrical detection of Néel vector orientation across the spin-flop transition in Cr_2O_3 [150] (see **Fig. 1.12**). Both field cooling and magnetoelectric control were employed to manipulate the Néel vector. Our advances in Cr_2O_3 will be discussed in detail in the following chapters.

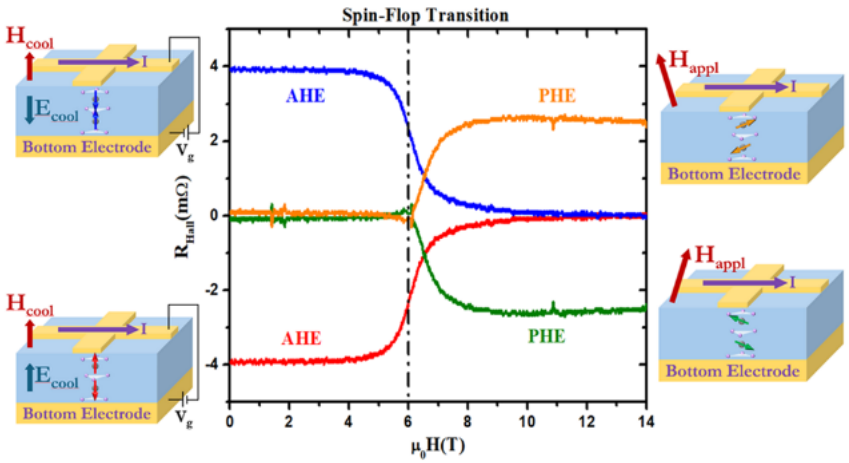


Figure 1.12 Electrical Detection of Néel Vector in Cr_2O_3 Reproduced from Ref. [150].

1.4 Properties and Dynamics of Uniaxial Antiferromagnets

Magnetic materials can exhibit a wide range of ordered states depending on the nature of the exchange interaction between atomic moments (see **Figure 1.13**). In the paramagnetic (PM) state, thermal fluctuations dominate, and the magnetic moments are randomly oriented, resulting in zero net magnetization. In contrast, ferromagnetic (FM) materials exhibit parallel alignment of magnetic moments below the Curie temperature, leading to spontaneous macroscopic magnetization. Ferrimagnets (FiM) consist of two or more magnetic sublattices aligned antiparallelly but with unequal moments, producing a finite net magnetization.

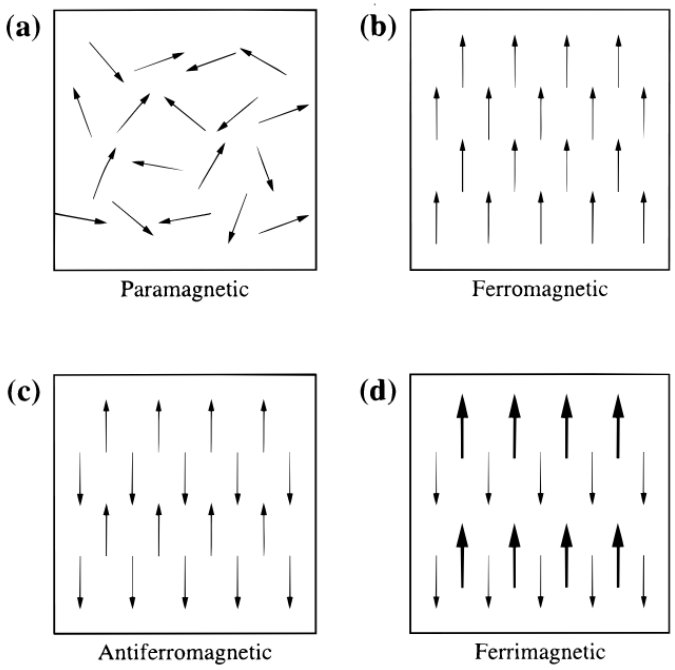


Figure 1.13 Different Types of Magnetic Order (a) Paramagnetic. (b) Ferromagnetic. (c) Antiferromagnetic. (d) Ferrimagnetic. Reproduced from Ref. [138].

In antiferromagnets (AFM), neighboring spins align antiparallel with equal magnitude, resulting in zero net magnetization while maintaining long-range magnetic order below the Néel temperature. This antiparallel arrangement is stabilized by the exchange interaction, which favors opposite spin alignment. Among various AFM configurations, the uniaxial antiferromagnet represents the simplest and most fundamental case. In such systems, the magnetic anisotropy constrains the spins of the two sublattices to align collinearly along a single crystallographic easy axis.

1.4.1 Néel Vector

In a uniaxial AFM, the magnetic moments of neighboring atoms align antiparallel due to strong exchange interactions, resulting in vanishing net magnetization in equilibrium. Instead of the total magnetization, the order parameter describing the magnetic state of an AFM is the Néel vector, defined as

$$\boldsymbol{L} = \boldsymbol{M_1} - \boldsymbol{M_2}$$

where $\boldsymbol{M_1}$ and $\boldsymbol{M_2}$ are the sublattice magnetizations of the two oppositely aligned spin sublattices. The Néel vector thus characterizes the orientation and magnitude of the AFM magnetic order, playing a role analogous to the magnetization $\boldsymbol{M}$ in ferromagnets.

Because the net magnetization $\boldsymbol{L} = \boldsymbol{M_1} + \boldsymbol{M_2}$ is typically negligible in AFM, the Néel vector serves as the fundamental quantity governing AFM properties and dynamics. Its direction is key to spin-dependent transport and magnetoelectric effects, while its orientation under external fields or stimuli lies at the heart of AFM spintronics.

1.4.2 Spin-Flop Transition

The Néel vector $\boldsymbol{L}$ in AFM responds differently from the magnetization $\boldsymbol{M}$ in ferromagnets to an external magnetic field. In a collinear AFM, neighboring spins align antiparallel to each other due to strong exchange interaction J. When an external magnetic field $\boldsymbol{H}$ is applied along the easy axis, the system initially resists reorientation because of the uniaxial magnetic anisotropy K_u. However, once the field exceeds a critical threshold H_{SF}, known as the spin-flop transition field, the AFM sublattice moments abruptly undergo a first-order transition to form a canted spin configuration, with a small canted moment parallel to the applied field, and the Néel vector perpendicular to it. This transition is known as spin-flop transition (SFT), which minimizes the total energy by reducing the Zeeman energy while also maintaining substantial antiparallel alignment between the sublattices to reduce the exchange energy [151,152].

Physically, the spin-flop transition represents a balance among three key energies: (i) Exchange energy favoring antiparallel spin alignment, (ii) Anisotropy energy favoring spin alignment along the easy axis, and (iii) Zeeman energy favoring spin alignment along the external field. If we consider a simple two-sublattice uniaxial AFM model with sublattice magnetizations $\boldsymbol{M_1}$ and $\boldsymbol{M_2}$, each of magnitude M_s, with magnetic field $\mu_0 H$ applied along the easy axis ($\hat{z}$), the free energy density F can be expressed by the simple model:

$$F = J\boldsymbol{m_1} \cdot \boldsymbol{m_2} - K_u(m_{1z}^2 + m_{2z}^2) - \mu_0 H M_s(m_{1z} + m_{2z})$$

where J is the exchange interaction favoring antiparallel alignment ($J > 0$), K_u is the uniaxial magnetic anisotropy favoring spins along easy axis ($K_u > 0$), $\boldsymbol{m_1}$ and $\boldsymbol{m_2}$ are the unit vector of $\boldsymbol{M_1}$ and $\boldsymbol{M_2}$.

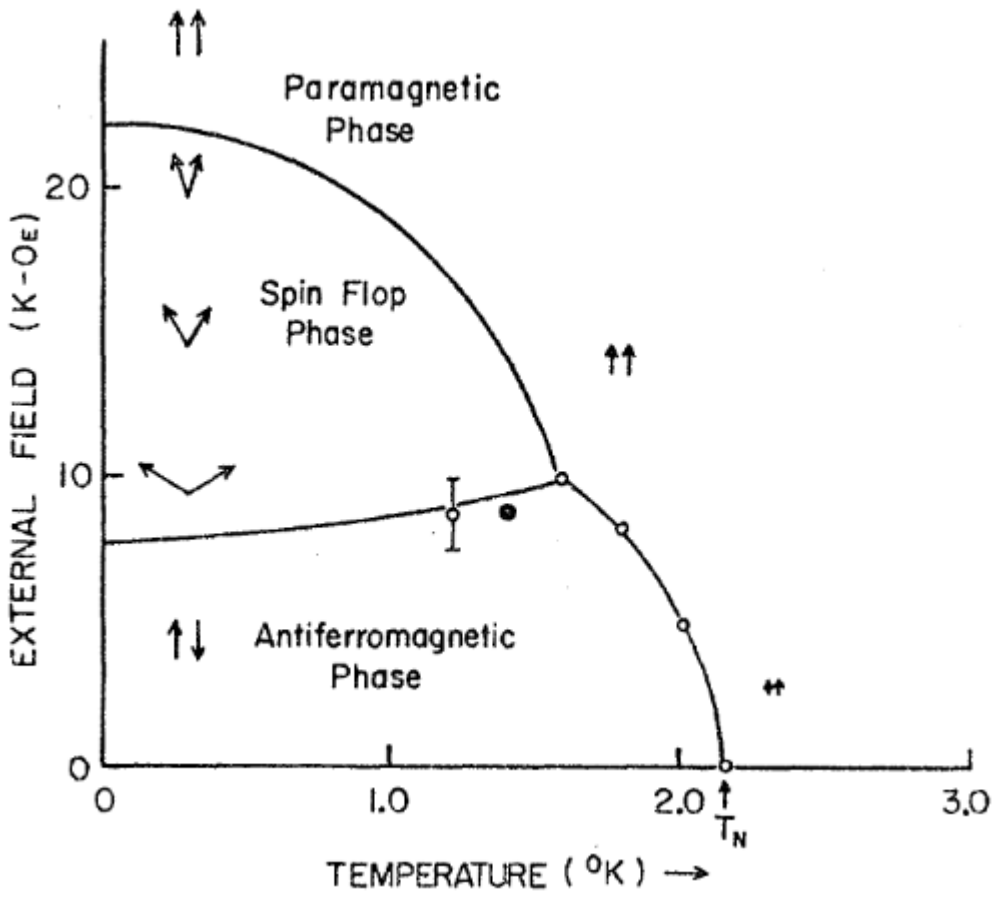


Figure 1.14 Phase Diagram of Spin-Flop Transition Reproduced from Ref. [151].

Minimizing the total energy with respect to the spin canting angle gives the critical field for the spin-flop transition:

$$H_{SF} = \sqrt{H_A(2H_E - H_A)}$$

where $H_E = \frac{2JM_S}{\mu_0}$ is the exchange field, and $H_A = \frac{2K_u}{\mu_0 M_s}$ is the anisotropy field. In the common case where $H_A \ll H_E$, this simplifies to

$$H_{\mathrm{SF}} \approx \sqrt{2H_E H_A}$$

It is worth noting that the magnetic anisotropy K_u in the above expression generally includes multiple contributions, such as magnetocrystalline, shape, and strain-induced anisotropies. In antiferromagnetic crystals like Cr_2O_3, the magnetocrystalline term typically dominates. However, in epitaxial thin films or multilayer structures, K_u should be regarded as an effective anisotropy that incorporates additional factors, such as strain-induced anisotropy or interfacial exchange arising at FM/AFM interfaces.

1.4.3 Dynamics and Resonance

Landau–Lifshitz–Gilbert (LLG) equation describes the dynamics of magnetization **M** (unit vector $\boldsymbol{m} = \frac{\boldsymbol{M}}{M_S}$) in a solid:

$$\frac{d\boldsymbol{m}}{dt} = \underbrace{-\gamma \boldsymbol{m} \times \boldsymbol{H_{eff}}}_{precessional\ torque} + \underbrace{\alpha \boldsymbol{m} \times \frac{d\boldsymbol{m}}{dt}}_{Gilbert\ damping}$$

where γ is the gyromagnetic ratio, α is the Gilbert damping constant, and $\boldsymbol{H_{eff}}$ is the effective magnetic field. This equation includes two terms. The first term describes the angular precession motion of the moment in $\boldsymbol{H_{eff}}$. The second term describes an energy dissipative process that aligns the moment with $\boldsymbol{H_{eff}}$, known as Gilbert damping. The $\boldsymbol{H_{eff}}$ comes from the partial differentiation of the free energy $-\frac{\partial F}{\partial m}$, which includes exchange,

anisotropy, Zeeman, and other interaction terms. LLG equation is introduced by Landau & Lifshitz in 1935 [153], and later reformulated by Gilbert in 1955 [154].

For uniaxial AFMs with two magnetic sublattices, $\boldsymbol{m_1} = \frac{\boldsymbol{M_1}}{M_s}$, and $\boldsymbol{m_2} = \frac{\boldsymbol{M_2}}{M_s}$, the dynamics can be described by considering each sublattice individually:

$$\frac{d\boldsymbol{m_1}}{dt} = -\gamma \boldsymbol{m_1} \times \boldsymbol{H_{eff,1}} + \alpha \boldsymbol{m_1} \times \frac{d\boldsymbol{m_1}}{dt}$$

$$\frac{d\boldsymbol{m_2}}{dt} = -\gamma \boldsymbol{m_2} \times \boldsymbol{H_{eff,2}} + \alpha \boldsymbol{m_2} \times \frac{d\boldsymbol{m_2}}{dt}$$

It's sometimes useful to formulate the equations in terms of the Néel vector $l = \frac{m_1 - m_2}{2}$ and net magnetization $m = \frac{m_1 + m_2}{2}$ [123,155]. The antiferromagnetic resonance (AFMR) frequency can be derived by considering the precessional motion, which is demonstrated by Kittel [156,157]. The resonance frequencies of the uniform precessional modes (with wave vector k = 0) are

$$\frac{\omega}{\gamma \mu_0} = \sqrt{2H_A H_E} \pm H \ (for\ H < H_{SF})$$

$$\frac{\omega}{\gamma \mu_0} = \sqrt{H^2 - 2H_A H_E} \ (for\ H > H_{SF})$$

Where H is the external magnetic field applied along the easy axis.

To give a brief overview of the equations, the AFMR frequency in Cr_2O_3 from Ref. [42] is reproduced in **Figure 1.16**. The spin-flop field $H_{SF} = \sqrt{2H_A H_E}$ separates the AFM dynamics into two distinct regimes. For $H < H_{\mathrm{SF}}$, the frequencies of two dynamical modes exhibit opposite chirality, which are split by the longitudinal magnetic field into a high-frequency mode (HFM) and a low-frequency mode (LFM). The HFM exhibits right-

handed chirality with respect to the magnetic field, a larger precession cone for sublattice magnetization $\boldsymbol{M_1}$, and carries spin-down angular momentum. In Contrast, the LFM exhibits left-handed chirality with respect to the magnetic field, a larger precession cone for sublattice magnetization $\boldsymbol{M_2}$, and carries spin-up angular momentum. The frequency separation between the two modes increases linearly with increasing H until the ground-state configuration becomes unstable at the critical field H_{SF}. For $H > H_{SF}$, the quasi-ferromagnetic resonance (QFMR) frequency increases monotonically with field.

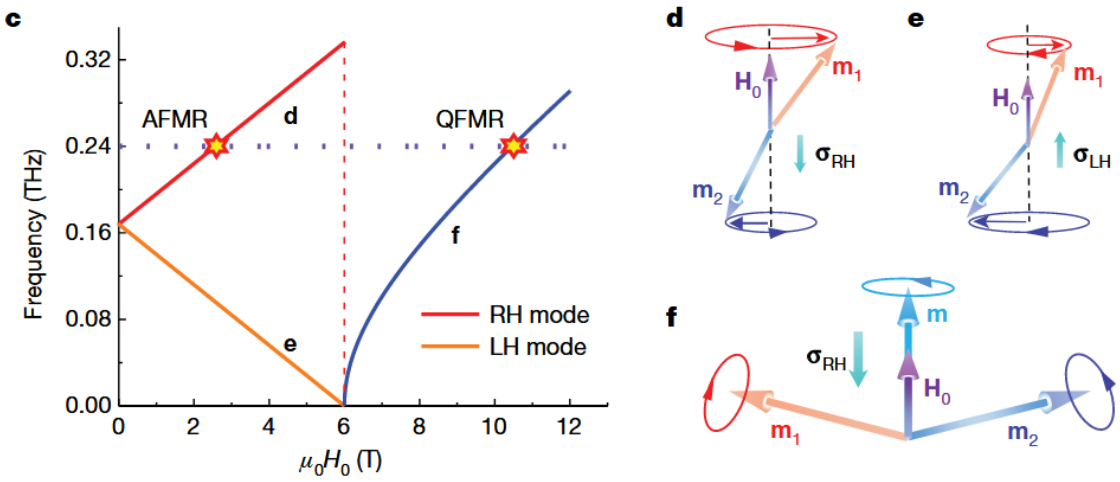


Figure 1.15 AFM Resonance in Cr_2O_3 (a) Calculated AFM resonance frequency ($k = 0$ magnons) as a function of the magnetic field applied along the c-axis of Cr_2O_3 at 0 K. (b) RH mode. (c) LH mode. (d) QFMR mode. Reproduced from Ref. [42].

Chapter 2 Electrical Detection of Single-Domain Néel Vector Reorientation across the Spin-Flop Transition in Cr_2O_3 Crystals

Electrical transport measurements in heterostructures of antiferromagnetic Cr_2O_3 bulk crystals and a thin Pt layer exhibit sharp responses as the Néel vector of the Cr_2O_3 undergoes the spin-flop transition. This abrupt change can arise from several distinct mechanisms including magnetostriction, proximity-induced anomalous Hall, spin Hall anomalous Hall, and spin Hall planar Hall effects. While large Pt devices sensing multiple up/down domains can produce indistinguishable Hall signal jumps due to different initial Néel vector orientations, smaller Pt devices that sense single domains isolate the proximity-induced Hall signals. This allows direct electrical detection of Néel vector reorientation across the spin-flop transition in single domain regions. Furthermore, the single-domain state can be prepared by magnetic field cooling or magnetoelectric cooling. We demonstrate a method to control and characterize almost the three-dimensional orientation of single-domain Néel vectors by exploiting Hall measurements and cooling techniques, crucial for future antiferromagnetic spintronic applications.

2.1 Background and Motivation

The spin-flop transition (SFT) is an important phenomenon in antiferromagnetic (AFM) materials characterized by a sudden rotation of antiparallel spins, and thus the reorientation of the Néel vector $\boldsymbol{L}$, accompanied by canting when an applied magnetic field overcomes the magnetic anisotropy. In bulk crystals, the SFT can be detected using various techniques, including neutron scattering [158–161], magnetometry [162–164], magnetic resonance [42,43,165], and transport methods such as spin Seebeck effect [166–168]. In AFM insulators like Cr_2O_3, electrical transport in an adjacent heavy metal layer, such as Pt, can be sensitive to the spin configurations near the interface. This allows for the electrical detection of the Néel vector reorientation at SFT, providing a convenient and versatile interface-sensitive approach particularly suited to AFM thin films and nanodevices. By exploiting this method, we can gain valuable insights into the Néel vector $\boldsymbol{L}$ at the nanoscale.

2.2 Methods

In this work, we investigate the Néel vector orientations across the SFT through electrical transport measurements in Cr_2O_3/Pt heterostructure devices. We utilize Cr_2O_3 single crystals with thicknesses of 0.5 mm. Two crystal orientations are chosen: $(10\bar{1}0)$ and (0001). In the $(10\bar{1}0)$-oriented crystal, the *c*-axis lies in the surface plane, resulting in a compensated surface. Conversely, in the (0001)-oriented crystal, the *c*-axis is perpendicular to the surface, and the surface spins of a single domain originate from only one AFM sublattice, creating an uncompensated surface. The polished Cr_2O_3 crystal surface is smooth with a root-mean-square (RMS) roughness of approximately 0.2 nm, which is subsequently coated with a 3 or 5 nm thick Pt layer using magnetron sputtering. Photolithography or electron beam lithography is used to define Pt Hall bar or Hall cross patterns with lateral dimensions ranging from 100 μm to 0.1 μm. Transport measurements on these devices are performed using Quantum Design's Physical Property Measurement System (PPMS). More details can be found in **Section 2.6: Supporting Information**.

2.3 Spin Seebeck and Magnetoresistance at Spin-Flop Transition

We start with the $(10\bar{1}0)$-orientation with a compensated surface of Cr_2O_3 on which no intentional net magnetic moments participate in the electrical transport of Pt placed on top. As the in-plane magnetic field is swept along the *c*-axis, the uniaxial direction of Cr_2O_3, there is an abrupt jump at 6 T, the spin-flop field, in the spin Seebeck effect (SSE) response, as shown in **Figure 2.1(a)**, signaling the switching of magnon spin polarization. More details about the SSE features were reported previously [167–169]. This SSE jump marks the discontinuity in spin-wave excitation spectrum in Cr_2O_3. Since the near-90° sudden rotation of static spin configuration occurs at this transition, it is expected to be sensed resistively using Pt [86].

A clear upward jump appears in the longitudinal magnetoresistance (MR) of Pt, $\frac{\Delta R}{R}$, at approximately the same field (**Figure 2.1(b)**). It is tempting to assign this MR jump to the spin-Hall magnetoresistance (SMR) effect just as in bilayers consisting of a ferrimagnetic insulator and a heavy metal [35,77,111,112,170]. However, a closer examination reveals crucial discrepancies. First, as Néel vector ***L*** rotates away from the *c*-axis, i.e., the current flow direction in the device, it should give rise to a downward SMR jump, opposite to the trend observed here. Second, to eliminate the SMR effect, we insert a 10 nm-thick, pinhole-free Al_2O_3 layer between Cr_2O_3 and Pt. Despite this insulating layer, we still observe a similar magnetoresistance upward jump but with a slightly reduced magnitude (**Figure 2.1(c)**). These facts suggest that a spin-independent magnetoresistance mechanism dominates the SMR effect in Cr_2O_3/Pt.

It was known that the magnetostriction effect causes the material to elongate along the *c*-axis while contracting laterally upon the spin-flop transition [171,172]. We find that this effect can quantitatively account for a resistance jump of $\frac{\Delta R}{R} = \frac{2\Delta L}{L} \sim 5.6 \times 10^{-5}$ at 20 K, which is close to our observed value of 4.5×10^{-5} in Cr_2O_3/Pt at 20 K [171,172]. The subtle difference between these two values might be attributed to the SMR effect. Evidently, the magnetostriction-dominated longitudinal magnetoresistance lacks sufficient sensitivity required to probe the spin configurations.

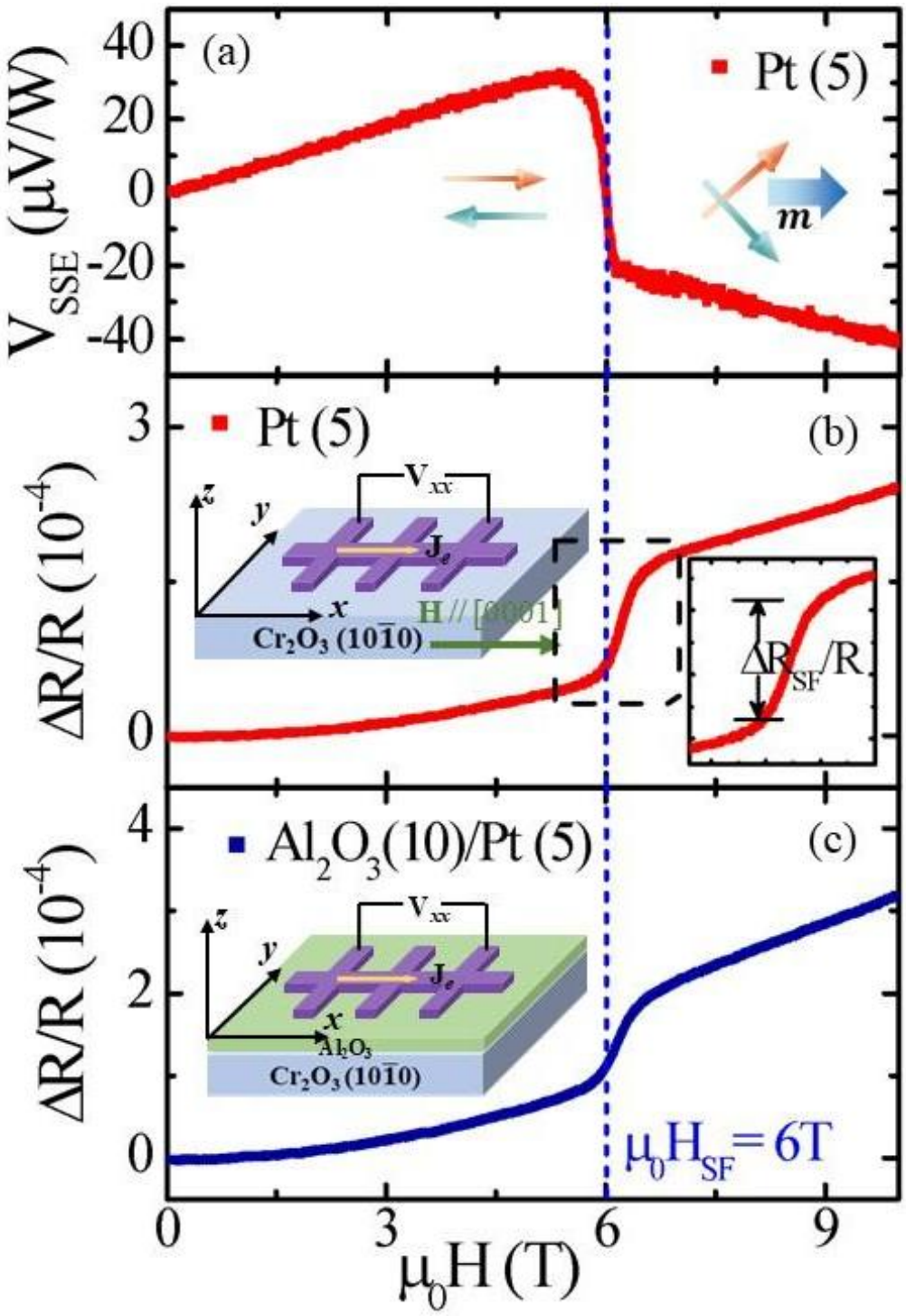


Figure 2.1 Spin-flop Transition of $Cr_2O_3(10\bar{1}0)$ Crystal (a) SFT detected by the SSE at 50 K. (b) SFT-induced resistivity jump in Cr_2O_3/Pt at 20K. (c) SFT-induced resistivity jump in Cr_2O_3/Al_2O_3/Pt at 20K. Insets show the measurement schematics.

2.4 Hall Detection of the Néel Vector

To electrically detect the orientation of ***L*** more decisively, we exploit the Hall effect which is inherently insensitive to the resistance change caused by a magnetostriction effect. By utilizing the uncompensated (0001) surface of Cr_2O_3, we induce a net magnetic moment ***m*** in Pt via the proximity effect. For Cr_2O_3, even above the SFT, the field-induced canting is very small due to the strong exchange interaction relative to the anisotropy. Therefore, the orientation of one sublattice spins can approximately represent that of ***L***, which means that the direction of the induced ***m*** in Pt can serve as a reliable indicator of the direction of ***L***. As ***L*** reorients, the change in the Hall signal can be generated through two mechanisms: the anomalous Hall effect (AHE) arising from m_z, the perpendicular component of ***m***; and the planar Hall effect (PHE) [115,164,173]. We acknowledge that the AHE signals in Cr_2O_3 thin films have been attributed to the proximity-induced magnetic layer at the interface [174,175] or the spin current reflection by the interfacial moments [176–178], both of which are proportional to m_z. The PHE is proportional to either $m_x m_y$ (due to the in-plane components of ***m*** in Pt), or $L_x L_y$ (due to the in-plane components of ***L*** via the spin current generated by the bulk Cr_2O_3), which provides information about the in-plane orientation of ***m*** or ***L***. Unlike the PHE, AHE can detect whether the 180° reversal occurs for ***m*** or ***L***.

2.4.1 Hall Resistance in $50\mu m \times 50\mu m$ Active Area

We perform Hall measurements on a 50 μm wide Cr_2O_3/Pt Hall cross device by passing a current through each of the two orthogonal channels in geometries G and G', as illustrated in **Figure 2.2(a)**. The magnetic field is intentionally tilted slightly away from the *c*-axis, with an in-plane component approximately aligned with the $\varphi = 45°$ direction to maximize the PHE responses above the SFT. As the magnetic field is swept, the transverse resistances R_{yx} in both G and G' are measured, as shown in the inset of **Figure 2.2(b)**. After the linear ordinary Hall effect (OHE) background is subtracted, the corrected Hall signals are presented in the main panel of **Figure 2.2(b)**.

In each Hall channel, sharp jumps occur at ±6 T, the SFT fields where ***m*** and ***L*** abruptly rotate by approximately 90° from out-of-plane to in-plane. Above the SFT, the AHE signal is expected to vanish due to the zero m_z component, but the PHE signal can suddenly jump from zero to a finite value which is proportional to $sin\ 2\varphi$. In theory, both the z-component and the in-plane component of ***m*** and ***L*** are obtained from the AHE and PHE responses, subject to an ambiguity in the in-plane direction between φ and $\varphi + \pi$ [164]. Notably, the two orthogonal channels in G and G' report opposite PHE signals if there is an in-plane ***m*** or ***L*** component.

By averaging the Hall signals from G and G', i.e., $\big(R_H(G) + R_H(G')\big)/2$, we effectively eliminate both the mixed signal from the longitudinal channel due to unintended device geometry asymmetry [179,180] and the PHE signals as discussed above, leaving only the AHE signal, R_{AHE}. Conversely, the difference signal contains only the PHE and geometry-induced mixed signals, which produce opposite signs in G and G' channels. The

well-defined Hall cross devices result in negligible mixing of the longitudinal signal (see **Section 2.6**); therefore, we attribute the half of the difference, i.e., $\big(R_H(G) - R_H(G')\big)/2$, to the PHE signal R_{PHE}.

Figure 2.2(c) displays both the R_{AHE} and R_{PHE} curves. Clearly, the R_{AHE} signal remains nearly flat across the entire field range, showing no observable features at the SFT. The absence of R_{AHE} below the SFT suggests the presence of multiple domains within the $50\mu m \times 50\mu m$ region, leading to a net $\langle m_z \rangle$ of approximately zero. On the other hand, because the R_{PHE} signal cannot distinguish between the two oppositely aligned in-plane directions of $\boldsymbol{L}$, the rotation of $\boldsymbol{L}$ from the initial multi-domain state to the in-plane direction does not result in signal cancellation even if there are spin-flop domains, and therefore produces finite R_{PHE} jumps.

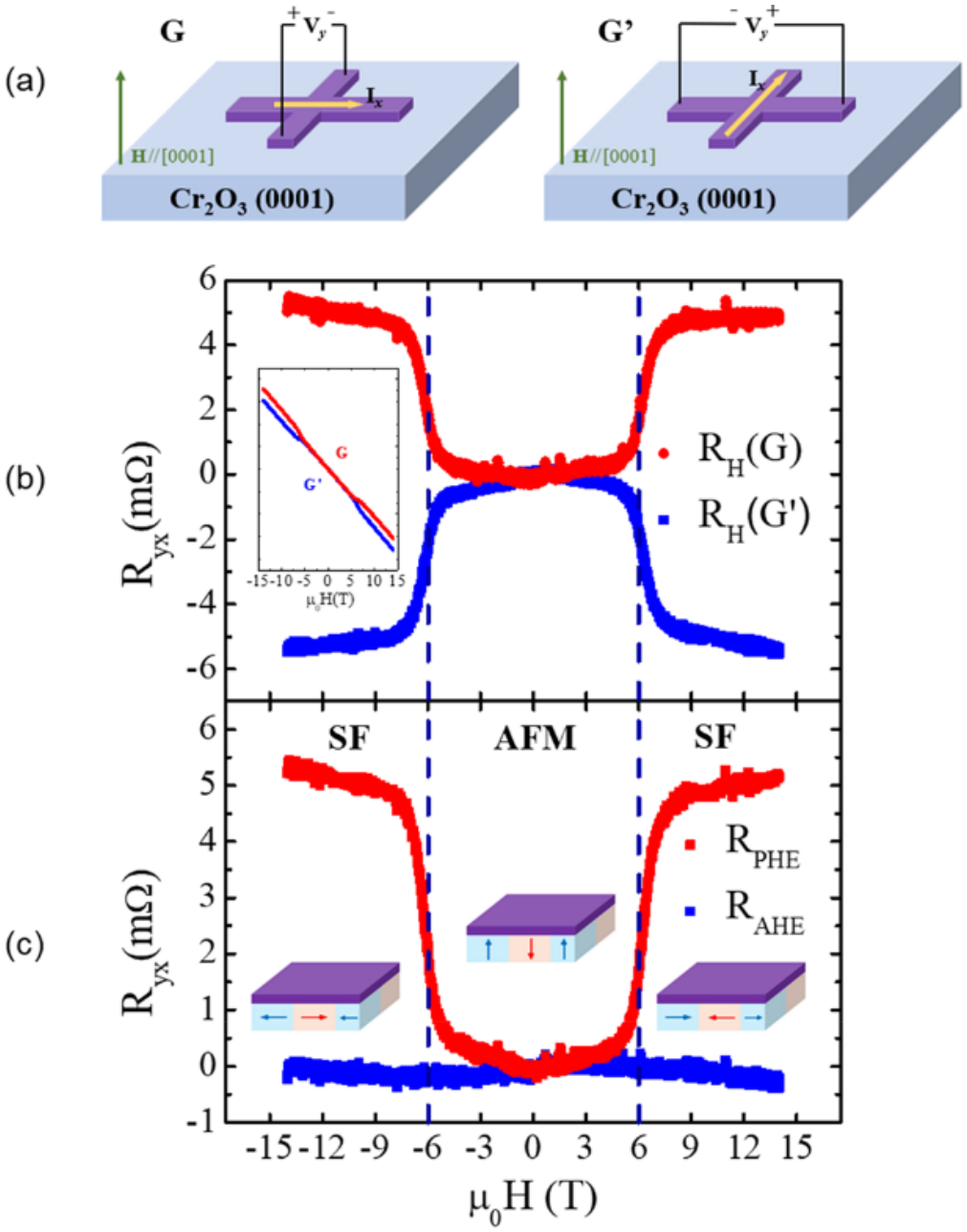


Figure 2.2 Hall Resistance of Cr_2O_3(0001)/Pt in 50μm×50μm Active Area (a) Illustrations of G and G' geometries for Hall measurements. (b) Transverse resistance R_{yx} measured in G (R_H(G)) and G' (R_H(G')) at 2 K by subtracting OHE background from original Hall signals (Inset). (c) R_{AHE} = (R_H(G)+R_H(G'))/2 and R_{PHE} = (R_H(G)-R_H(G'))/2 are displayed. The cartoons show multi-domain spin configurations in antiferromagnetic (AFM) phase and spin-flop (SF) phase.

2.4.2 Hall Resistance in $10\mu m \times 10\mu m$ Active Area

While we have demonstrated the sensitivity of the PHE responses to Néel vector rotation at the SFT, the absence of the AHE signal, resulting from the cancellation of m_z in multiple domains, hinders the determination of the state of the Néel vector below the SFT. To unequivocally detect the proximity-induced AHE signal in Pt below SFT, smaller Hall cross devices capable of probing single domains are necessary. We fabricate smaller Pt Hall cross devices with widths ranging from 10 μm to 0.1 μm using electron beam lithography.

Figure 2.3(a) illustrates the Hall signals, $R_H(G)$, and $R_H(G')$, obtained at 2 K from the G and G' channels of a 10 μm device subjected to zero magnetic field (ZFC) from 320 K, exceeding the Néel temperature (T_N ~ 307 K). Both $R_H(G)$ and $R_H(G')$ signals exhibit a sharp SFT, similar to what was observed in the 50 μm device. However, in contrast to the 50 μm device, wherein $R_H(G)$ and $R_H(G')$ display opposing jump directions, the 10 μm device demonstrates concurrent downward jumps in both signals at the SFT fields. This results in a non-zero R_{AHE} signal below the SFT. This observed finite R_{AHE} is attributed to a net m_z within the 10 μm × 10 μm area, arising from either incomplete m_z cancellation due to multi-domain configurations or a single domain state. This behavior is in marked contrast to that of the 50 μm device.

To influence the ZFC state, field cooling (FC) is performed from 320 K to 2 K under positive (PFC) and negative (NFC) 1 T fields. The corresponding Hall responses, presented in **Figures 2.3(b)** and **Figure 2.3(c)**, demonstrate a near inversion of the R_H(G) and R_H(G') features between PFC and NFC, which suggests opposite signs of m_z resulting

from the application of opposing FC fields. **Figure 2.3(d)**, **2.3(e)**, and **2.3(f)** display the R_{AHE} and R_{PHE} curves for ZFC, PFC, and NFC, respectively. While R_{PHE} curves remain largely unchanged and are approximately field symmetric, R_{AHE} curves display distinct differences. First, the jumps at the SFT fields can be upwards or downwards, depending on FC conditions. Second, disregarding the difference in SFT jump sizes, the overall PFC and NFC responses are inverted. Third, the ZFC curve closely resembles the NFC curve.

The three R_{AHE} curves are plotted together in **Figure 2.3(g)**. Notably, while the NFC and PFC conditions produce two distinct AHE values below the SFT, the two curves converge above the SFT. Moreover, the fact that the ZFC curve is nearly identical to the NFC curve suggests that even the ZFC state is a single-domain state. These results collectively demonstrate that the Néel vector of the single domain can be reversed solely by a cooling magnetic field, which can be electrically detected. While the detailed mechanism by which FC influences AFM domains remains unclear, similar FC effects have been previously reported by other groups [181,182,149,183,174,184]. Such FC effects were tentatively attributed to an above-Néel-temperature memory effect within residual AFM domain walls [183], a phenomenon that warrants further investigation.

It is crucial to observe that, despite the main curve's inversion indicating the reversal of $\boldsymbol{L}$, the features at the SFT fields are not symmetric about the field. In fact, the two FC R_{AHE} curves are not perfectly inverted. By averaging the two FC R_{AHE} curves shown in **Figures 2.3(e)** and **2.3(f)**, we can extract the non-inverted component, R_{AHE_A}, as depicted in **Figure 2.3(h)**. The field-antisymmetric component, R_{AHE_A}, invariant with the cooling field direction, is removed from **Figure 2.3(g)**. This isolates the cooling field-

reversible, field-symmetric components, R_{AHE_S}, as shown in **Figure 2.3(i)**. FC process establishes $\boldsymbol{m}$ and $\boldsymbol{L}$ in one of two single-domain states, indicated by the two plateaus on the R_{AHE_S} curve. During successive low-temperature field sweeps between ±14 T, the R_{AHE_S} curve repeats, demonstrating that $\boldsymbol{m}$ and $\boldsymbol{L}$, once in a single-domain state, maintain their orientation below the SFT and undergo reversible rotation across the SFT, regardless of sweeping field direction. These behaviors are qualitatively different from those reported in thin films where the ferromagnetic-like AHE loops are observed [174,185]. In contrast, the R_{AHE_A} component exhibits a distinct behavior, changing sign with field reversal. Intriguingly, the R_{AHE_A} component peaks near the SFT fields and diminishes with increasing field, where $\boldsymbol{m}$ and $\boldsymbol{L}$ are expected to lie within the film plane. However, in-plane rotation of $\boldsymbol{m}$ and $\boldsymbol{L}$ would not produce an averaged Hall signal. Therefore, we suggest alternative mechanisms, such as the topological Hall effect [74,186–188], induced by spin textures that form when the effective anisotropy weakens near the SFT.

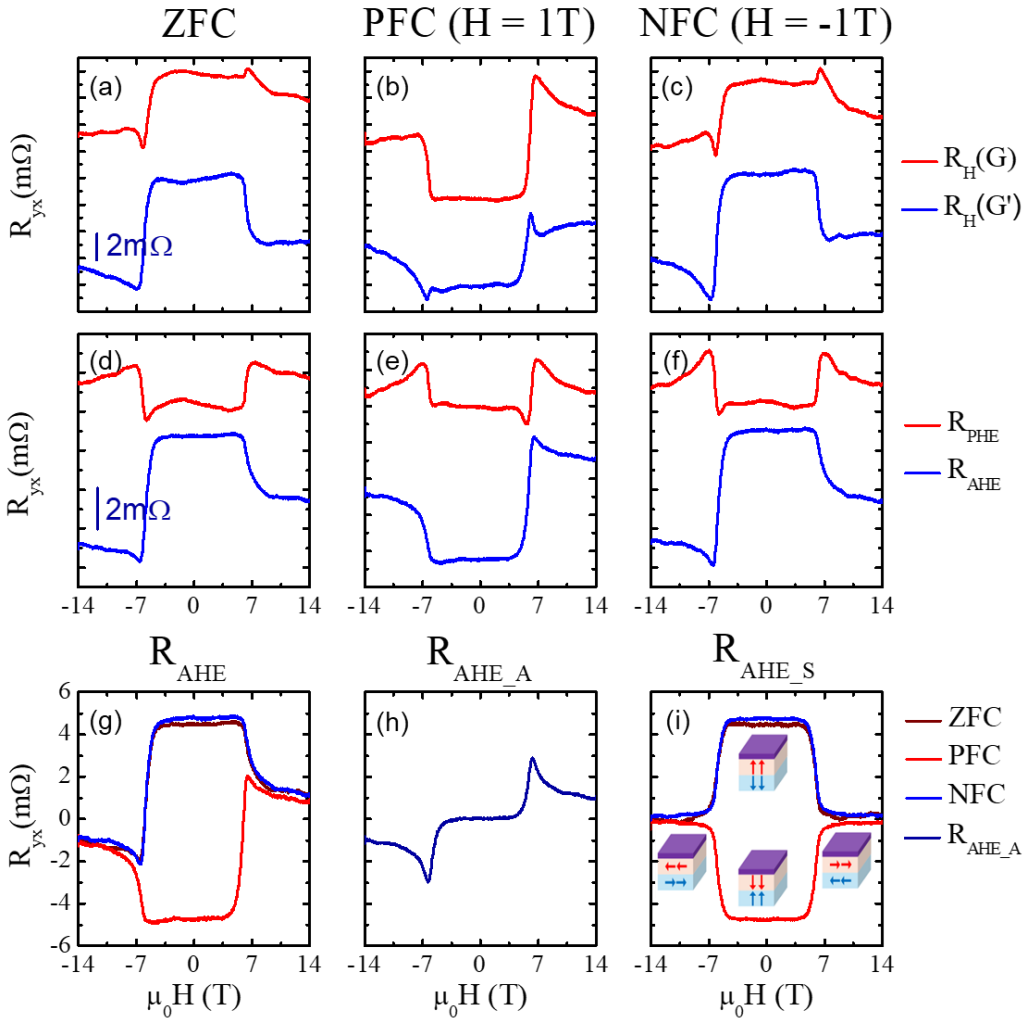


Figure 2.3 Hall Resistance of Cr_2O_3(0001)/Pt in 10μm×10μm Active Area (a-c) R_H measured in G & G' at 2K after (a) zero field cooling (b) positive field cooling (c) negative field cooling. (d-f) Extracted R_{AHE} & R_{PHE} at 2K after (d) zero field cooling (e) positive field cooling (f) negative field cooling. (g) R_{AHE} (h) R_{AHE_A} (i) R_{AHE_S}. The cartoons show the corresponding spin configurations in a single domain.

2.4.3 Controlling Néel Vector by Field Cooling and Magnetoelectric Coupling

We have demonstrated that the cooling field direction can reliably toggle the Néel vector state with the single-domain region under the 10 μm Pt Hall cross device. To validate this FC effect, we have performed similar FC experiments on four additional Hall cross devices, fabricated on a separate Cr_2O_3 crystal using electron beam lithography and Pt etching (see **Section 2.6.3**). These devices, A (10nm), B (10 μm), C (1 μm), and D (0.1 μm), different in width, are shown in **Figure 2.4**. The upper two rows present the R_{AHE} results for all four devices under 1 T positive (PFC) and negative (NPC) fields, with arrows indicating the corresponding Néel vector orientations. Notably, all devices, regardless of size, exhibit nearly identical R_{AHE} plateau magnitudes (~ 3 $m\Omega$), confirming that they sense single domains. Furthermore, the Néel vector is consistently reversed between PFC and NFC, reinforcing our previous findings. Interestingly, despite being located up to approximately 0.8 mm from each other on the same substrate and subjected to the identical cooling field, the Néel vector orientation is not uniform across the substrate. These findings indicate that while FC is effective in switching Néel vector orientations, it is not sufficient for the deterministic selection of a specific orientation to achieve a single AFM domain across the entire material.

Cr_2O_3 is a magnetoelectric material where the Néel vector can be controlled by both electric and magnetic fields [141–143,145–147,149,181,183,189–196]. Utilizing Pt Hall crosses as the top electrode and silver paint on the bottom surface as the bottom electrode, we demonstrate deterministic Néel vector orientation setting via magnetoelectric cooling (MEC). The lower two rows of **Figure 2.4** show the R_{AHE} results for three devices

subjected to MEC with a 1 T magnetic field and ±50 V across the 0.5 mm thick Cr_2O_3 crystal, corresponding to an electric field of 1 kV/cm. With +50 V (PMEC), the Néel vector is consistently set downward in three tested devices. Conversely, a -50 V (NMEC) results in an upward Néel vector direction in the same devices, independent of their size. This confirms the deterministic control of Néel vector orientation using MEC.

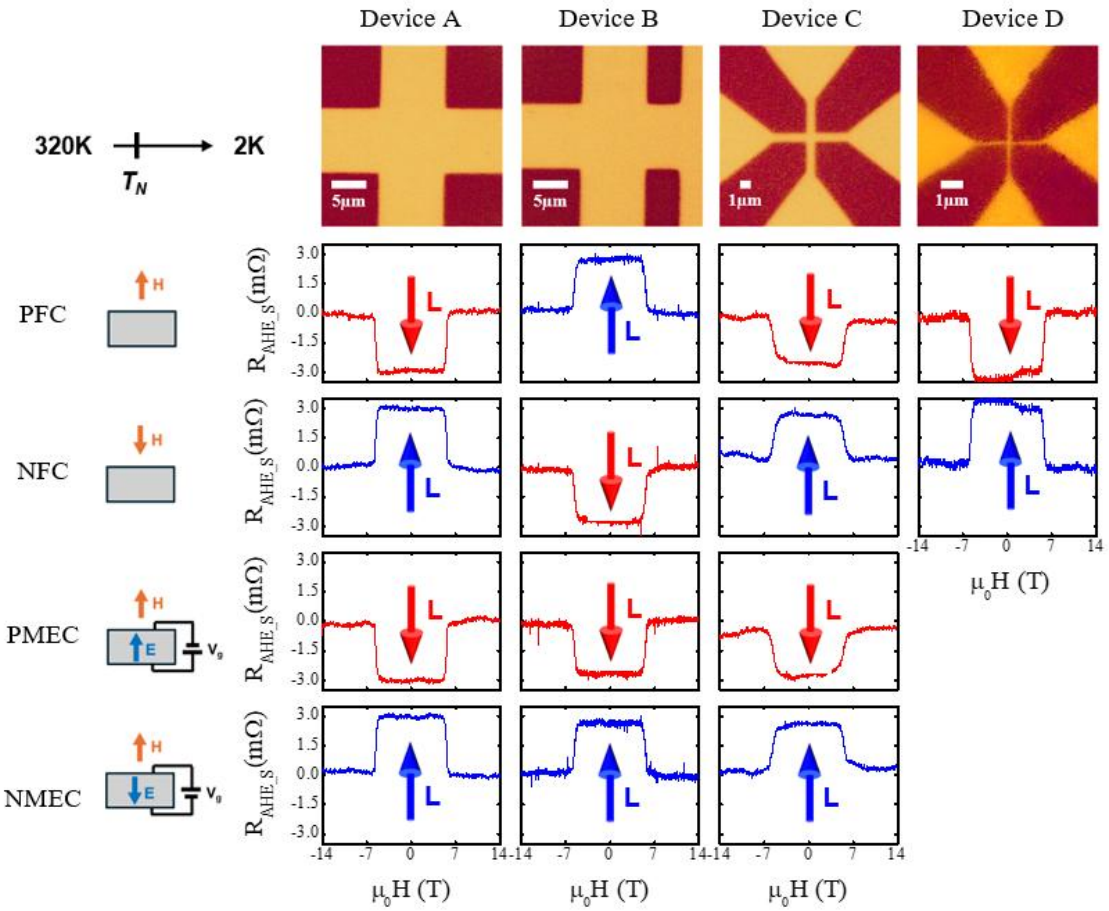


Figure 2.4 Néel Vector Orientations under Different Conditions The upper optical micrographs present the four Hall cross devices being tested. The devices are cooled down from 320K to 2K under PFC, NFC, PMEC, and NMEC conditions. R_{AHE_S} vs. applied field are extracted from spinning Hall measurements and plotted accordingly. Arrows labeled with "L" represent Néel vector orientations inferred from R_{AHE_S}.

2.4.4 Temperature Dependance of AHE and PHE

Both the PHE and proximity-induced AHE signals in a single domain should be proportional to the magnitude of the Néel vector and other relevant parameters such as the spin-mixing conductance and anomalous Hall angle. The temperature dependence of these two signals is measured and shown in **Figure 2.5** for Device A in **Figure 2.4**. As the Néel temperature is approached, both signals decrease as expected. The overall temperature dependence exhibits a broad maximum around 100 K. A similar non-monotonic response was observed in the magneto-optical Kerr effect signal from the top Cr_2O_3 surface [147]. The broad peaks in both AHE and PHE likely originate from the $Cr_2O_3(0001)$ sublattice moment and therefore the magnitude of the Néel vector, both of which are imprinted in the Hall responses of Pt.

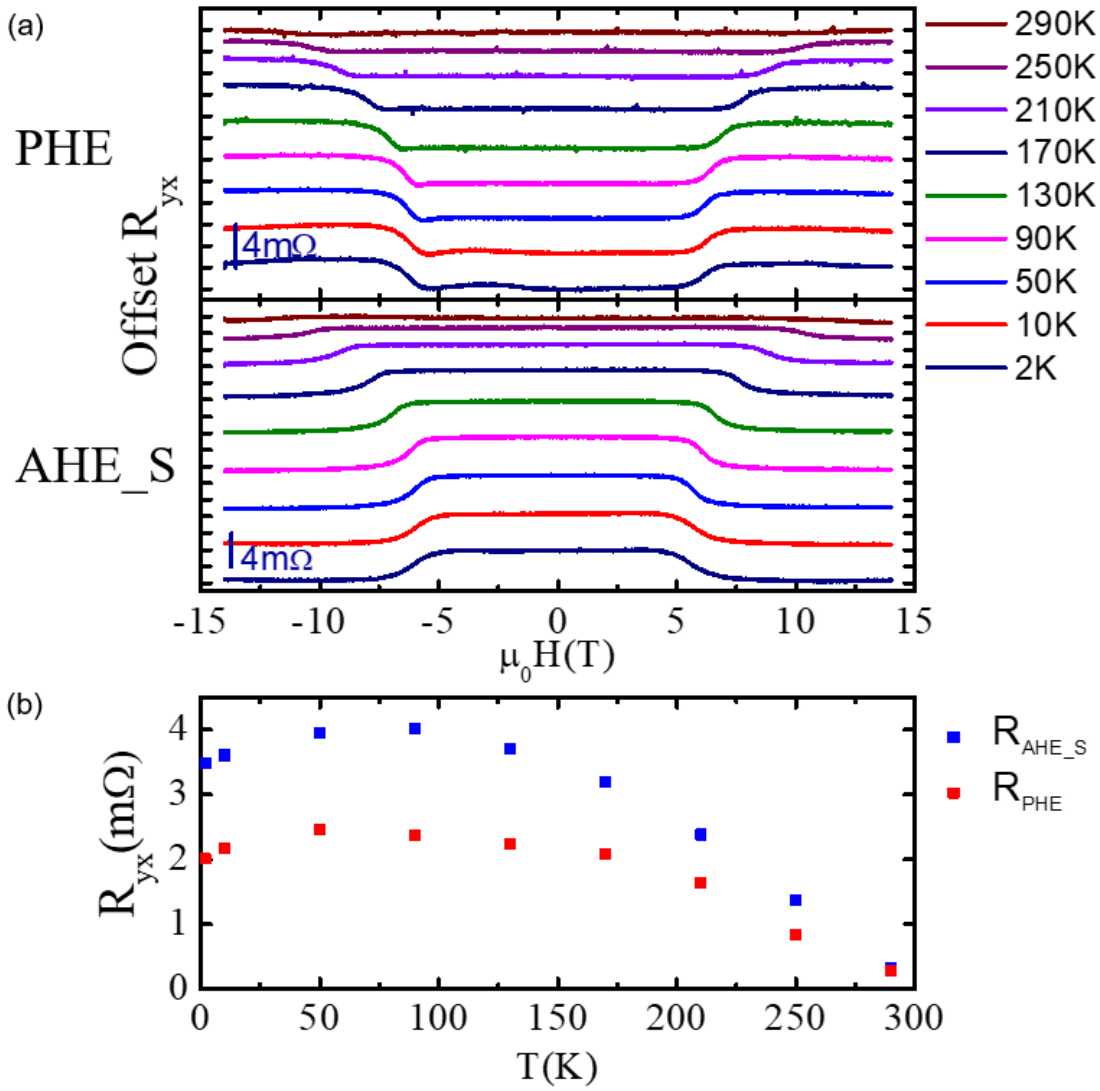


Figure 2.5 Temperature Dependence of AHE and PHE (a) R_{AHE_S} & R_{PHE} curves at different temperatures. (b) Corresponding R_{AHE_S} and R_{PHE} magnitudes vs. temperature.

2.5 Summary

In conclusion, we present the unequivocal electrical detection of single-domain Néel vector reorientation across the SFT of Cr_2O_3, using micro- and nano-fabricated Pt Hall cross devices. Magnetoelectric cooling provides deterministic control of the single-domain Néel vector, unlike the domain configuration changes induced by magnetic field cooling. This precise manipulation and electrical readout of the AFM order parameter at the single-domain level represents a key milestone in the development of AFM spintronics.

2.6 Supporting Information

In this section, I present additional experimental details, complementary measurements, and discussions for a comprehensive understanding of this work.

2.6.1 Magnetometry Characterization of Cr_2O_3 Bulk Single Crystal

Prior to transport measurements, we first verify the easy-axis AFM phase of Cr_2O_3 by performing magnetometry characterization as shown in **Figure 2.6**. We choose a (0001)-oriented single crystal with dimensions of 5 mm × 5 mm × 0.5 mm (inset of **Figure 2.6(a)**) for the characterization. **Figure 2.6(a)** shows the temperature dependence of the magnetic susceptibility without external magnetic field. Interestingly, we observed a characteristic increase with temperature up to the Néel temperature ($T_N \approx 307$ K), followed by a cusp and a nearly temperature-independent behavior above T_N. This temperature dependence differs from that of conventional antiferromagnets, where the susceptibility typically follows Curie–Weiss behavior and decreases as temperature rises above T_N [197,198]. The anomalously flat susceptibility in Cr_2O_3 has been reported previously [164,165,183,199], and may be attributed to the persistence of short-range antiferromagnetic correlations above the Néel temperature.

Figure 2.6(b) presents the field-dependent magnetic moment *m* (red curve) and *dm/dH* (blue curve) at T = 10K, with the magnetic field $\mu_0 H$ applied along the easy-axis direction. When the applied field is below 6 T, the magnetic moment remains close to zero. Upon increasing the positive (negative) magnetic field to 6 Tesla, a sharp increase

(decrease) of moment is observed. This is consistent with spin-flop transition, a hallmark behavior of easy-axis AFMs, characterizing the reorientation of the Néel from easy-axis to a direction perpendicular to the applied field, with a small spin canting aligned in the same direction of the applied field. This small canting creates a detectable net magnetic moment in the crystal, which can therefore be picked up by magnetometry measurement. The derivative *dm/dH* exhibits two symmetric peaks near ±6 T, in good agreement with the reported spin-flop transition field H_{SF} of Cr_2O_3 at low temperature [42]. **Figure 2.6(c)** shows the Quantum Design's Magnetic Properties Measurement System (MPMS) used to perform the magnetometry characterizations. These results clearly confirm that the Cr_2O_3 single crystal exhibits an easy-axis AFM phase below 307 K and undergoes a spin-flop transition above 6 T at low temperature.

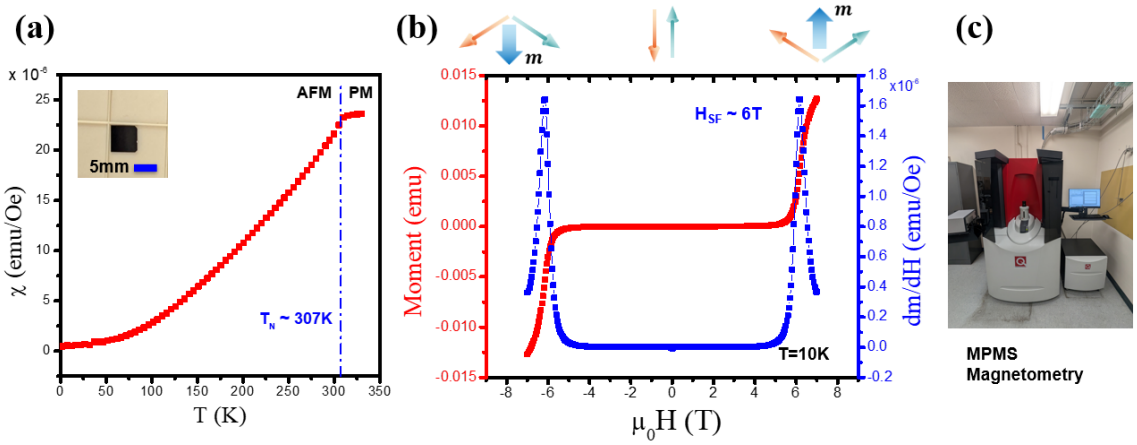


Figure 2.6 Magnetometry Characterization of the (0001)-Oriented Cr_2O_3 Single Crystal (a) Susceptibility χ vs. T, the inset shows the image of the Cr_2O_3 single crystal. (b) Moment m (red) & dm/dH (blue) vs. μ_0H, spin configurations below and above spin-flop transition are shown in the schematic. (c) The image of the MPMS system.

2.6.2 Fabrication and Characterization of $Cr_2O_3(10\bar{1}0)$/Pt Heterostructures

Prior to device fabrication, to ensure the interface quality, the surface of Cr_2O_3 crystal was prepared by chemical mechanical polishing (CMP), followed by standard solvent cleaning and gentle O_2 plasma ashing. The atomic force microscopy image of the surface is shown in **Figure 2.7(a)**. After the treatment, the surface exhibits atomic smoothness with a root-mean-square (RMS) roughness around 0.2 nm. With this high-quality surface, we proceed with the fabrication of different heterostructure devices to serve the purposes for different transport studies (SSE or MR studies).

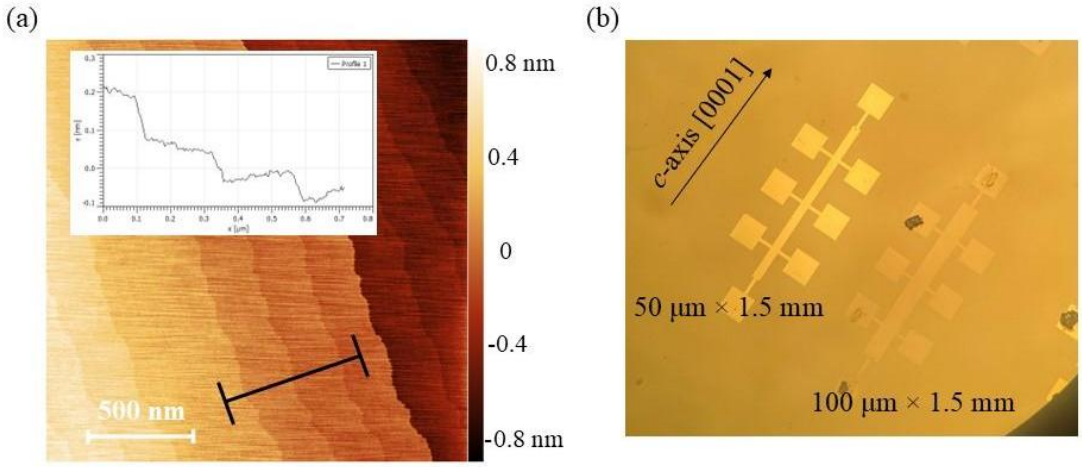


Figure 2.7 Fabrication and Characterization of $Cr_2O_3(10\bar{1}0)$/Pt Heterostructures (a) Atomic force microscopy image of $Cr_2O_3(10\bar{1}0)$ surface before fabrication. It shows clear atomic terraces on which the RMS roughness (within the white box) is about 0.2 nm. (b) Optical image of Hall bar devices with a 5 nm thick Pt layer fabricated on the atomically flat $Cr_2O_3(10\bar{1}0)$ surface.

Figure 2.7(b) shows the optical image of Pt Hall bar devices fabricated on top of the Cr_2O_3 surface used for MR measurement. The Hall bar patterns are defined by

photolithography to form a 50 μm or 100 μm wide and 1.5 mm long current channel oriented parallel to [0001], i.e., the c-axis direction which is also the easy axis of Cr_2O_3. We deposit a 5 nm thin Pt layer on Cr_2O_3, with or without a 10 nm thin Al_2O_3 insertion layer to distinguish the origin of MR associated with the spin-flop transition.

2.6.3 Fabrication and Characterization of Cr_2O_3(0001)/Pt Heterostructures

In this study, we employ commercial Cr_2O_3(0001) single crystals with thicknesses of 0.5 mm. Polishing of the surface is performed to improve the surface smoothness, which involves mechanical polishing (MP) followed by chemical mechanical polishing (CMP). **Figure 2.8(a)** presents an atomic force microscopy image of the surface after CMP, revealing a smooth finish with RMS roughness of 0.2 nm in a 5 μm x 5 μm area, which is satisfactory for the subsequent fabrication of Cr_2O_3/Pt heterostructures.

The Pt Hall cross devices are fabricated using either of two distinct methods. In the first method, electron beam lithography is used to define the Hall bar or Hall cross areas, followed by the deposition of a 3 nm or 5 nm Pt layer via magnetron sputtering, and then liftoff. Devices used for the test in **Section 2.4.1** and **Section 2.4.2** are fabricated using this method. In contrast, for devices used for the test in **Section 2.4.3**, a 5 nm Pt layer is deposited onto the Cr_2O_3 (0001) crystal by magnetron sputtering first and subsequently patterned into Hall cross devices by electron beam lithography and physical dry etching with Ar plasma. For both methods, post-annealing at 400°C or 450°C is performed to eliminate potential contamination and enhance the Pt quality without influencing Cr_2O_3 properties.

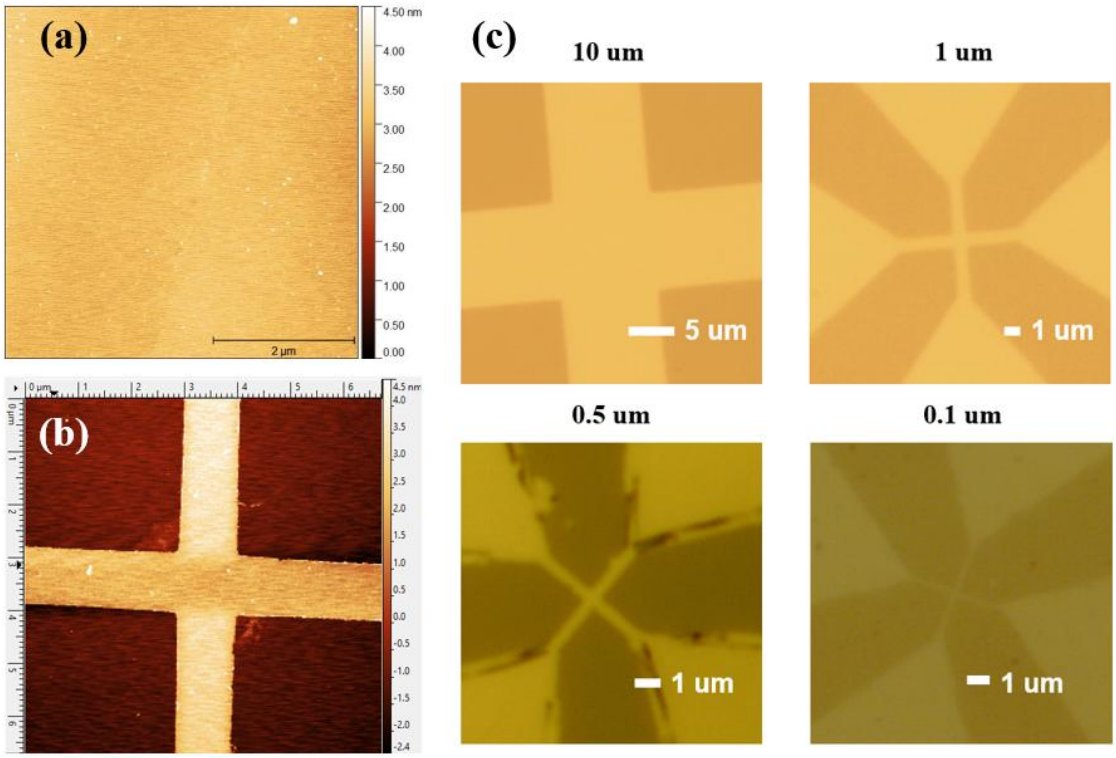


Figure 2.8 Fabrication and Characterization of Cr_2O_3(0001)/Pt Heterostructures (a) Atomic force microscopy image of the polished Cr_2O_3(0001) surface in a 5 µm x 5 µm area. (b) Atomic force microscopy image of a 1 µm Hall cross device. (c) Optical images for Pt Hall cross devices ranging from 0.1 µm to 10 µm.

2.6.4 Magnetoresistance and Hall Measurements

Transport measurements on these devices are performed using Quantum Design's Physical Property Measurement System shown in **Figure 2.9**. A low-frequency sinusoidal AC current, typically 7 Hz or 13 Hz, is applied to the Pt Hall bar or Hall cross devices using a Keithley 6221 current source, while the longitudinal and transverse first harmonic voltage responses are measured with a SR830 lock-in amplifier. For the Cr_2O_3(0001) crystal, an external magnetic field is applied out-of-plane along the easy axis (c-axis [0001]) with a slight tilt to maximize PHE signal during the transport measurements. The

x, y, and z axes directions follow the right-hand rule. The recorded resistances are defined as follows:

$$R_{xx} = \frac{V_x}{I_x}$$

$$R_{yx} = \frac{V_y}{I_x}$$

Here, I_x refers to the RMS value of the AC current applied along the x-direction, while V_x and V_y represent the first harmonic longitudinal and transverse voltage responses, respectively.

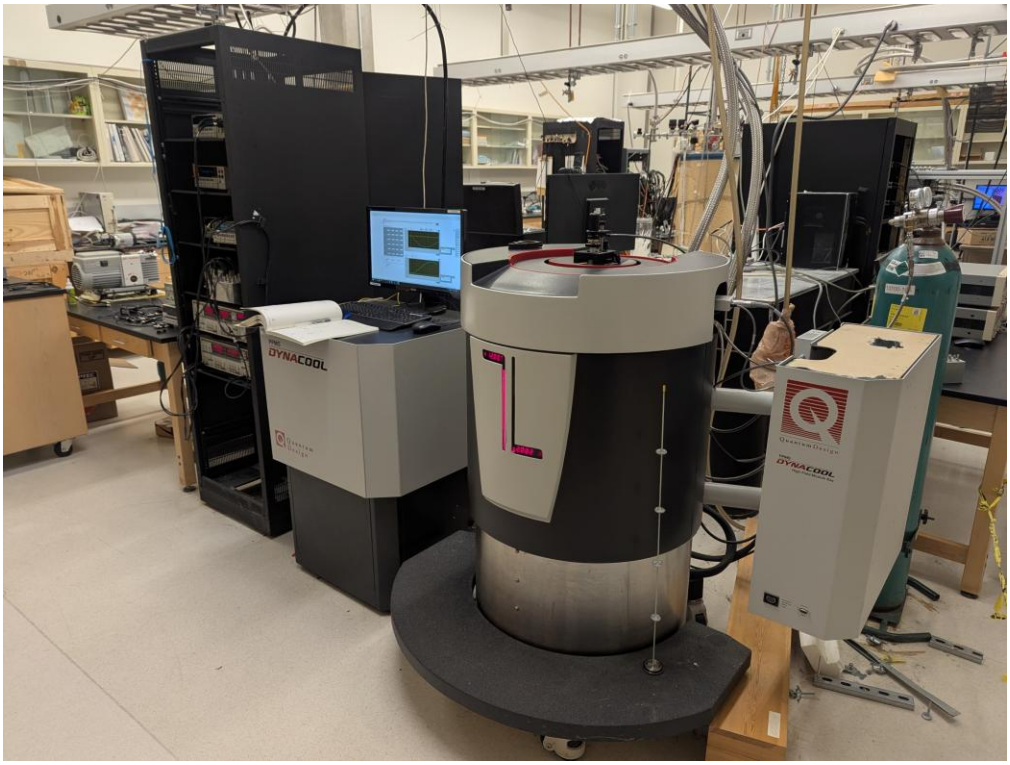


Figure 2.9 Physical Properties Measurements System PPMS system from Dr. Jing Shi's group at UC Riverside. Typical low-frequency AC technique is applied for magnetotransport studies.

2.6.5 Spin Seebeck Effect Measurements

SSE measurement is carried out using the same techniques as our previous studies [168,169]. As shown in **Figure 2.10(a),** we utilize the standard longitudinal SSE geometry with 5 nm thin Pt detector. To drive the SSE signal, a temperature gradient is created by injecting an AC current with frequency ω into a 15 nm thick Pt heater. The heater is placed on top and separated from the Pt detector by a 100 nm thick insulating Al_2O_3 layer, hence resulting in a SSE response, V_{SSE}, oscillating with frequency 2ω in the detector, which is picked up by a SR830 lock-in amplifier. An optical image of a typical SSE device (**Figure 2.10(b)**) shows both the top heater and bottom detector geometry.

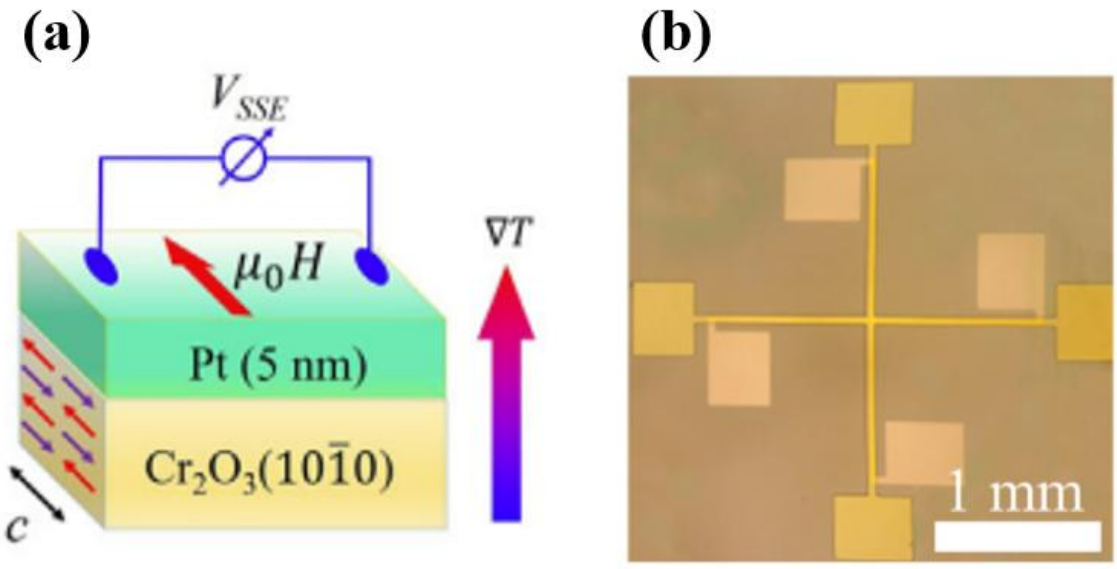


Figure 2.10 Spin Seebeck Measurements (a) Device schematic for SSE measurements in $Cr_2O_3(10\bar{1}0)$/Pt reproduced from Ref. [168]. (b) Optical image of a sample SSE device reproduced from Ref. [169].

2.6.6 Temperature Dependence of Magnetostriction Effect

When performing MR measurements in Cr_2O_3 $(10\bar{1}0)$ /Pt, we observe a geometrically induced resistivity change ΔR_{SF} at H_{SF} due to magnetostriction effect (see the inset of **Figure 2.11**). This is further evident by the insertion of a 10 nm thick Al_2O_3 layer between Cr_2O_3 and Pt, by which ΔR_{SF} has no significant change. We subsequently study the temperature dependence of ΔR_{SF} in both Cr_2O_3/Pt (5nm) and Cr_2O_3/Al_2O_3 (10nm)/Pt (5nm) and the result is plotted in **Figure 2.11**. At the measured temperature range (5K-300K), ΔR_{SF} show little difference between the two heterostructure stacks. The value of ΔR_{SF} is small at 300K, and increases monotonically when the temperature decreases to 50K, then slightly decreases at lower temperatures.

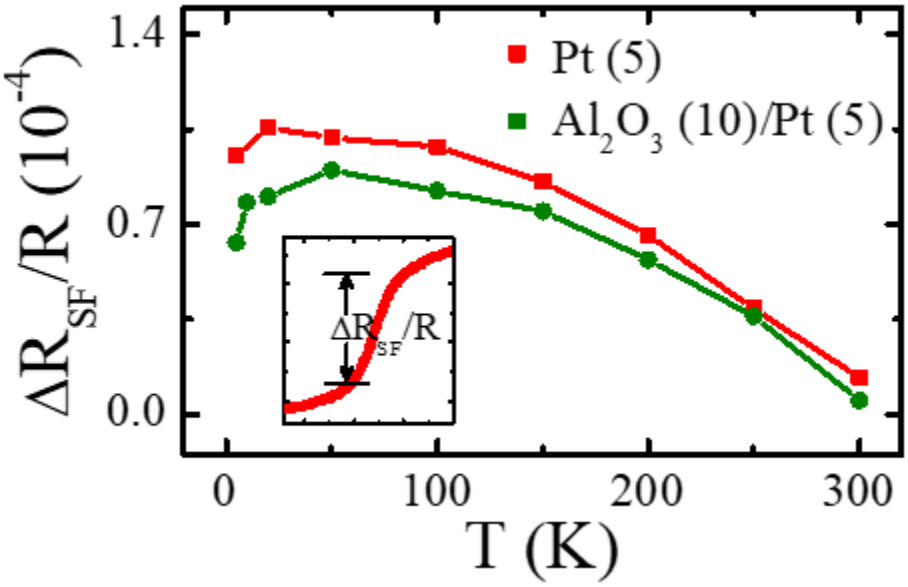


Figure 2.11 Temperature Dependence of Magnetostriction Effect Inset show ΔR_{SF} at spin-flop transition.

2.6.7 Planar Hall Effect and Geometry-Induced Mixing Signals

When performing Hall measurements, a geometry-induced mixing of the longitudinal R_{xx} signal into the Hall terminals is inevitable. This mixed signal has the opposite signs when the voltage measurements are interchanged between two orthogonal geometries, G and G' [179,180], mimicking the jumps typically associated with the planar Hall effect (PHE) at the spin-flop transition (SFT). This mixing effect can potentially contaminate the signal defined as $R_{PHE} = (R_H(\mathrm{G}) - R_H(\mathrm{G}'))/2$. However, this effect can be minimized with a precisely defined Hall cross geometry that reduces misalignment between the Hall terminals and the equipotentials of the current flow.

In **Figure 2.8**, optical images and atomic force microscopy images reveal that the Hall cross structures, ranging from 0.1 μm to 10 μm, are sharply defined with well-formed cross shapes with uniform thickness. This precise geometry is crucial for accurately separating longitudinal and transverse resistances. In an ideal Hall cross, the transverse signal remains largely independent of the longitudinal resistance, as the orthogonal geometry minimizes potential spillover from R_{xx} into the Hall resistance R_{yx}.

We further provide a comparison of R_{xx} and R_{PHE} data for the 10 μm device, shown in **Figure 2.12**. It reveals that R_{xx} is symmetric with respect to the magnetic field, forming a V-shape under field sweep, with a slight decrease in resistance at the SFT field. If this signal were positively or negatively mixed into the Hall channels, we would expect a similar V-shape with a decrease in resistance, or an inverted V-shape with increased resistance, in R_{PHE}. However, the R_{PHE} signal remains nearly flat at low fields, without any apparent V-shape, and exhibits a prominent upward jump at the SFT. This behavior is

consistent across all devices presented in this study. The overall shape of the curve strongly suggests that the signal is dominated by the PHE, with minimal contamination from R_{xx} mixing.

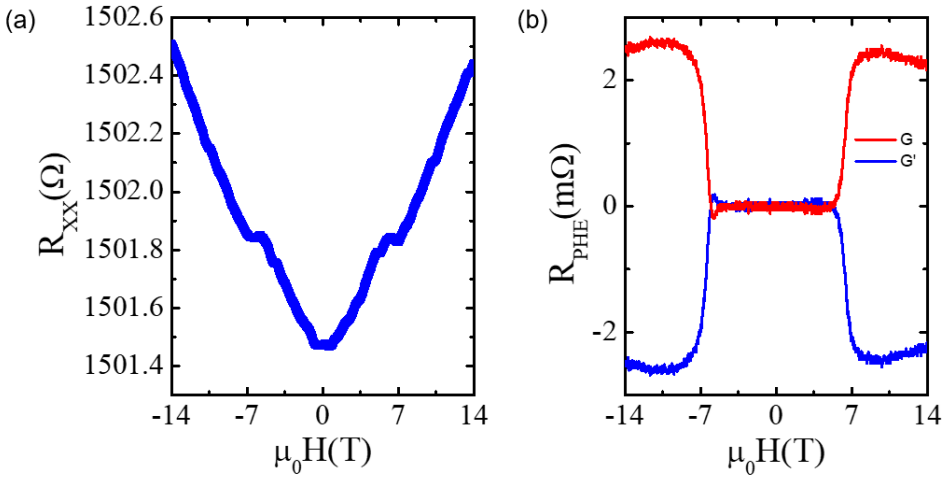


Figure 2.12 Comparison Between R_{xx} and R_{PHE} (a)There are small downward jumps at the SFT superimposed on the overall V-shape R_{xx} background. (b) The PHE signals are dominated by the jumps. If these jumps were due to mixing of the R_{xx} signal, the V-shape background would appear together with and dominate the jumps.

The consistent characteristics observed across all devices underscore the robustness of the fabrication quality and measurement setup. Given the well-defined geometry, smooth thickness verified by optical and atomic force microscopy imaging, and the consistent behavior in R_{xx} and R_{PHE} signals, it is reasonable to conclude that the influence of R_{xx} on R_{yx} is minimal. The precise design and fabrication of the Hall crosses play a crucial role in ensuring accurate Hall measurements with negligible R_{xx} interference.

2.6.8 A Brief Summary of the Hall Resistance

Probing the SFT in antiferromagnetic (AFM) materials provides key insights into the Néel vector $\boldsymbol{L}$, the order parameter of AFM materials. Our Hall measurements in a Pt layer atop a Cr_2O_3(0001) crystal reveal a sharp jump in the Hall signal at the SFT field. While a prior study attributed this signal to the PHE [164], we have identified additional components, including an anomalous Hall effect (AHE) induced by the exchange field from Cr_2O_3's boundary magnetization, denoted as R_{AHE_S}, and an AHE contribution possibly arising from spin textures, denoted as R_{AHE_A}, thus yield an expression for the Hall resistance $R_H = R_{OHE} + R_{PHE} + R_{AHE_S} + R_{AHE_A}$.

Figure 2.13 illustrates our approach to disentangling the contributions from R_{PHE}, R_{AHE_S}, and R_{AHE_A} in a 10 μm Hall cross device (OHE is precluded). At the SFT, the Néel vector rotates from out-of-plane (OOP) to in-plane (IP), resulting in the loss of $\boldsymbol{L}_z$, the OOP Néel vector component, and the emergence of $\boldsymbol{L}_x\boldsymbol{L}_y$, associated with the IP component. The PHE signal, sensitive only to the IP component, is extracted as the differential response between the geometries R_H(G) and R_H(G'). Notably, R_{PHE} is nearly zero below the two SFT fields but jumps to a finite value above them, consistent with the emergence of $\boldsymbol{L}_x\boldsymbol{L}_y$. Additionally, when the field direction is reversed above the SFT, the Néel vector maintains the same $\boldsymbol{L}_x\boldsymbol{L}_y$ magnitude, resulting in a symmetric R_{PHE} signal across positive and negative SFT. The PHE signal can also arise from the IP component of proximity-induced magnetic moment in Pt.

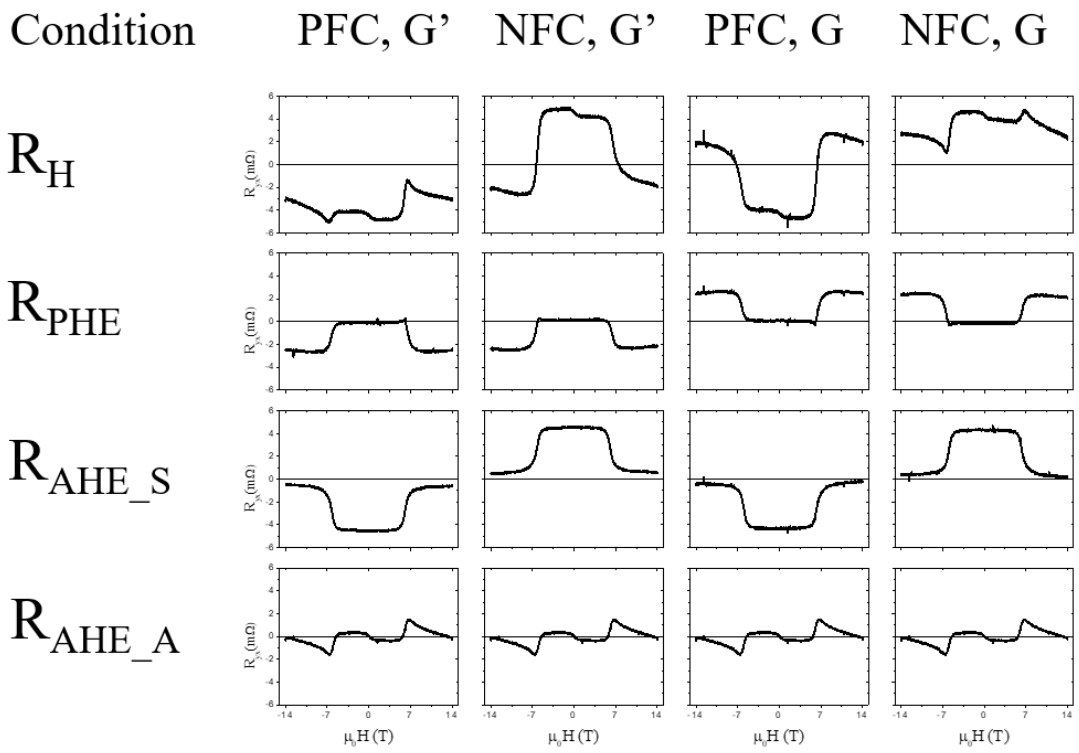


Figure 2.13 A Brief Summary of the Hall Resistance For the data presented here, the measurement is carried out at 90 K. OHE is treated as a dominant linear contribution and precluded from the displayed R_H. The decomposition of R_H into R_{PHE}, R_{AHE_S}, and R_{AHE_A} are presented.

In contrast, R_{AHE_S} is sensitive solely to $\boldsymbol{L}_z$ via a proximity-induced moment in Pt. Significantly, R_H measurements taken under positive field cooling (PFC) and negative field cooling (NFC) show a two-level separation below SFT, which converges above it, consistent with the expected behavior of $\boldsymbol{L}_z$. Thus, we attribute the distinction between R_H(PFC) and R_H(NFC) to R_{AHE_S}. Notably, R_{AHE_S} is field-symmetric and toggles between two distinct values below SFT, reflecting the binary Néel vector states, a feature essential for AFM spintronics applications [122,123,125,200].

Finally, the remaining signal, R_{AHE_A}, survives after averaging the signals from the two orthogonal channels and different cooling conditions. It is nearly perfect H-antisymmetric. As discussed, the feature at the SFT may arise from a chiral spin texture forming when effective anisotropy weakens. However, in contrast to the measurements taken at 2K where R_{AHE_A} is flat below SFT, here we observed another anomaly, a nonlinear AHE near $H = 0$.

2.6.9 On the Anomaly in AHE

Figure 2.14 shows the field dependence of R_{AHE_A} at various temperatures. Interestingly, in addition to the jump observed at the spin-flop transition (marked by the blue dashed line), a low-field nonlinear AHE signal also appears (circled by the red dashed line). These two anomalies, temporarily denoted as ΔR_{ASF} and ΔR_{ALH}, exhibit distinct temperature dependences. ΔR_{ASF} is prominent at low temperatures and gradually diminishes as the temperature approaches room temperature. In contrast, ΔR_{ALH} is pronounced at higher temperatures, remaining observable even above the Néel temperature, but weakens upon cooling. This contrasting temperature behavior indicates that the two effects likely originate from different mechanisms.

ΔR_{ASF} is presumably related to the antiferromagnetic order of Cr_2O_3, whereas ΔR_{ALH} is likely unrelated to it. Previous studies on Cr_2O_3/Pt bilayers have reported Hall resistance features similar to our observation of ΔR_{ALH}, which persist above the Néel temperature [175,177,185,187], although in our case the feature appears at a lower temperature (~90 K), which is less commonly observed. Moriyama *et al.* (2020) [175]

performed first-principles calculations for Cr_2O_3/Pt and suggested that this signal (They referred to as a "giant anomalous Hall effect") may be intrinsic to the Cr_2O_3/Pt interface, arising from a chiral spin structure in momentum space.

Nevertheless, these interpretations require further experimental and theoretical investigation. Other possible explanations for the observed signals include unexpected magnetic moments. The ΔR_{ASF} feature reported here for the first time represents a novel phenomenon whose origin remains to be elucidated.

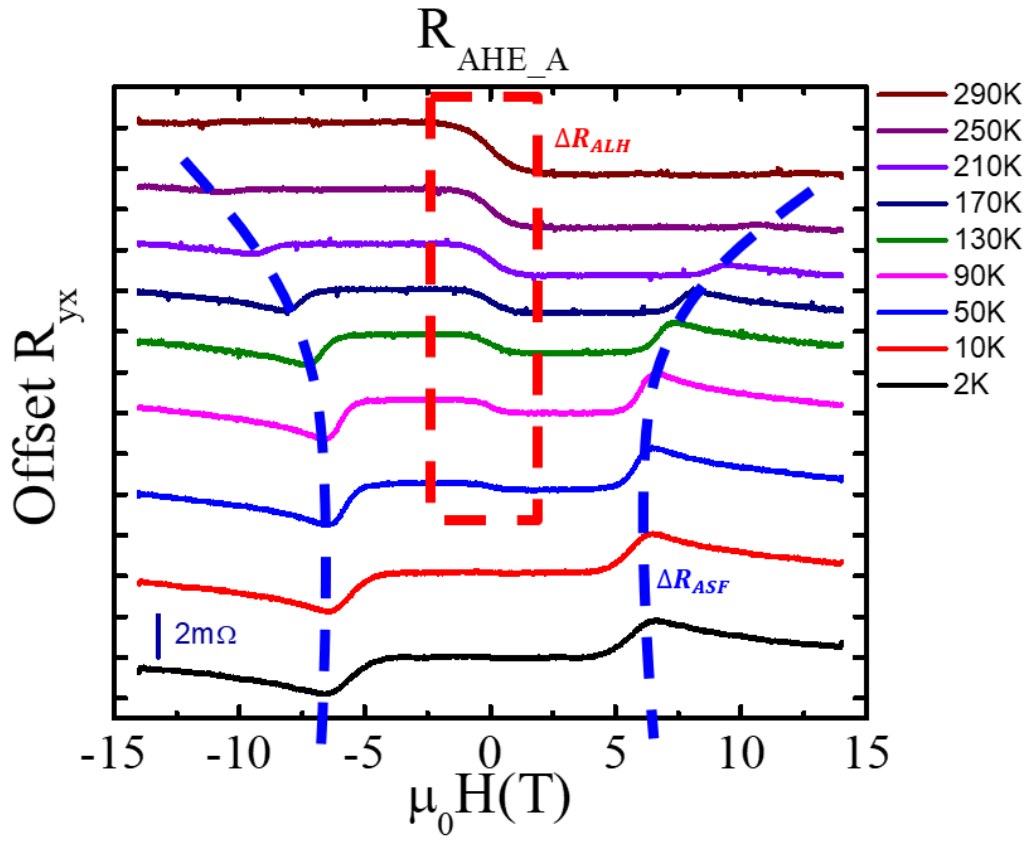


Figure 2.14 Temperature Dependence of R_{AHE_A} The AHE at the SFT (ΔR_{ASF}, blue dashed line) and low magnetic fields (ΔR_{ALH}, red dashed frame) exhibit distinct temperature dependence.

Chapter 3 Dual Ferromagnetic and Ferroelectric Dynamics in Linear Magnetoelectric Cr_2O_3

The antiferromagnetic order parameter, defined by the Néel vector in collinear antiferromagnets like Cr_2O_3, is highly desirable for next-generation, low-dissipation memory. We demonstrate precise, non-volatile switching of the Néel vector via the linear magnetoelectric effect in Cr_2O_3, with the two stable states effectively read out using the anomalous Hall resistance in an adjacent Pt detector layer. Crucially, we observe a pronounced history-dependent training effect in the AFM domain dynamics that enables state tuning. Specifically, cyclic magnetic field with fixed electric field training induces magnetic softening through domain wall unpinning and enhanced mobility. Conversely, cyclic electric field with fixed magnetic field training drives an opposite behavior, leading to magnetic hardening and stability. This contrasting response is attributed to distinct microstructural dynamics analogous to those found in ferromagnetic and ferroelectric systems. The bifunctional control mode allows the device to be dynamically tuned between a mobile configuration and a stable configuration, representing a critical advancement toward magnetoelectric spintronic devices.

3.1 Background and Motivation

The realization of next-generation, low-dissipation electronic devices hinges on the development of materials that allow for mutual control of magnetic and electric properties. Multiferroic and magnetoelectric (ME) materials, which host coupled magnetic and electric order parameters, provide the essential platform for investigating this fundamental coupling and exploiting it for novel device concepts [139,140].

The linear magnetoelectric (LME) effect, the focus of this work, is described by the coupling terms in the free energy expansion $F_{ME} = -\alpha_{ij}E_iH_j$. The cross coupling between the electric polarization (***P***) and the magnetic field (***H***), and between the magnetization (***M***) and the electric field (***E***), are represented by: $P_i(\boldsymbol{E},\boldsymbol{H}) = \alpha_{ij}H_j$, and $M_i(\boldsymbol{E},\boldsymbol{H}) = \frac{1}{\mu_0}\alpha_{ij}E_j$, where α_{ij} is the magnetoelectric tensor. This LME coupling is non-zero only in specific classes of materials that simultaneously break both time-reversal (T) and space-inversion (P) symmetry while preserving PT symmetry.

Among ME materials, the antiferromagnetic (AFM) insulator Chromium Oxide (Cr_2O_3) stands as the prototype system. It is a collinear AFM with a Néel temperature (T_N) near 307 K [201]. Its LME effect, characterized by the diagonal coefficient ($\alpha_{xx}, \alpha_{yy}, \alpha_{zz}$), is coupled directly to the AFM order parameter, the Néel vector, enabling the non-volatile switching of the Néel vector by simultaneous application of static ***E*** and ***H*** fields. This ability to use an electric field to write magnetic information makes it highly attractive for spintronics. However, due to the absence of spontaneous ***M*** and ***P***, it is challenging to

functionalize the linear magnetoelectric, making the development relatively slow compared to multiferroic materials [140,202].

Despite the absence of spontaneous $\boldsymbol{M}$ and $\boldsymbol{P}$, the ME coupling allows an applied electric field $\boldsymbol{E_B}$ to induce a magnetization $\boldsymbol{M}$, enabling Néel vector switching driven by a magnetic field $\boldsymbol{H}$, analogous to ferromagnetic (FM) behavior. Conversely, the presence of polarization $\boldsymbol{P}$ under a fixed magnetic field $\boldsymbol{H_B}$ allows Néel vector switching driven by an electric field $\boldsymbol{E}$, analogous to ferroelectric (FE) behavior [203]. To be more explicit, in a LME system, the dynamic change of the ME free energy $F = \alpha EH$ involve two terms:

$$\Delta F = \frac{\partial F}{\partial E}\Delta E + \frac{\partial F}{\partial H}\Delta H = \alpha H\Delta E + \alpha E\Delta H = \underbrace{P\Delta E}_{FE-like} + \underbrace{M\Delta H}_{FM-like}$$

The first term represents the FE-like mode, where the Néel vector couples to the electric polarization $\boldsymbol{P}$ and is switched by $\boldsymbol{E}$ when ΔH is zero (H is fixed), while the second term represents the FM-like mode, where the Néel vector couples to the magnetization $\boldsymbol{M}$ and is switched by $\boldsymbol{H}$ when ΔE is zero (E is fixed).

While both modes exploit linear magnetoelectric effect to drive Néel vector switching, these two modes are fundamentally different in dynamics. FM-like switching follows precessional, torque-driven magnetic dynamics described by Landau–Lifshitz–Gilbert (LLG) equation, while FE-like switching proceeds through overdamped polarization dynamics. Such a contrast may potentially lead to different microstructural evolution pathways and energy landscapes. However, to our knowledge, this possibility has not been systematically explored before.

In this work, we report precise, non-volatile switching of the Néel vector in Cr_2O_3 via the LME effect, with the two stable states robustly read out using the anomalous Hall resistance in an adjacent Pt detector layer. Crucially, we uncover a novel mode-dependent magnetoelectric effect that allows for the tuning of the Néel vector coercivity. FM-like mode cycling drives magnetic softening that enhances domain wall mobility for faster writing, while FE-like mode cycling induces magnetic hardening which stabilizes the magnetic state for long-term retention. Our results establish dual FM/FE mode control over the AFM magnetoelectric coupling, providing a viable pathway toward next-generation, energy-efficient spintronic memory devices.

3.2 Methods

The sample was fabricated from a 0.5 mm thick Cr_2O_3(0001) single crystal. The surface was polished using chemical mechanical polishing (CMP) to achieve an atomically flat finish, followed by standard solvent cleaning to remove residual surface contaminants. A 4 nm platinum (Pt) layer was subsequently deposited on the cleaned surface by sputtering. Device patterning was performed by defining a Hall cross structure with a channel width of 10 μm via electron beam lithography (EBL). The unpatterned Pt was removed using argon-based inductively coupled plasma reactive ion etching (ICP-RIE), yielding the final device geometry.

To investigate the ME effect, both E-field and H-field are needed. E-field is provided by a gate voltage applied across the Cr_2O_3 crystal, with the Pt Hall cross device

serving as the top electrode and a silver paint contact applied to the bottom surface acting as the bottom electrode. The sample was mounted in Quantum Design's Physical Property Measurement System (PPMS), allowing electrical transport measurements with an applied H-field up to 14 T and temperature down to 1.9K. Both the E-field and H-fields are applied either parallel or antiparallel to the c-axis, which is also the out-of-plane direction for Cr_2O_3 (0001) crystal.

3.3 Néel Vector Controlled by Magnetoelectric Annealing

For Cr_2O_3, the ME free energy term of the form $F(\boldsymbol{E},\boldsymbol{H}) = -\alpha_{ij}E_iH_j$ suggests a preferred AFM domain after cooling down through the Néel temperature T_N (~ 307 K) with a combination of electric fields ($\boldsymbol{E}$) and magnetic fields ($\boldsymbol{H}$), called magnetoelectric annealing [146,147,181,204]. Using this technique, we first verify the magnetoelectric coupling and the effectiveness of Pt layer for electrical detection of the Néel vector in our Cr_2O_3 crystal. **Figure 3.1** demonstrates deterministic control of the Néel vector orientation through traditional magnetoelectric annealing method. The measurement is carried out by averaging anomalous Hall resistance from two spinning current configurations as shown schematically in **Figure 3.1(a)**. As reported in previous literatures [150,179,180], this technique effectively eliminates mixing contributions from imperfect Hall cross geometry and potential planar Hall contributions, enabling clean detection of the uncompensated moment which couples to the Néel vector.

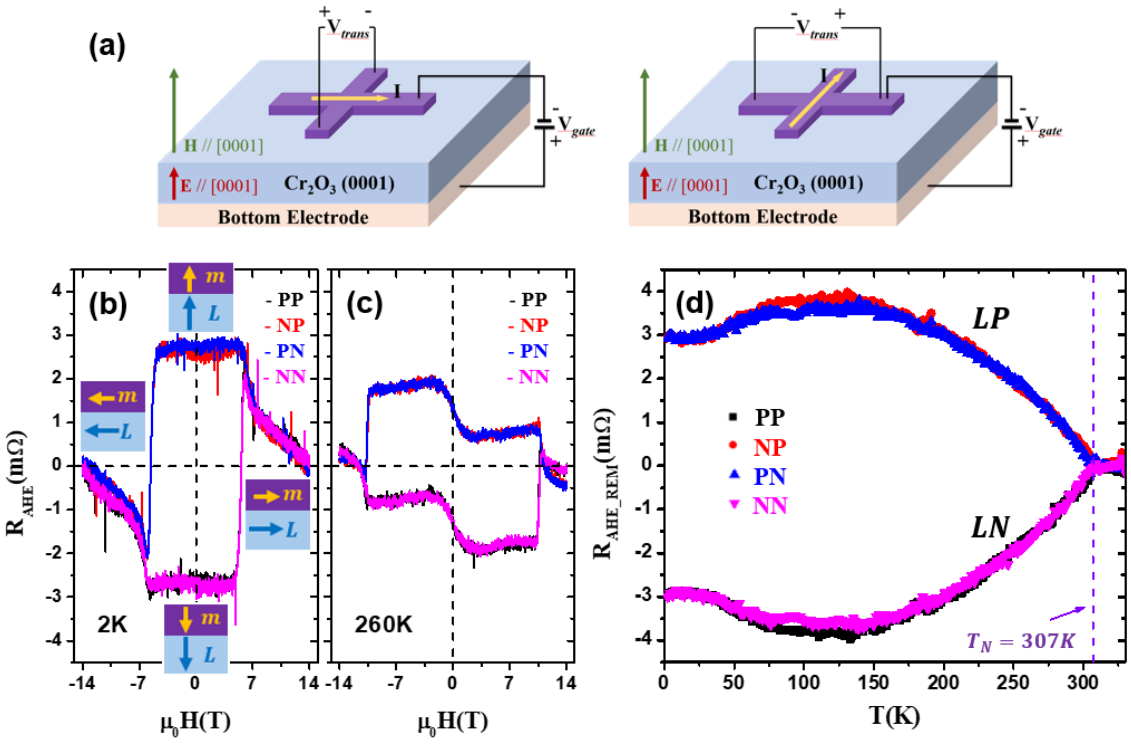


Figure 3.1 Magnetoelectric Annealing Experiments (a) Spinning current configurations. (b) R_{AHE} - H at 2K. (c) R_{AHE} - H at 260K. (d) Remanent R_{AHE} - T. Magnetic field sweeps between $\pm 14\ T$ are taken at zero electric fields. The four curves correspond to different measurements taken after four different magnetoelectric annealing process from 320K to the measured temperatures. No magnetic hysteresis is observed in each curve.

Magnetic field is applied in out-of-plane direction along the c-axis and swept between ± 14 T, and the spinning-current averaged R_{AHE} measured at 2K and 260K after removing a linear ordinary Hall background are plotted in **Figure 3.1(b)** and **Figure 3.1(c)** with respect to the applied magnetic field. Prior to the R_{AHE}-H measurements, the sample is prepared by cooling from 320 K, a temperature above its Néel temperature T_N (~ 307 K), to a temperature below T_N with a combination of $E_{cool} = \pm 1\ kVcm^{-1}$ and $\mu_0 H_{cool} = \pm 1\ T$, both applied along the c-axis direction. This annealing process stabilized a single AFM domain, and the type of AFM domain can be chosen based on the relative orientation

of the applied $\boldsymbol{E_{cool}}$ and $\boldsymbol{H_{cool}}$. Four crossed *EH* configurations are performed during the ME annealing process: positive $\boldsymbol{E_{cool}}$, positive $\boldsymbol{H_{cool}}$ (PP); negative $\boldsymbol{E_{cool}}$, positive $\boldsymbol{H_{cool}}$ (NP); positive $\boldsymbol{E_{cool}}$, negative $\boldsymbol{H_{cool}}$ (PN); negative $\boldsymbol{E_{cool}}$, negative $\boldsymbol{H_{cool}}$ (NN). When the temperature is reached, we remove the electric field and perform the mentioned spinning-current anomalous Hall measurements.

Clearly, at zero magnetic field, we observe a negative remanent $R_{AHE} \approx -3\ m\Omega$ at 2K (**Figure 3.1(b)**) after ME annealing in PP and NN configurations, in which magnetic field and electric field are parallel to each other. In contrast, after antiparallel PN and NP annealing, remanent R_{AHE} takes positive values $R_{AHE} \approx 3\ m\Omega$. This is consistent with expectations that parallel and antiparallel ME annealing will lead to opposite Néel vector domains. The observed remanent anomalous Hall resistance is attributed to proximity-induced moment in Pt, sensing the uncompensated moment from the top layer coupled to the Néel vector of Cr_2O_3 (see schematics). This assumption is further supported by taking the magnetic field sweep. At 2K, the detected R_{AHE} value remains field-invariant when the field is small. However, when the applied field exceeds the spin-flop transition field $\mu_0 H_{SF} \approx 6\ T$ of Cr_2O_3, R_{AHE} drops from a finite value to near zero due to vanishing out-of-plane moment when Néel vector reorients into the in-plane direction. The overall R_{AHE} curve shape includes both symmetric and antisymmetric contributions, which has been discussed in Chapter 2.

Similar trends are also observed at 260 K (**Figure 3.1(c)**), despite the lowered remanent $R_{AHE} \approx \pm 1.5 m\Omega$, the increased $\mu_0 H_{SF} \approx 10.6\ T$, and an emergent nonlinear low-field feature which is not influenced by different ME annealing configurations. This

nonlinear low-field anomalous Hall has been observed before in both Cr_2O_3/Pt and Cr_2O_3/Ta heterostructures [175,177,185,187] when the temperature is near and above T_N. The origin is still unclear, but likely intrinsic to Cr_2O_3/heavy-metal interface.

In **Figure 3.1(d)**, the remanence of anomalous Hall resistance, R_{AHE_REM}, is extracted and plotted as a function of temperature. Four curves are displayed corresponding to the PP, NP, PN, and NN configurations during ME annealing. Above $T_N \approx 307\ K$, no obvious anomalous Hall is observed. However, the four curves diverge into two branches with opposite R_{AHE_REM} values below 307 K, where antiparallel annealing configurations (NP, PN) take the positive branch and parallel configurations (PP, NN) take the negative branch. The curves peak at around 130K with a maximum value of around 4 mΩ, then decrease to approximately 3 mΩ at 2K. These experiments together provide clear evidence for the magnetoelectric coupling and electrical readout of the Cr_2O_3 Néel vector. For the convenience of later discussions, here we define the two stable Néel vector states as *LN* state and *LP* state. *LN* represents the Néel vector state with negative R_{AHE_REM} formed after PP and NN annealing. *LP* represents the Néel vector state with positive R_{AHE_REM} formed after NP and PN annealing.

3.4 Néel Vector Switching in FM-Like Mode

While ME annealing is the traditional and most effective method to manipulate the Cr_2O_3 Néel vector [146], isothermal switching without the need for temperature cycling is mandatory for practical, operational devices [147]. Achieving this is significantly more

challenging due to the inherent energy barrier (ΔF) separating the two stable Néel vector states as depicted schematically in **Figure 3.2(a)** (Reproduced from Ref. [205]).

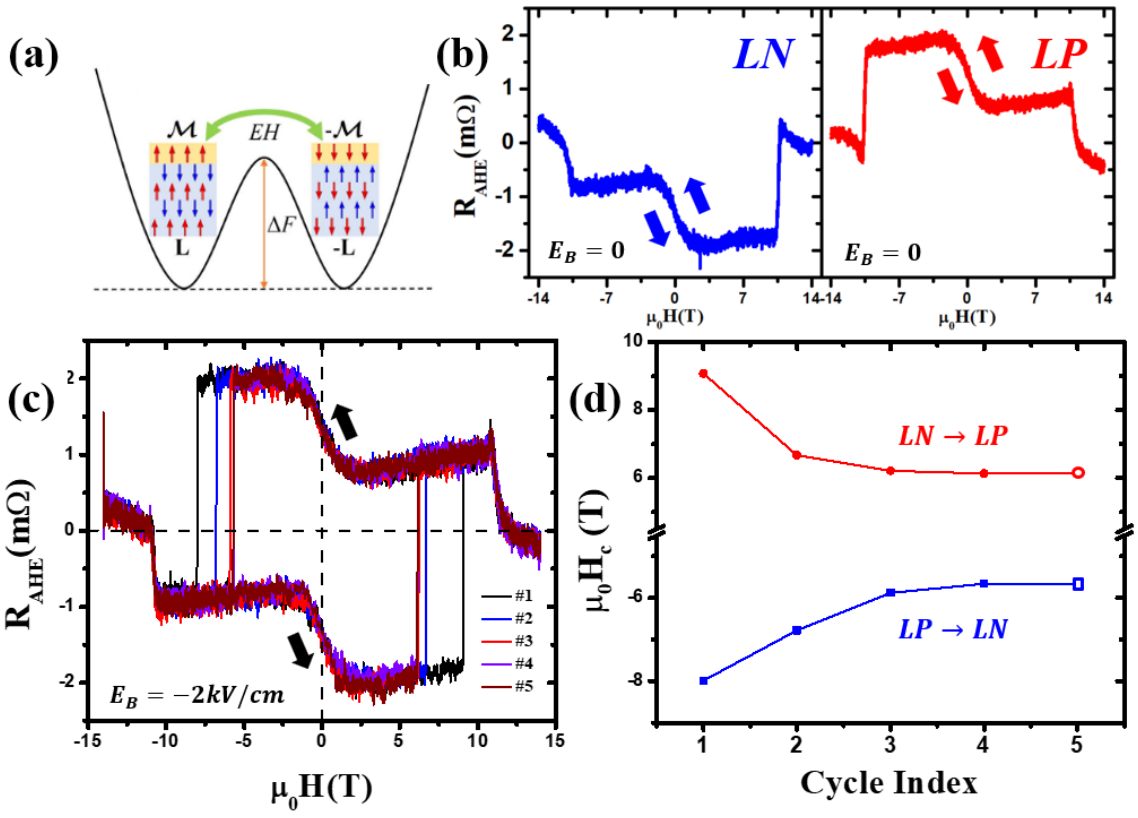


Figure 3.2 Isothermal Switching of the Néel Vector (a) Illustration of switching between two magnetic domain states by combined EH field reproduced from Ref. [205] (b) R_{AHE} during H-field sweep in the absence of E-field. LN and LP states are initiated by ME annealing. The arrows indicate field sweep directions. The same applies for (c). (c) R_{AHE} during multiple H-field sweep cycles with $E_B = -2\ kVcm^{-1}$. (d) H_c in different cycles, with the last cycle illustrated by open symbols.

To induce a switch isothermally, the applied ME free energy must overcome this intrinsic barrier, requiring the condition $\alpha EH > \Delta F$. In the idealized case of single-domain coherent switching (the entire magnetic volume flips uniformly), this barrier is determined

by the material's uniaxial anisotropy energy, K_u, making the required switching fields prohibitively high (see the discussion in **section 3.8.2**). However, in realistic materials, the switching mechanism is usually mediated by complex microstructures and dynamics of the system, such as domain wall nucleation and motion [206–208]. This dynamic, localized process effectively lowers the threshold energy required for switching, enabling the Néel vector to be flipped at achievable field strengths, albeit requiring careful control to ensure reliable, non-volatile operation.

After initializing a single-domain Néel state (LN or LP) via ME annealing, we perform H-field sweeps between $\pm 14\ T$ at $260\ K$ in the absence of an electric field. As shown in **Figure 3.2(b)**, no hysteresis is observed, and the R_{AHE_REM} (R_{AHE} at $H = 0$) remains unchanged throughout the cyclic H-field sweeps, indicating that the Néel vector is stable and no switching occurs. In contrast, in **Figure 3.2(c)**, when a constant bias electric field $E_B = -2kVcm^{-1}$ is applied to the Cr_2O_3 crystal, clear isothermal switching of the Néel vector between the LN and LP states emerges during the same $\pm 14\ T$ H-field sweep. This is evidenced by distinct hysteresis loops with split $R_{\mathrm{AHE_REM}}$ values of approximately $\pm 1.5\ m\Omega$ and well-defined coercive fields corresponding to the switching points. The switching behavior is attributed to a magnetization $\boldsymbol{M}$ induced by E_{B} in the Cr_2O_3 crystal as discussed in Section 3.1. The cyclic magnetic field directly acts on $\boldsymbol{M}$, generating magnetic torques that drive the Néel vector $\boldsymbol{L}$ through the magnetoelectric coupling.

Importantly, repeated H-field sweeps reveal a history-dependent training effect, characterized by the reduction and subsequent saturation of coercive field H_C upon repeated cycling. The evolution of H_C with cycle number is shown in **Figure 3.2(d)**. In

each cycle, two switching events occur: $LN \rightarrow LP$ at positive field, and $LP \rightarrow LN$ at negative field. Both transitions exhibit a similar decreasing and saturating trend upon repeated cycling. The H_C values from the final cycle (For here the 5th cycle) are taken as saturated values and are plotted as open symbols.

Training effects are a crucial manifestation of the underlying domain dynamics. The observed decreasing coercive fields over cycles reflects a relaxation of the magnetic microstructure toward a lower-energy configuration. Such behavior is commonly associated with irreversible rearrangements of AFM domains or domain walls during the initial switching cycles. The progressive stabilization of the switching fields suggests that internal defects, pinning sites, or interfacial strain may contribute to complex domain-wall dynamics in the Cr_2O_3 crystal. Consequently, the training effect provides insight into the microscopic energy landscape governing the motion of Néel vector $\boldsymbol{L}$ coupled with electric-field-induced $\boldsymbol{M}$.

We proceed to perform cyclic H-field sweep measurements at different E_B. At each E_B, multiple field sweeps are performed, exhibiting training effects that vary in magnitude but share a similar trend, characterized by a gradual reduction and eventual saturation of the coercive fields upon repeated magnetic cycling. The stabilized field sweep cycle at each E_B are plotted in **Figure 3.3(a)**. From the R_{AHE} loops at different E_B, it is first observed that the coercive field H_C decreases with increasing E_B. Secondly, when E_B changes sign, the polarity of the hysteresis also follows and changes sign. These observations are consistent with the LME effect. Larger E_B induced a larger magnetization $\boldsymbol{M}$, hence smaller $\boldsymbol{H_C}$ is

required to reverse $\boldsymbol{L}$ through Zeeman coupling $\boldsymbol{M} \cdot \boldsymbol{H}$. Conversely, reversing the sign of E_B inverts the ME coupling between $\boldsymbol{L}$ and $\boldsymbol{M}$, resulting in a reversal of hysteresis polarity.

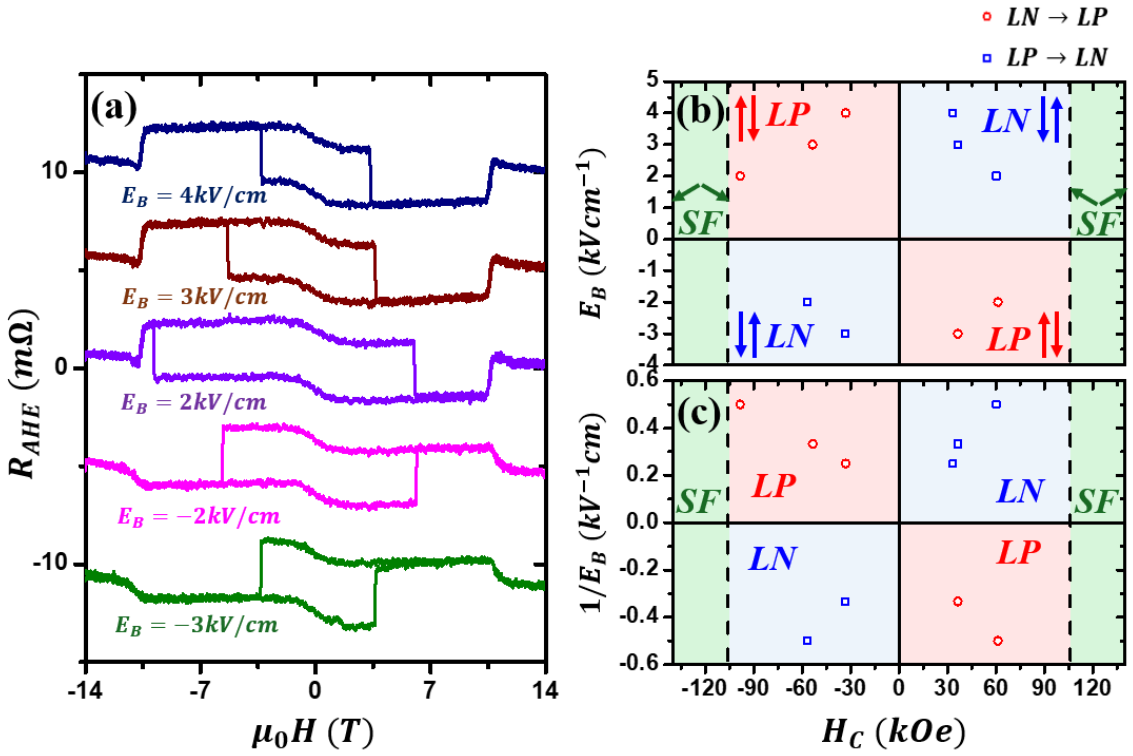


Figure 3.3 Magnetoelectric Switching for FM-Like Mode (a) H-field dependence of R_{AHE} at different E_B. The field thresholds are stabilized ones. (b) E_B vs. H_C. (c) E_B^{-1} vs. H_C.

Figure 3.3(b) shows an E-H plot at 260K where the energetically favored AFM domain states observed from previous ME annealing experiments are marked by different colors. *LN* domain (light blue) is preferred for PP and NN configurations, and *LP* domain (light red) is preferred for NP and PN configurations. However, when the magnetic field is larger than 10.6 T, the system prefers the spin-flop states (light green), where the antiparallel spins reoriented to the ab plane with slight canting toward the magnetic field

direction along the c-axis. It's worth noting that the spin-flop field remains invariant at different E fields in our experiments, contrasting a previous report [209]. The two stabilized $\boldsymbol{H_C}$ extracted from the hysteresis at each $\boldsymbol{E_B}$ (**Figure 3.3(a)**) are also plotted in **Figure 3.3(b)**. One $\boldsymbol{H_C}$ corresponds to the switching of $\boldsymbol{L}$ from *LN* to *LP* state, represented by the red open dots. Another $\boldsymbol{H_C}$ corresponding to the switching of L from *LP* to *LN* state are represented by the blue open dots. These switching behaviors aligned perfectly with the energetically preferred AFM phase diagram, highlighting consistency between ME annealing and isothermal ME switching experiments.

These critical E and H fields are expected to follow $|EH|_C = constant$ corresponding to the switching of the Cr_2O_3 AFM single domain [145,147]. To visualize this, we plot the E^{-1} to H as shown in **Figure 3.3(c)** to verify the linearity between E^{-1} and H, as indicated by $|EH|_C = constant$. Indeed, a clear linear relationship is observed between E^{-1} and H.

3.5 Néel Vector Switching in FE-like Mode

So far, we have demonstrated isothermal switching of the Néel vector $\boldsymbol{L}$ coupled to $\boldsymbol{M}$ driven by cyclic $\boldsymbol{H}$, which is analogous to the switching of FM materials, and training effect towards magnetic softening (lower H_C) is observed. Next, we demonstrate the switching of $\boldsymbol{L}$ in a FE-like mode, where an electric polarization, $\boldsymbol{P}$, is induced by a bias magnetic field H_B. As shown in **Figure 3.4(a)**, by dynamically cycling E fields between $\pm 4kVcm^{-1}$ with $H_B = 10T$, we observe hysteresis corresponding to the switching of the

Néel vector. (Notice that due to the existence of H_B, the original signal sits on an ordinary Hall background. Here we manual offset the center of the loop to zero to eliminate the background) Particularly, an increase of coercive electric field, E_C, upon training cycles before saturation after the 4th cycle is observed, contrasting the magnetic softening observed in FM-like mode. The E_C and remanent R_{AHE} across different cycles are further plotted in **Figure 3.4(b)** for clear view of the trend.

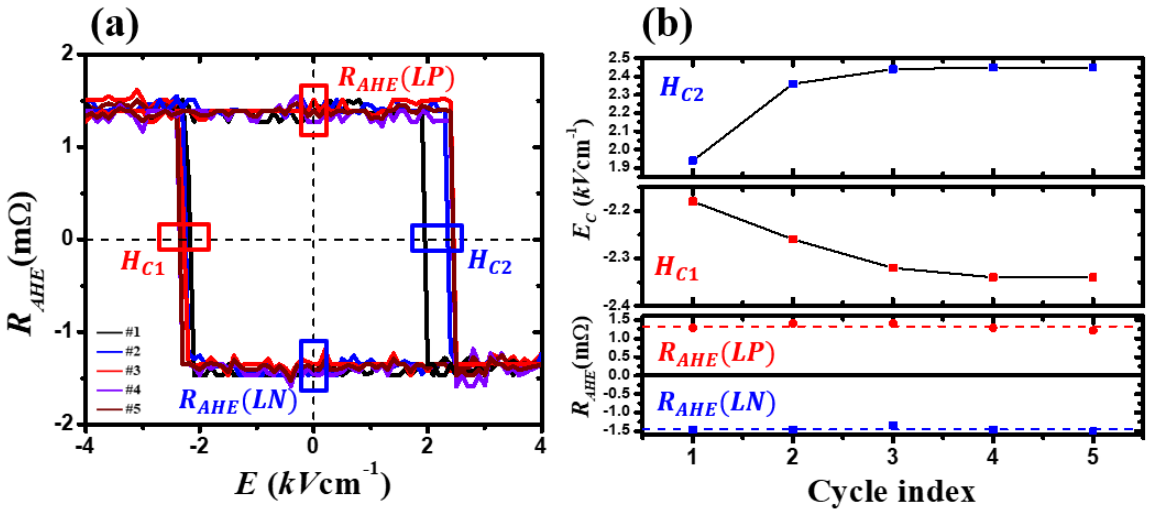


Figure 3.4 FE-Like Néel Vector Switching (a) R_{AHE} vs. E across 5 cycles. In each cycle, E starts from 4kV/cm (b) H_C and R_{AHE}.

The observed increase in coercive field E_C upon initial electric field cycling is a common but complex phenomenon in FE materials, often associated with mobile charged defects. Two primary effects, wake-up effect and fatigue, can both lead to electric hardening. Fatigue is characterized by the long-term accumulation of charged defects, such as oxygen vacancies, at domain walls and interfaces. [210–213] This accumulation creates localized pinning centers that severely hinder domain wall motion, leading to a progressive

loss of switchable polarization $\boldsymbol{P}$ thus enlarges E_C. Conversely, the wake-up effect describes an initial training period where the material's properties improve or stabilize. This effect is commonly associate with the rearrangement of existing mobile charge defects from a random, unstable initial state into more stable, ordered configurations, resulting in an increase and stabilization of the E_C and remanent polarization $\boldsymbol{P}$ [214–216].

Given that our Cr_2O_3 crystal exhibits a rapid increase in E_C that stabilizes within the first few cycles, this behavior is indicative of the wake-up effect. The initial electric field cycles provide the necessary energy to overcome the kinetic barrier, allowing a stable, optimized domain structure. This electric hardening process provides the foundation for the robust, retention-optimized state desired in non-volatile memory applications. Such a FE-like switching mode with stable R_{AHE} readout (lower panel in **Figure 3.4(b)**) from Pt layer also demonstrates the potential for voltage-controlled pure AFM spintronics using the Néel vector to encode information [149].

3.6 Mode-Dependent Dynamics and Energy of the Néel Vector

To investigate the mode-dependent dynamics under different switching modes, we performed measurements in a sequential manner. For the FM-like switching, where the magnetic field was cycled between $\pm 14T$ under a fixed electric bias, we first applied an electric field of $E = -2kVcm^{-1}$ and conducted five consecutive magnetic-field sweep cycles. The same procedure was then repeated at $E_B = -3kVcm^{-1}$, $E = 2kVcm^{-1}$, $E_B = 3kVcm^{-1}$, and $E_B = 4kVcm^{-1}$, each with 3-5 cycles depending on when the hysteresis

stabilized. Subsequently, for the FE-like switching, in which the electric field was cycled between $\pm 4 kV cm^{-1}$ under a constant magnetic field bias, we carried out 3-5 electric-field sweep cycles at successive magnetic fields of $H_B = 10T$, $H_B = 9T$, and $H_B = 8T$. This sequence allows direct comparison of the training effects and magnetoelectric threshold $|EH|_C$ arising from repeated magnetic versus electric switching under systematically varied bias conditions.

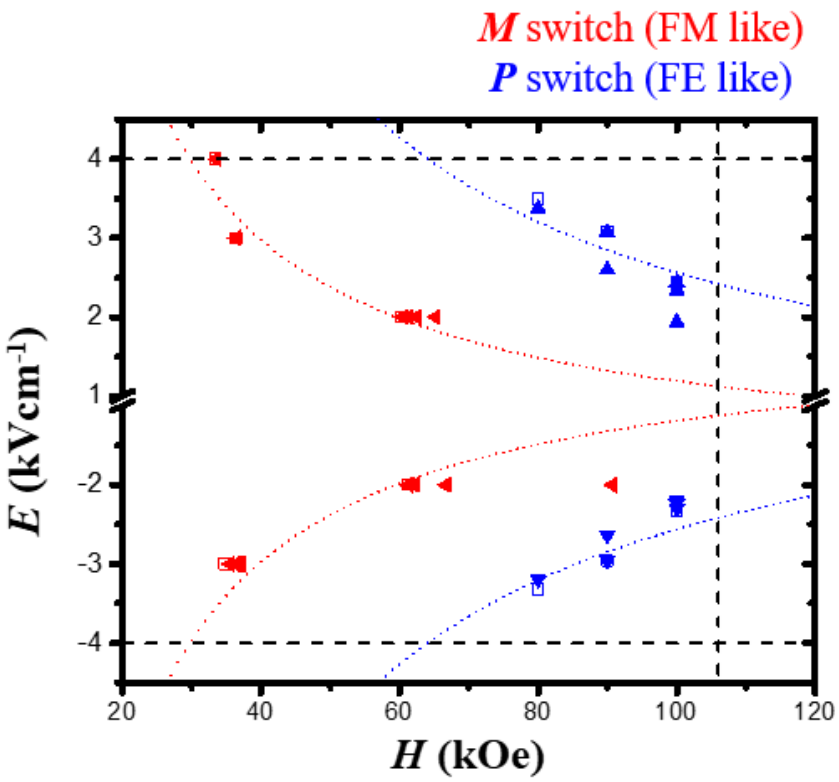


Figure 3.5 Dynamics and Energy of FM-Like and FE-Like Switching Solid and open symbols denote coercive fields extracted from initial training loops (closed) and final stabilized loop (open). Red dashed line corresponds to $|EH| = 119\ kVkOe/cm$ from fitting to the red open symbols. Blue dashed line corresponds to $|EH| = 256\ kVkOe/cm$ from fitting to the blue open symbols.

We present our results in **Figure 3.5**. Coercive fields extracted from all the loops taken in the sequence are plotted, denoted by either solid or open symbols: solid symbols correspond to all the initial and subsequent loops except for the final one, while open symbols represent the final loop measured at each E_B or H_B for the FM-like or FE-like switching mode. In the FM-like switching mode (red symbols), at the first three bias electric fields (E_B = −2, −3, and 2 kV/cm), we observe a clear training effect, characterized by an initial decrease in coercivity followed by stabilization after several loops. At higher bias fields (E_B = 3 and 4 kV/cm), however, the loops remain nearly identical from the first to the last cycle, exhibiting no obvious coercive training effect. This potentially indicates the system has already been dynamically tuned into a magnetically softer and more stable configuration, possibly due to equilibrium being reached in the interfacial exchange coupling or internal magnetic domain structure.

In contrast, the FE-like switching mode displays an increasing electric coercivity over successive loops before saturation. This trend suggests that the gradual rearrangement of mobile charge defects, such as oxygen vacancies, enhances domain pinning, leading to a wake-up effect commonly observed in FE materials. As a result, the system evolves toward a harder and more stabilized configuration upon cycling.

Consequently, **Figure 3.5** clearly shows that the FM-like and FE-like modes exhibit distinct $|EH|_C$ for switching. The red and blue dashed lines correspond to fits of the form $|EH| = C$ to the stabilized loops (open symbols) for the FM-like and FE-like modes using the stabilized (open symbols) loops. The FM-like mode yields a critical magnetoelectric threshold of approximately 119 kV·kOe/cm, whereas the FE-like mode requires a

substantially higher value of about 256 kV·kOe/cm. This contrast highlights the different energy barriers and microscopic mechanisms governing the two switching modes.

Importantly, these results further establish Cr_2O_3 as a prototypical magnetoelectric material whose linear and symmetry-defined ME coupling provides a clean platform for probing the dynamic interplay between magnetic and electric order parameters. Unlike multiferroic materials, where spontaneous magnetization and polarization coexist and often intertwine, Cr_2O_3 allows one to independently tune magnetic and electric degrees of freedom via the external fields *E* and *H*. This simplicity makes it possible to directly reveal the asymmetric microstructural dynamics manifested in the FM-like and FE-like switching modes.

3.7 Summary

In summary, we demonstrate deterministic magnetoelectric isothermal switching of the Néel vector in Cr_2O_3 single crystal, which can be effectively detected by anomalous Hall effect in the Pt layer exploiting Cr_2O_3(0001)/Pt heterostructures. This pure ME-based electrical writing and reading functionalities established a direct and efficient route for antiferromagnetic spintronics.

Crucially, the observation of distinct training behaviors and critical magnetoelectric thresholds suggests that the pathways of domain evolution and defect interaction differ fundamentally between these two modes. In the FM-like mode, the system relaxes toward a soft, equilibrated magnetic state. In contrast, the FE-like mode produces a hardening effect analogous to ferroelectric wake-up.

These findings imply that the ME switching process in Cr_2O_3 is not simply a reciprocal coupling between polarization and magnetization, but rather a history-dependent interplay between magnetic domain kinetics and electric-field-driven charge migration. The ability to access both regimes within the same material under controlled biasing conditions provides a rare opportunity to map the kinetic asymmetry between magnetic and electric order responses. This could have broader implications for designing ME-based memory devices, where the switching pathway can be selectively utilized to achieve either low-power, soft switching or high-stability, hard switching.

3.8 Discussions

In this section, I present additional discussions that are essential for a comprehensive understanding of this work.

3.8.1 Linear Magnetoelectric Effect in Cr_2O_3

Chromium(III) oxide (Cr_2O_3), commonly known as chromia, is a stable, hard, and chemically inert transition-metal oxide. It shares the corundum crystal structure (isostructural with α-Al_2O_3), which belongs to the trigonal crystal system with the centrosymmetric space group $R\bar{3}c$ and the point group $\bar{3}m$. This structure features a hexagonal close-packed array of oxygen ions with two-thirds of the octahedral interstitial sites occupied by ions.

Cr_2O_3 is a uniaxial antiferromagnetic insulator (bandgap > 3eV). Below its relatively high Néel temperature of $T_N \approx 307K$, Cr_2O_3 transitions from a paramagnet to an antiferromagnet. As shown in **Figure 3.6** (reproduced from Ref. [196]), The magnetic ordering is a collinear spin structure where the magnetic moments on the d^3 Cr^{3+} ions are aligned along the *c*-axis, equivalent to the hexagonal unit cell ⟨0001⟩ direction (**Figure 3.6(c)**). This specific antiferromagnetic configuration is known as easy-axis antiferromagnetism, allowing us to define 2 degenerate Néel vector domains: the up-down-up-down "in-pointing" domain as shown in **Figure 3.6(a)**, and the down-up-down-up **"out-pointing"** domain shown in **Figure 3.6(b)**.

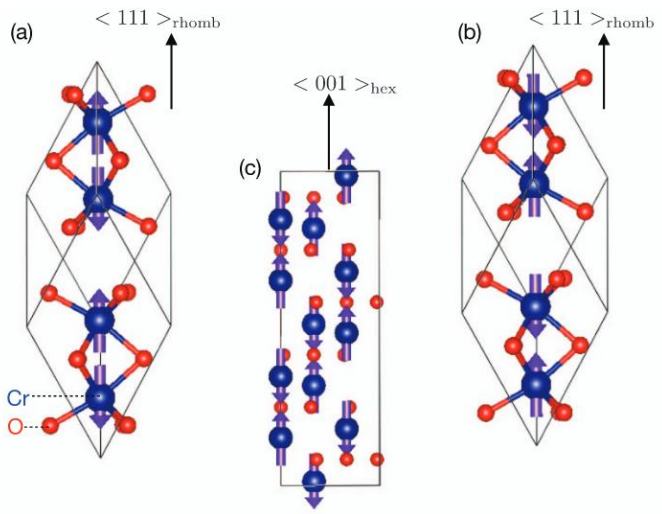


Figure 3.6 The Crystal and Spin Structure of Cr_2O_3 in the AFM Phase (a) "Out-pointing" Néel vector domain for the primitive rhombohedral unit cell (b) "In-pointing" Néel vector domain for the primitive rhombohedral unit cell (c) "In-pointing" Néel vector domain for the hexagonal unit cell. Reproduced from Ref. [196].

The combination of the crystallographic structure and the spin arrangement results in a unique magnetic symmetry that is crucial for its function. The magnetic order breaks both time-reversal symmetry (T) and the space-inversion symmetry (P) of the crystal lattice while preserving the combined PT symmetry, leading to the magnetic space group $R\bar{3}'c'$ and the corresponding magnetic point group $\bar{3}'m'$. This reduced symmetry is the key to the linear magnetoelectric (LME) effect. First predicted theoretically by Igor Dzyaloshinskii [141] and later confirmed experimentally [142,143], the LME effect in Cr_2O_3 is defined by ME tensor α_{ij} that only diagonal components ($i = j$) are allowed by its magnetic point group. The ME tensor

$$\alpha = \begin{pmatrix} \alpha_{\perp} & 0 & 0 \\ 0 & \alpha_{\perp} & 0 \\ 0 & 0 & \alpha_{\parallel} \end{pmatrix}$$

permits a term in the free energy of the form:

$$F(\boldsymbol{E}, \boldsymbol{H}) = -\alpha_{ij} E_i H_j$$

Here the ME tensor α is coupled to its spin structure, hence the Néel vector. For Cr_2O_3, if the Néel vector reverses its sign, such as reverses from the up-down-up-down domain (**Figure 3.6(a)**) to the down-up-down-up domain (**Figure 3.6(b)**), α_{ij} also reverses its sign. As a result, there is a preferred Néel vector domain orientation, determined by the combined electric field (***E***) and magnetic field (***H***). Another related property is the induction of magnetization ***M*** by an applied electric field ***E***, and conversely, the induction of electric polarization ***P*** by an applied magnetic field ***H***, following the equations:

$$P_i(\boldsymbol{E}, \boldsymbol{H}) = -\frac{\partial F}{\partial E_i} = \alpha_{ij} H_j$$

$$M_i(\boldsymbol{E}, \boldsymbol{H}) = -\frac{1}{\mu_0}\frac{\partial F}{\partial H_i} = \frac{1}{\mu_0}\alpha_{ji} E_i$$

Figure 3.7 shows the temperature dependence of $\alpha_{\parallel}$ and $\alpha_{\perp}$, extracted from one of the earliest experiment [143]. The transverse component $\alpha_{\perp}$ arises from the electric-field–induced canting of magnetic dipole moments away from the easy axis [217,218]. In contrast, the longitudinal component $\alpha_{\parallel}$ exhibits a peak in magnitude before decreasing and eventually changing sign at low temperatures. This behavior can be understood as a competition between contributions from spin fluctuations [219] and the orbital response [218].

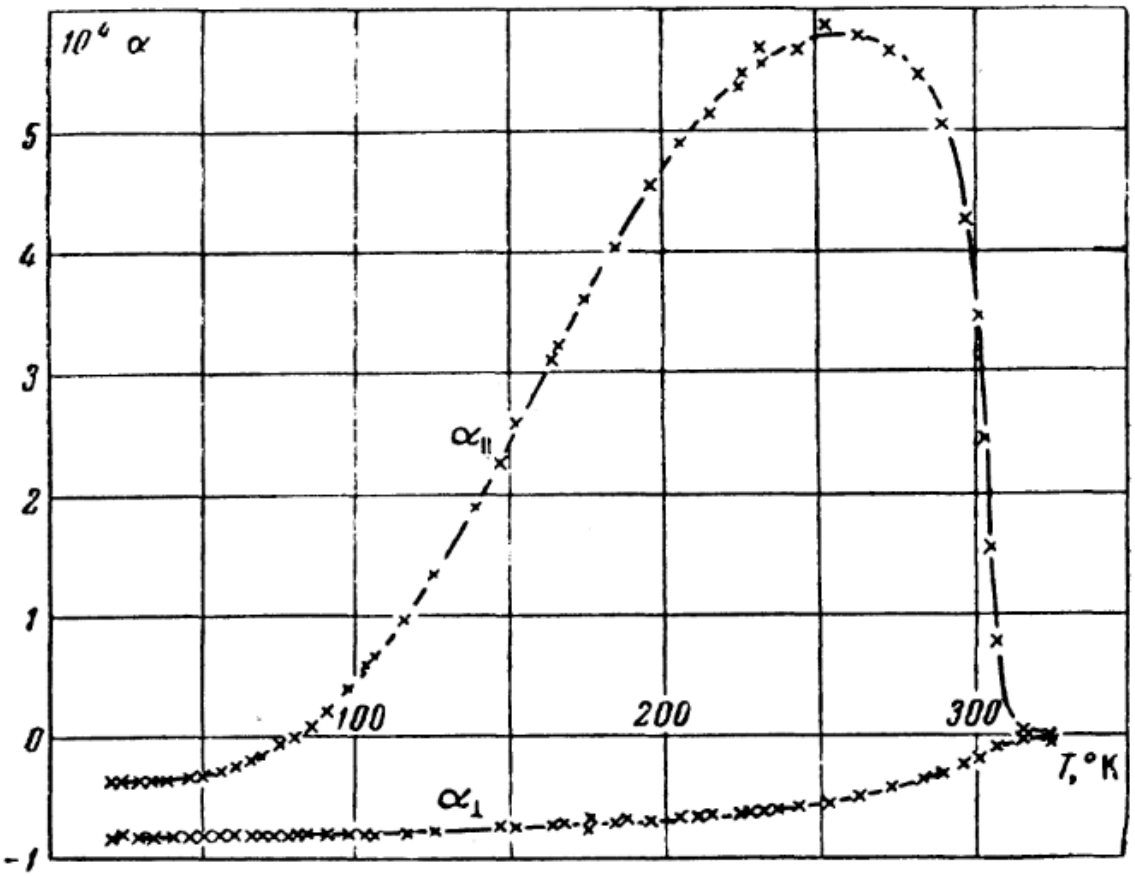


Figure 3.7 Temperature Dependence of the $\alpha_{\parallel}$ and $\alpha_{\perp}$ in Cr_2O_3 Reproduced from Ref. [143].

3.8.2 Estimation of Magnetoelectric Threshold for Coherent Switching

Here we provide a simple estimation of the critical magnetoelectric threshold $|EH|_c$ required to switch the Néel vector of Cr_2O_3, assuming a uniform coherent switching process. The lowest magnetoelectric energy term, αEH, must overcome the uniaxial anisotropy energy K_u, such that

$$\alpha EH \geq K_u$$

The reported values of the linear magnetoelectric coefficient α vary in literature. Here, we adopt a widely cited peak value of $\alpha_{ZZ} = 4.13\ ps/m$ [139]. The uniaxial magnetic anisotropy energy for Cr_2O_3 is $K_u = 2 \times 10^5\ ergs/cc$ [165], corresponding to $2 \times 10^4\ J/m^3$. Substituting these values yields

$$EH \geq \frac{K_u}{\alpha} \approx 4.84 \times 10^{15}\ (Jm^{-2}s^{-1}) \approx 6 \times 10^5\ (kVkOe/cm)$$

Even with an electric field as high as $E = 1000$ kV/cm, a magnetic field of $B = 60$ T would be required to reach this energy threshold. In our experimental configuration, the maximum electric field we can apply to the crystal is $E = 4$ kV/cm, in which case the corresponding magnetic field would need to exceed approximately 15000 T. This is far from realistically reachable. This simple estimation provides complementary evidence for the role of domain dynamics in magnetoelectric switching.

3.8.3 Comparison of Magnetoelectric Threshold Energy

In **Table 3-1**, we summarize the magnetoelectric threshold energy EH required to control the Néel vector orientation of Cr_2O_3 across different works we found. Studies on bulk crystals and thin films are separated. Generally, bulk crystals can be controlled with a lower energy $EH < 1000\ kVkOe/cm$, and thin films require higher energy. For Cr_2O_3 thin films, $1000\ kVkOe/cm < EH < 10000\ kVkOe/cm$ are commonly reported for magnetoelectric annealing, and $EH > 10000\ kVkOe/cm$ are commonly reported for isothermal switching. In addition, isothermal switching of Cr_2O_3 below 250K has not been reported before based on our searching results.

Table 3-1 Comparison of Magnetoelectric Threshold Energy (EH)

EH (kVkOe/cm)	Process	T (K)	Thickness	Ref
119, 256	**isothermal**	260K	0.5 mm	This work
15-190	**isothermal**	255K-300K	crystal	[145]
30	MEFC	298K	0.7 mm	[146]
40	**isothermal**	303K	0.6 mm	[147]
450, 1150	**isothermal**	300K, 290K	0.1 mm	[203]
10	MEFC	2K	0.5 mm	[150]
400	MEFC	200K	250nm	[192]
8000	MEFC	260K	150nm	[193]
4212-6714	MEFC	260K	150nm	[220]
9000	MEFC	280K	150nm	[221]
30000-40000	MEFC	280K	50nm	[222]
9600-12000	**isothermal**	275K	500nm	[148]
8000-24000	**isothermal**	253-278K	200nm	[194]
32000-52000	**isothermal**	285K	150nm	[223]
189000	**isothermal**	292K	200nm	[149]

Chapter 4 Temperature and Thickness Dependence of The Anomalous Hall Effect in Epitaxial Cr_2O_3 and Pt Heterostructures

We investigate the anomalous Hall effect in heterostructures of epitaxial Cr_2O_3(0001) thin films and Pt and reveal its coupling to the antiferromagnetic order of Cr_2O_3. We find that the sign of the proximity-induced anomalous Hall hysteresis is opposite between top and bottom interfaces in symmetric Pt/Cr_2O_3/Pt structures, consistent with the predicted opposite boundary magnetizations coupled to the Néel vector. By employing the Anomalous Hall effect as a sensitive probe, we uncover a thickness-dependent crossover of the Néel vector switching pathways. Different stacking sequence and temperature-dependent measurements provide insight into the underlying mechanisms driving the Néel vector switching. These findings demonstrate unprecedented control of Néel vector switching through Cr_2O_3 thickness, providing new design principles for antiferromagnetic spintronic devices.

4.1 Background and Motivation

Epitaxial thin films offer several key advantages over bulk crystals. From a practical standpoint, thin films are compatible with modern micro- and nano-fabrication techniques, enabling integration into device architectures. Their thickness, strain, and interfacial environment can be precisely engineered for tunable magnetoelectric and spin-transport properties. From a fundamental perspective, thin films provide a platform to explore how reduced dimensionality and interfacial effects modify the physical properties and Néel vector dynamics. These effects can lead to magnetic behaviors not observed in bulk Cr_2O_3, offering deeper insight into the mechanisms that govern spin order in magnetoelectric antiferromagnets.

Particularly, the anomalous Hall effect in Cr_2O_3/Pt thin film stacks has been a focus of research in recent years [174,175,185,187,224,225]. Several studies have reported hysteresis loops during magnetic-field sweeps in Cr_2O_3/Pt thin film systems [174,185,224], in stark contrast to the behavior of bulk Cr_2O_3, which exhibit field-invariant surface moment below spin-flop transition [150]. Recently, Ujimoto et al. reported imaging of surface Cr moments in Pt/Cr_2O_3/Pt using X-ray magnetic circular dichroism (XMCD) [174], providing evidence that links the reversal of AFM order to the observed AHE hysteresis. However, the microscopic mechanisms governing the AFM order reversal, and how they might be controlled for functional AFM spintronic applications, remain elusive.

In this chapter, we report the observation and systematic investigation of the AHE hysteresis in heterostructures composed of epitaxial Cr_2O_3(0001) thin films and Pt. High-

quality Cr_2O_3 thin films are epitaxially grown on $Al_2O_3(0001)$ or $Al_2O_3(0001)/Pt(111)$ substrates using pulsed laser deposition (PLD) and subsequently fabricated into Hall bar devices. Transport measurements reveal that the AHE hysteresis polarity is opposite for the top and bottom Pt layer in $Pt/Cr_2O_3/Pt$ structures, consistent with the expected reversal of boundary magnetization at the top and bottom Cr_2O_3 interfaces. This finding confirms that the observed AHE hysteresis is intrinsically coupled to the AFM order reversal of the Cr_2O_3 thin film.

Crucially, we reveal a pronounced dependence of the anomalous Hall effect hysteresis on both the Cr_2O_3 layer thickness and temperature. These results demonstrate an unprecedented crossover in the Néel vector switching pathway, offering new insights into the underlying switching mechanisms and presenting a promising route for engineering next-generation antiferromagnetic spintronic devices.

4.2 Epitaxial Growth of $Cr_2O_3(0001)$ Thin Films

To investigate the temperature and thickness dependence of the anomalous Hall effect in different stacking configurations, including $Al_2O_3/Cr_2O_3/Pt$, $Al_2O_3/Pt/Cr_2O_3$, and $Al_2O_3/Pt/Cr_2O_3/Pt$, we adopted a controlled growth approach. Thin epitaxial Cr_2O_3 layers were deposited using pulsed laser deposition (PLD) on atomically flat substrates to ensure smooth, high-quality surfaces. This technique enables precise control over film thickness, allowing exploration of the structural and magnetic properties with varying thickness. We systematically employ different parameters to grow the Cr_2O_3 films, including target

composition (Cr_2O_3 or Cr), growth atmosphere (O_2 or O_3), chamber pressure (2–2.2 mTorr), substrate temperature (400–530 °C), laser energy (150–300 mJ), repetition rate (1–4 Hz), and post-deposition annealing parameters.

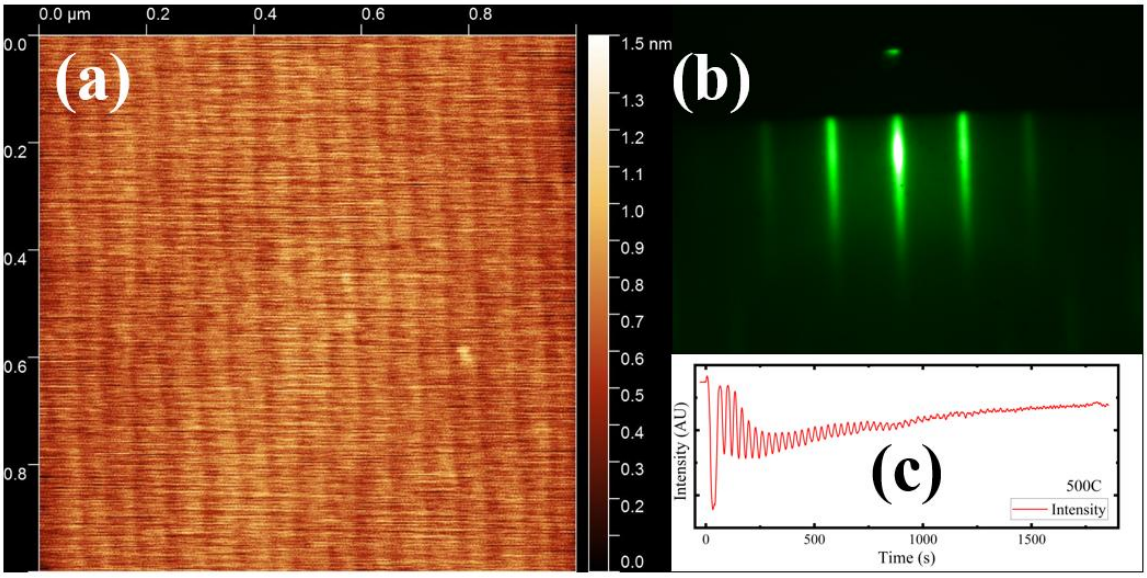


Figure 4.1 Structural Characterization of Al_2O_3(0001)/Cr_2O_3 (a) Atomic force microscopy image of a representative Al_2O_3(0001)/Cr_2O_3 sample. (b) RHEED pattern. (c) RHEED intensity during a 30 mins growth.

For the Al_2O_3/Cr_2O_3/Pt stacking, Cr_2O_3 was epitaxially grown on Al_2O_3(0001). **Figure 4.1(a)** shows the atomic force microscopy image of a representative sample over a 1 µm × 1 µm area, revealing well-defined atomic terraces with a root-mean-square (RMS) roughness of 0.15 nm. The atomic force microscopy image along with the streaky reflection high-energy electron diffraction (RHEED) pattern shown in **Figure 4.1(b)** confirms the high crystallinity and smooth surface morphology. **Figure 4.1(c)** presents the RHEED intensity oscillations recorded during 30 minutes of growth. The clear periodic oscillations

not only indicate layer-by-layer epitaxial growth but also provide a reliable measure for determining film thickness.

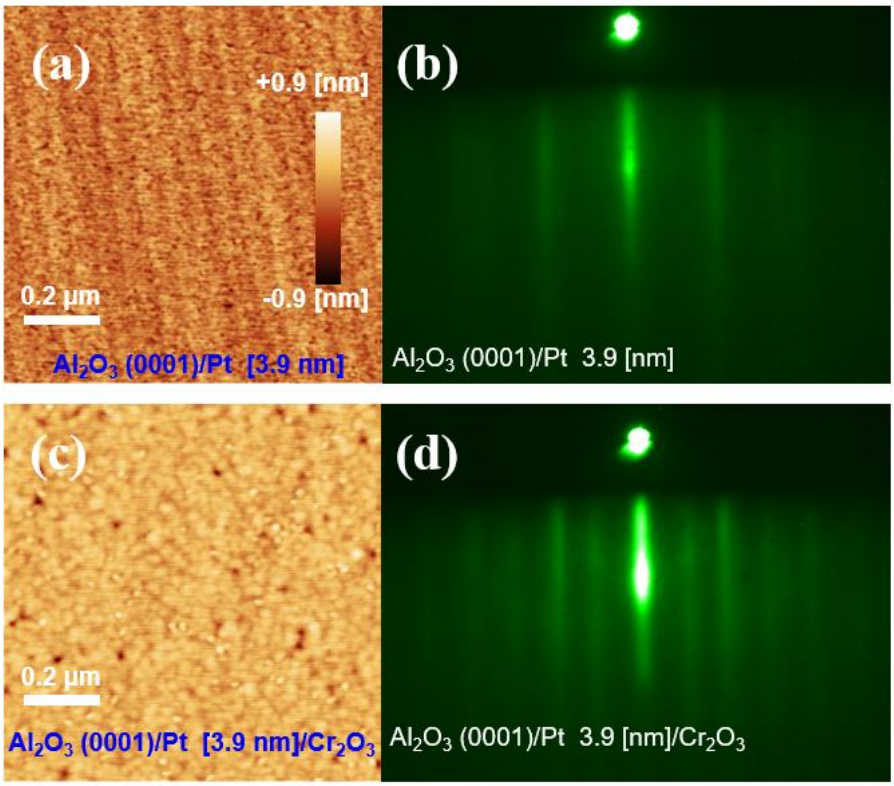


Figure 4.2 Structural Characterization of Al_2O_3(0001)/Pt/Cr_2O_3 (a) Atomic force microscopy image and (b) RHEED pattern of Al_2O_3(0001)/Pt[3.9nm]. (c) Atomic force microscopy image and (d) RHEED pattern of Al_2O_3(0001) /Pt[3.9nm]/Cr_2O_3.

For the Al_2O_3/Pt/Cr_2O_3 and Al_2O_3/Pt/Cr_2O_3/Pt stacking configurations, a thin Pt layer (typically 4 nm thick) was first deposited onto the Al_2O_3(0001) substrate using magnetron sputtering and subsequently annealed at 700 °C. This process produced a smooth surface with atomic terraces and a streaky RHEED pattern, as shown in **Figures 4.2(a)** and **Figure 4.2(b)**, and an RMS roughness of approximately 0.19 nm. The Cr_2O_3

thin film was then grown on this Pt surface by PLD. The corresponding AFM image and RHEED pattern are presented in **Figures 4.2(c)** and **Figure 4.2(d)**. Although the Cr_2O_3 surface remains relatively smooth with an RMS roughness of approximately 0.29 nm, the absence of clear terraces and the emergence of pinholes indicate a lower epitaxial quality compared with Cr_2O_3 directly grown on Al_2O_3 substrates. This reduced interface quality may contribute to the lower magnitude of the observed AHE, as will be discussed later. The subsequent device fabrication process is described in **Section 4.8.2**.

4.3 AHE in Cr_2O_3/Pt (Top Detector)

We begin with the observation of AHE hysteresis and its temperature dependence in a Cr_2O_3(0001)/Pt device. The Cr_2O_3 layer has a thickness of approximately 11 nm.

Figure 4.3(a) presents the anomalous Hall resistance R_{AHE} of the top Pt Hall cross device, measured at 150 K with magnetic field applied along the c-axis. The main panel displays the R_{AHE} data, which is obtained by subtracting a linear background from the original R_{yx} data (shown in the inset of **Figure 4.3(a)**). This linear background is attributed to the ordinary Hall effect (OHE), a transverse potential difference that scales linearly with the perpendicular magnetic field due to the Lorentz force. In all the samples across all temperatures in this present study, we found the OHE slopes are negative, which reflects that electrons are the primary charge carriers in Pt. The top right schematic illustrates the device stacking order.

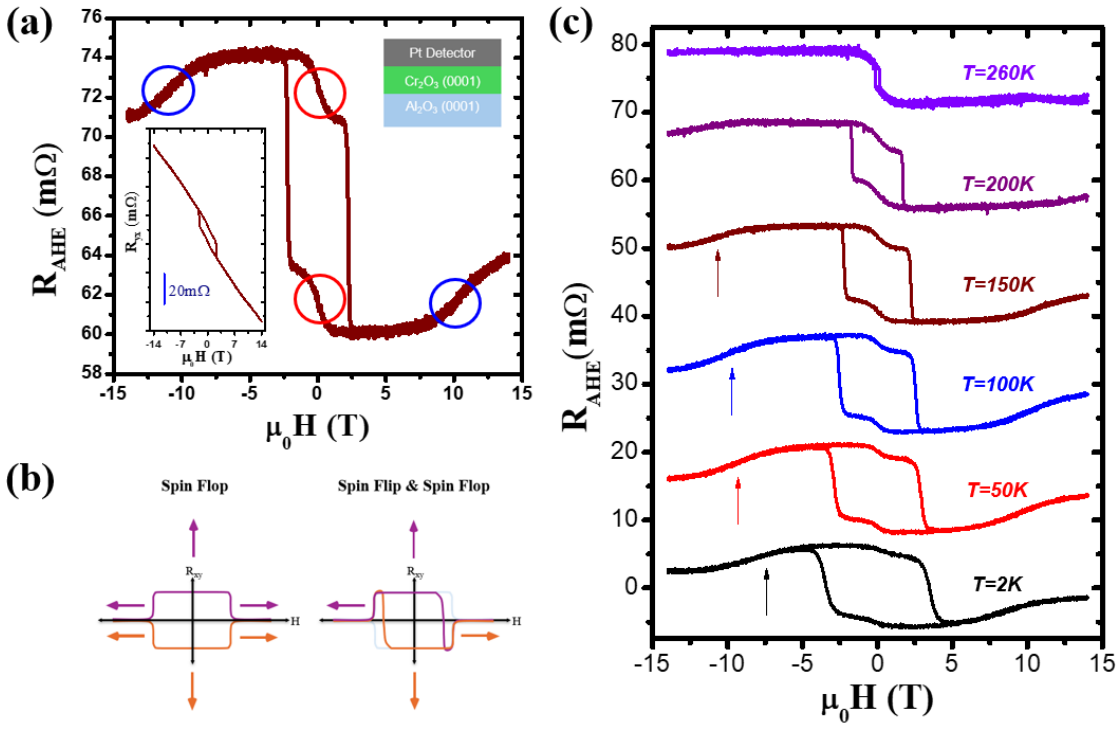


Figure 4.3 Anomalous Hall Effect of Cr_2O_3/Pt (a) R_{AHE} of 11 nm thick Cr_2O_3/Pt measured at 150K. Magnetic field is applied along the c-axis. Red and blue circles highlight the nonlinear AHE regions at low fields and high fields. The inset is the original R_{yx} data with linear background. The top-right schematic illustrates device stacking order. (b) Illustrations of spin-flop transitions and spin-flip transitions. The arrows indicate the Néel vector direction. (c) R_{AHE} at different temperatures. Arrows indicate the position of spin-flop transitions.

The resulting R_{AHE} loop exhibits a clear hysteresis with distinct coercive fields and two well-defined AHE values at zero magnetic field. The sharp switching between the two states is characteristic of a material with perpendicular magnetic anisotropy (PMA), consistent with the Cr_2O_3(0001) thin film. Beyond the characteristic hysteresis, additional nonlinear features emerge in both the low-field (red circles) and high-field (blue circles) regions. The nonlinear anomaly at low-field region is also observed in Cr_2O_3 crystal, and a related discussion is provided in **Section 2.6.9**.

Assuming the AHE hysteresis is the result of magnetic-field-induced Néel vector switching (spin flip), detected via a coupled interfacial moment in the Pt layer as suggested by other studies [174,185], then the high-field nonlinear AHE likely characterized the spin-flop transition, as schematically illustrated in **Figure 4.3(b)**. Therefore, the complete R_{AHE} loop can be interpreted as the combination of spin-flip transitions between two Néel vector states occurring near $\pm 2.5\ T$ and spin-flop transitions occurring near $\pm 10\ T$.

Figure 4.3(c) shows the R_{AHE} loops at different temperatures, where the arrows indicate the positions of the spin-flop transitions. The positions of spin-flop transitions are determined by the local maximum of the derivatives (see **section 4.8.3**). Qualitatively, the coercive field H_c for the Néel vector switching decreases with increasing temperatures, while the spin-flop transition field H_{SF} increases with temperature. Importantly, H_c and H_{SF} appear independent of each other. The observed decrease in H_c is analogous to typical ferromagnetic systems, where higher thermal agitation lowers the magnetic anisotropy energy, suppressing the coercive field. This observation suggests the possible existence of net magnetization in the 11 nm thick Cr_2O_3/Pt sample, which is large enough to drive the Néel vector switching by Zeeman coupling with the applied magnetic field.

4.4 AHE in Pt/Cr_2O_3/Pt (Both Top and Bottom Detectors)

Our previous discussions assume that the AHE hysteresis arises from Néel vector switching induced solely by magnetic field. To examine this assumption, we recall that in magnetoelectric AFMs, the top and bottom surfaces possess boundary magnetizations

pointing in opposite directions, as required by the magnetic point group symmetry [147,191,205,226]. Therefore, the top Pt layer and bottom Pt layer should be magnetized oppositely, leading to AHE hysteresis loops with reversed polarity when the Néel vector is switched by the magnetic field.

Figure 4.4 presents the R_{AHE} measured at 200 K from both the top and bottom detectors in a Pt/Cr_2O_3/Pt device with a Cr_2O_3 layer thickness of 23 nm, with the inset showing an optical image of the device layout. Both loops are manually centered at $R_{\mathrm{AHE}} = 0$ for clearer comparison. Schematics illustrate the corresponding stacking order of the measured devices.

Apparently, the top and bottom detectors exhibit AHE loops of opposite polarity while sharing nearly identical coercive fields. For clarity in later discussions, we define the polarity of the R_{AHE} loop in the top detector as negative (clockwise) and that in the bottom detector as positive (counterclockwise). This result demonstrates that the top and bottom Pt layers sense opposite interfacial magnetizations, providing strong evidence that the R_{AHE} signal is directly coupled to the Néel vector orientation. Consequently, this confirms that the Néel vector in Cr_2O_3 thin films can be switched solely by applying a magnetic field.

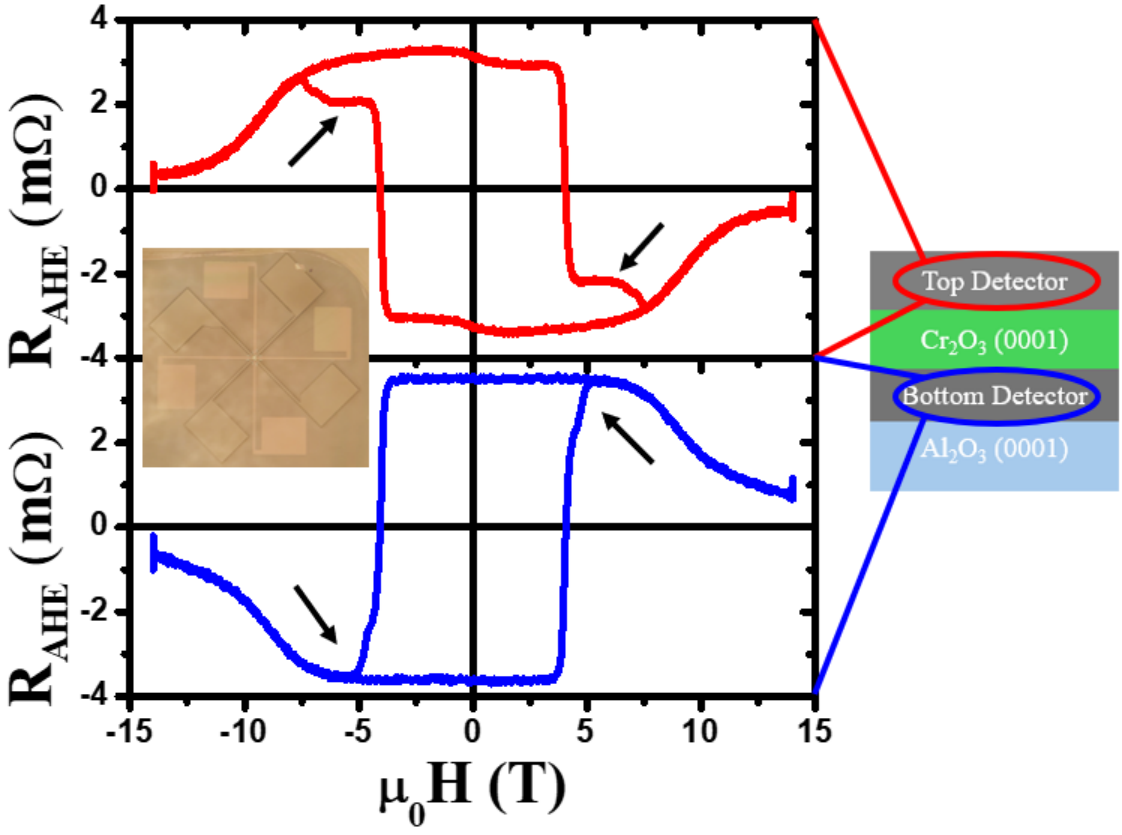


Figure 4.4 Anomalous Hall Effect in Pt/Cr_2O_3/Pt R_{AHE} measured at $T = 200K$ for top detector (top panel) and bottom detector (bottom panel) of the sandwiched Pt/Cr_2O_3/Pt device (23 nm). Device layout is shown in the inset. Schematic illustrates the corresponding stacking order of the device.

Additional anomaly in the switching is observed in R_{AHE} curves as indicated by the arrows. The switching anomaly can be understood within a multidomain framework. During the Néel vector reversal, the Cr_2O_3 layer may not switch uniformly but instead evolves through the nucleation and growth of multiple domains. For example, similar switching anomaly has been reported in patterned NiFeCo submicron arrays, where trapped magnetization vortices and domain-wall motion lead to complex magnetization reversal processes [208].

Beyond the general domain picture, another plausible explanation involves the role of interfacial Dzyaloshinskii–Moriya interactions (DMIs). Previous studies have shown that the Pt/Cr_2O_3 interface can break inversion symmetry and generate interfacial DMI, which in turn can influence both transport phenomena and surface spin structures [184,187]. In the Pt/Cr_2O_3/Pt sandwiched structure, the two interfaces may induce DMIs of opposite chirality, leading to an asymmetric spin texture or partial canting across the film thickness. Similar effects have been reported in perpendicularly magnetized Pt/Co/Pt and Pt/Co/Ir/Pt thin films, where the DMI strength and sign can be tailored by modifying the top and bottom interfaces [227]. Such competing interfacial DMIs in the Cr_2O_3-based heterostructure could stabilize noncollinear or twisted spin configurations, resulting in the observed switching anomaly. Considering that this anomaly appears exclusively in the Pt/Cr_2O_3/Pt sandwiched device, this mechanism presents an intriguing possibility worthy of further investigation.

4.5 Thickness and Temperature Dependence of AHE

Magnetic-field-induced AFM order reversal is peculiar and worth exploring. An intriguing question is whether this phenomenon is intrinsic to Cr_2O_3 thin films or Cr_2O_3/Pt stacks due to thickness reduction, or it is due to extrinsic factors such as inhomogeneity or defects. To answer this question, we proceed to examine the temperature dependence and thickness dependence of the AHE in Cr_2O_3 thin film samples, including both Cr_2O_3/Pt top detector and Pt/Cr_2O_3 bottom detector samples.

Figure 4.5(a-c) presents the R_{AHE} loops of Cr_2O_3/Pt top detector samples with different thickness, including the one discussed in Section 4.3. The Cr_2O_3 layer thicknesses are 11 nm, 30 nm, and 45 nm. Interestingly, we observed markedly different AHE behaviors between these samples.

The most striking observation is that the 11 nm and 45 nm samples exhibit opposite polarities in their R_{AHE} loops. In the 11 nm sample, the R_{AHE} loops show negative polarity across all measured temperatures, from 2 K up to above 260 K. In contrast, the 45 nm sample consistently exhibits positive polarity from 2 K to 300 K. Furthermore, the coercive field behavior differs significantly between the two. For the 11 nm sample, the coercive fields are relatively small (< 5 T) and decrease monotonically with increasing temperature. Conversely, in the 45 nm sample, the coercive fields are much larger (> 5 T) and increase with temperature up to above 250 K.

These contrasting trends suggest that distinct mechanisms may govern the Néel vector switching in the thin and thick Cr_2O_3 layers, driving the Néel vector in the opposite direction. Alternatively, the observed polarity reversal may indicate that the interfacial surface moments in these two samples have opposite signs.

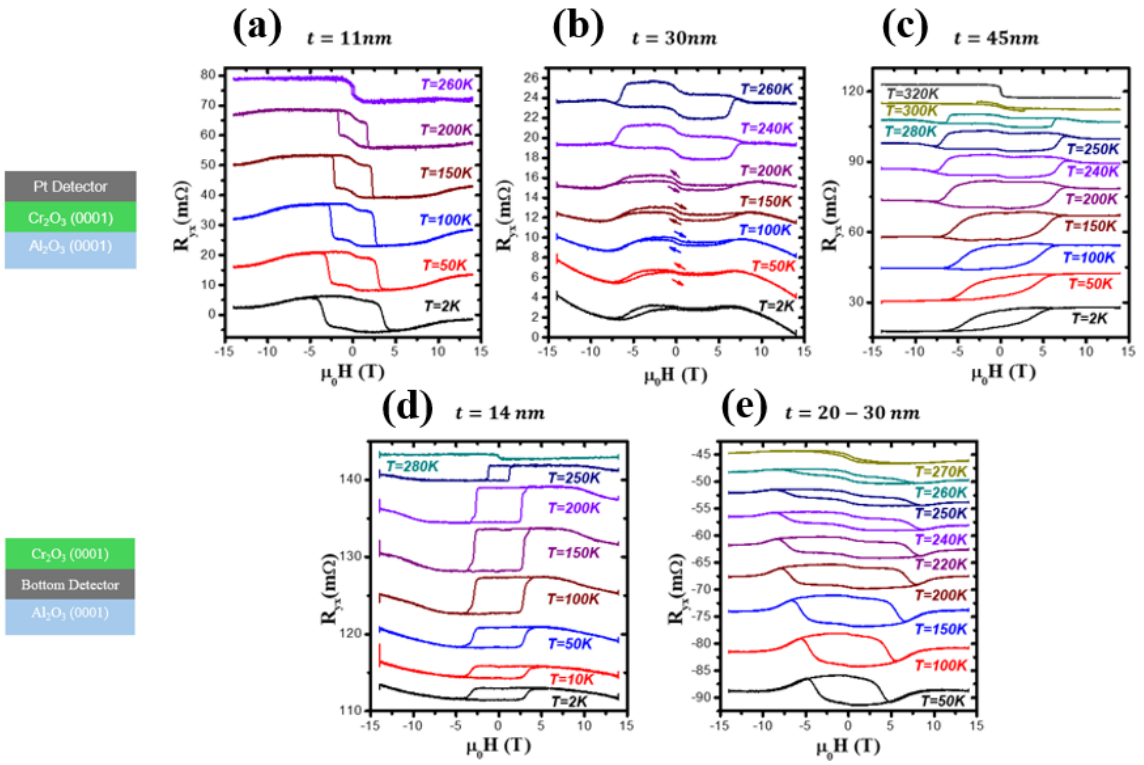


Figure 4.5 R_{AHE} Loops for Cr_2O_3 Samples with Different Layer Thickness (a-c) R_{AHE} loops of Cr_2O_3/Pt samples with (a) 11 nm, (b) 30 nm, and (c) 45 nm thickness. The arrows indicate the loop directions. (d,e) R_{AHE} loops of Pt/Cr_2O_3 samples. One with a Cr_2O_3 layer thickness of (d) 14 nm. Another one is estimated to be (e) 20-30 nm thick.

A sample with an intermediate thickness of 30 nm between the previous two cases provides a clear distinction between the two possible explanations. Notably, the R_{AHE} magnitude becomes significantly smaller below 200 K compared to its high-temperature values. This behavior is unlikely to originate from the temperature dependence of interfacial moments. Instead, it suggests the presence of minor loops associated with multidomain formation, likely arising from competing mechanisms that drive the Néel vector in opposite directions. More importantly, the loops exhibit two polarity reversals, one between 50 K and 100 K, and another between 150 K and 200 K. These features

provide supporting evidence for the coexistence of competing switching mechanisms, rather than simply opposite interfacial moment signs, as the origin of the reversed polarity observed in the thin and thick samples.

Figure 4.5(d,e) presents the R_{AHE} loops of two Pt/Cr_2O_3 bottom detector samples. The thinner sample has a Cr_2O_3 layer thickness of 11 nm, while the thicker one is estimated to be 20-30 nm. For the bottom detector samples, we observe trends similar to those in the top detector samples. In particular, the 14 nm bottom detector sample exhibit R_{AHE} loops polarities opposite to those of the 11 nm top detector sample, which we attribute to the opposite interfacial moments at the top and bottom interfaces, as discussed in **Section 4.4**. When the Cr_2O_3 layer thickness increases, the R_{AHE} loops reverse their polarity. The coercive field H_c of the 20-30 nm thick bottom detector sample also shows a similar temperature dependence to that of the 43 nm top detector sample, first increasing with temperature up to 250 K and then decreasing and vanishing at higher temperatures. The resemblance between these two samples suggests that a common underlying mechanism governs the behavior.

Notably, the sign reversal of R_{AHE} occurs at different thicknesses for the top and bottom Pt samples. This indicates that the Cr_2O_3 layer thickness alone does not determine the observed polarity reversal. We tentatively attribute this discrepancy to differences in interfacial quality between Cr_2O_3/Pt and Pt/Cr_2O_3 interfaces. As discussed in **Section 4.2**, Cr_2O_3 grown on Al_2O_3 and on Al_2O_3/Pt shows distinct structural characteristics. This further underscores the importance of high-precision, well-controlled epitaxial growth in achieving reproducible properties for the study of complex interfacial effects.

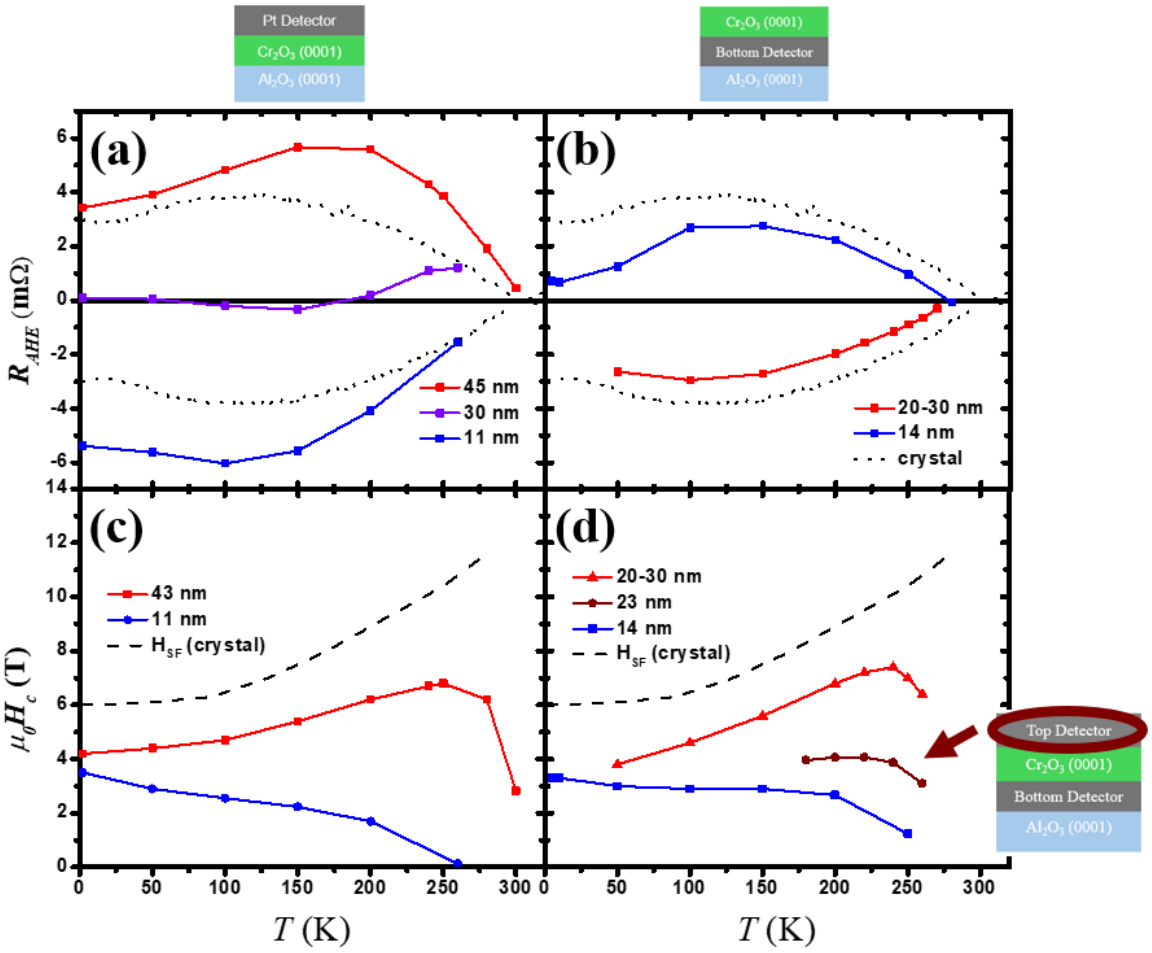


Figure 4.6 Temperature and Thickness Dependence of R_{AHE} and H_c (a) R_{AHE} from Cr_2O_3/Pt top detector samples extracted from Figure 4.5. The dotted lines are from Cr_2O_3 single crystal device for reference. (b) Coercive fields extracted from four different samples, including both Cr_2O_3/Pt and Pt/Cr_2O_3/Pt. Dashed line is crystal H_{SF} for reference.

Figure 4.6 presents the temperature dependence of R_{AHE} and H_c extracted from the samples shown in Figure 4.5. For positive polarity, we take positive R_{AHE} values. For negative polarity, we take negative R_{AHE} values. Dotted lines are the positive and negative R_{AHE} derived from the Cr_2O_3 single crystal in Chapter 3, which we plot here as a reference.

For top detector samples in **Figure 4.6(a)** and bottom detector samples in **Figure 4.6(b)**, the temperature-dependent R_{AHE} curves resemble that of the single crystal, albeit with slightly different onset temperatures. These temperatures correspond to their respective Néel temperatures, which vary with film thickness. Notably, top detector samples generally exhibit R_{AHE} magnitudes larger than those of the single crystal, while bottom detector samples generally exhibit smaller R_{AHE} magnitudes. This possibly reflects the interface quality in the different kinds of samples. The overall curves shape are within reasonable sample-to-sample variations and are consistent with previous reports [175,178,178,180].

Importantly, the 11 nm and 45 nm films exhibit R_{AHE} of comparable magnitude but opposite sign, implying distinct underlying mechanisms that drive the Néel vector in opposite directions under an applied magnetic field. This is the same for the 14 nm and 20-30 nm thin films with bottom detectors. The only exception is the intermediate 30 nm film with top Pt detector, in which the competing mechanisms balance each other, resulting in small R_{AHE} magnitude and fluctuating sign with temperature.

Figure 4.6(c) and **Figure 4.6(d)** present the temperature dependence of H_c for samples with different thickness. Here we exclude the 30 nm thick sample since it doesn't exhibit clear coercive fields. In addition, we have included an additional Pt/Cr_2O_3/Pt sample in **Figure 4.6(d)** with Cr_2O_3 layer thickness of 23 nm. As the sample is also grown on Al_2O_3/Pt but with an additional top Pt layer, we expect it to have similar epitaxial quality and comparable H_c with the other bottom detector samples. Clearly, we see a trend that the coercive field increases with Cr_2O_3 thickness. Crucially, for 11nm, 14nm, and 23 nm

samples, we observe coercive fields decrease monotonically or stay almost invariant with increasing temperature. These 3 samples also show consistent R_{AHE} polarities. For the 20-30 nm sample and the 45 nm sample, however, the coercive field increases with increasing temperatures and shows a polarity that is opposite to the other three samples.

4.6 Crossover Behavior of Anomalous Hall Hysteresis

The complex thickness and temperature dependence of the anomalous Hall effect suggests the presence of multiple underlying mechanisms in the Cr_2O_3/Pt heterostructures. In the thin limit, the observation of sharp rectangular loops and coercive fields that decrease with increasing temperature is characteristic of ferromagnetic or ferrimagnetic behavior.

The emergence of ferrimagnetism in epitaxial Cr_2O_3 thin films has been reported and systematically investigated by Kosub et al. [149], whose key findings are summarized in **Figure 4.7**. Through detailed structural characterization, they revealed a strong correlation between the areal magnetization (ρ_m) and the lattice misfit between the Cr_2O_3 films and their underlying substrates, as shown in **Figure 4.7(a)**. Among the examined underlayers, including Al_2O_3, Pt, and V_2O_3, V_2O_3 provides the smallest lattice misfit with Cr_2O_3 and consequently yields nearly vanishing ferrimagnetism. The ferrimagnetic moment arises from misfit dislocations formed at the heterointerface during heteroepitaxial growth, as illustrated schematically in **Figure 4.7(e)** and visualized in the high-resolution transmission electron microscopy (HRTEM) image in **Figure 4.7(f)**. These dislocations

induce a net interfacial moment that couples to the Néel vector, with the sign of the coupling determined by whether the strain is compressive or tensile.

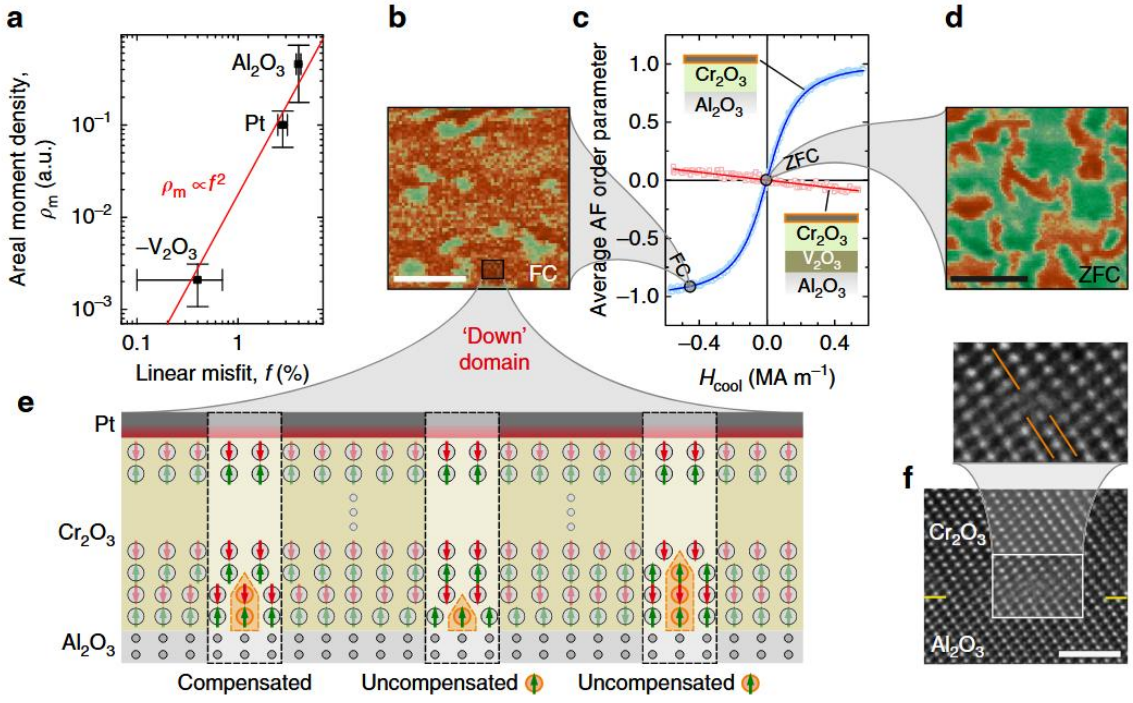


Figure 4.7 Ferrimagnetism in Cr_2O_3 Thin Film Reproduced from Ref. [149].

Interestingly, we observe similar structural defects in our recent study of the $Al_2O_3(11\bar{2}0)/Cr_2O_3$ epitaxial heterostructure using HRTEM (**Figure 2(c)** in Ref. [169]). Moreover, according to their study, Cr_2O_3 grown directly on Al_2O_3 exhibits a larger areal magnetization than Cr_2O_3 grown on a Pt substrate. Qualitatively, this difference can account for the distinct behaviors observed in our top-detector ($Al_2O_3/Cr_2O_3/Pt$) and bottom-detector ($Al_2O_3/Pt/Cr_2O_3$) samples.

If we attribute the Néel vector switching in the thin samples (**Figure 4.5(a)** and **4.5(d)**) to the presence of an areal magnetic moment induced by lattice misfit, we can construct a simple model for the switching process. The switching occurs when the Zeeman coupling overcomes the uniaxial anisotropy energy, such that

$$\mu_0 \rho_m A H \geq K_u V = K_u A t$$

where ρ_m is the areal magnetization density, K_u is the uniaxial anisotropy energy density, t is the Cr_2O_3 thickness, and A is the interfacial area. From this relation, the critical switching field can be expressed as

$$H_c = \frac{K_u t}{\mu_0 \rho_m} \propto \frac{t}{\rho_m}$$

We note that this model assumes a uniform coherent switching process, which may not reflect the actual microscopic switching mechanism. As discussed in **Section 3.8.2**, the real energy cost for Néel vector reversal is generally much smaller than predicted by a single-domain coherent model, owing to the involvement of domain nucleation and domain-wall motion. Nonetheless, this simplified expression captures the correct qualitative trend observed experimentally: as the film thickness increases, a larger magnetic field is required to induce switching, until the field becomes insufficient to overcome the anisotropy, leading to the disappearance of the ferromagnet-like behavior.

Furthermore, since the Al_2O_3/Cr_2O_3 interface is likely to induce a larger interfacial magnetization density ρ_m than the Pt/Cr_2O_3 interface, we expect the ferromagnetic-like behavior to persist to greater thicknesses in the $Al_2O_3/Cr_2O_3/Pt$ samples compared to the $Al_2O_3/Pt/Cr_2O_3$ configuration. This expectation is consistent with our experimental observations.

Though this model qualitatively explains our results and the difference between different substrates, it is questionable that such small surface moments can induce AFM order switching across thin films. From the TEM image in **Figure 4.7(f)**, uncompensated Cr atoms due to dislocation at the interface are only a small portion. In addition, energy-dispersive X-ray (EDX) spectroscopy reveals another type of point defects in our sample, the oxygen vacancies (Figure 4 in Ref. [169]). Notably, the Cr/O ratio gradually increases with film thickness, showing more than a 20% rise at a depth of 26 nm.

Foner [165] discussed that the nonzero longitudinal susceptibility in Cr_2O_3 can be attributed to the presence of point defects (vacancies). A point defect locally disturbs the spin alignment of neighboring ions, and this perturbation can extend over a large spatial range. Under an applied magnetic field, the misaligned spins from both sublattices experience a torque, contributing to the overall magnetic response. Therefore, oxygen deficiencies may also play an important role in the observed magnetic behavior.

To explain the contrasting AHE behavior in thinner films and thicker films, we propose another possible mechanism that can potentially drive the Néel vector switching with the introduction of Dzyaloshinskii–Moriya interactions (DMIs). The presence of DMIs at Cr_2O_3 surface and interface has been evidently shown by different studies [184,187]. Our recent study also suggests a possible formation of spin texture at spin-flop transition at Pt/Cr_2O_3 interface due to DMI [150]. With the introduction of DMI, we found that Cr_2O_3 AFM order can be reversed at a field close to the spin-flop transition field using a simple two-sublattice macrospin simulation method. The result is shown in **Figure 4.8**.

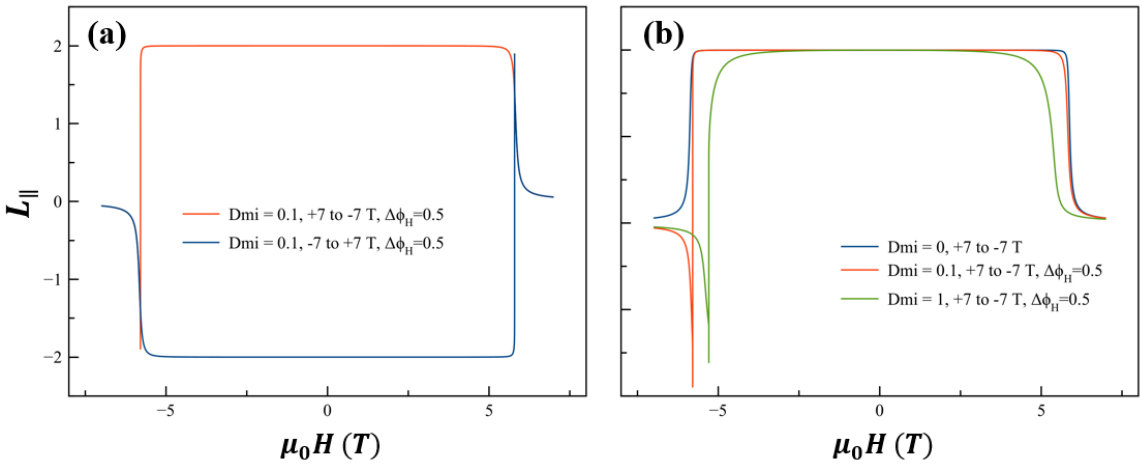


Figure 4.8 Macrospin Simulations with DMI (a)Magnetic field response of $L_{\parallel}$, the Néel vector component along c-axis. Orange curve is by changing magnetic field from 7T to -7T, blue curve is by changing magnetic field from -7T to 7T (b) Magnetic field response of $L_{\parallel}$ with different DMI strength. Simulation details in section 4.8.

Briefly, when there is a small misalign ($\Delta\phi_H = 0.5^{\circ}$) of the applied magnetic field from the easy axis, which is common in experiments, the presence of DMI can drive a switching of the Néel vector right before spin-flop transition. More details about the simulations are included in **Section 4.8.4**. This can explain the temperature dependence of Hc plotted in **Figure 4.6** for the thicker samples, where the coercive field closely follows the increment of the spin-flop transition. The DMI-driven mechanism can potentially drive Néel vector in the opposite directions to the ferrimagnetism, giving rise to opposite sign of the anomalous Hall effects.

4.7 Summary

We have investigated thin film heterostructures of Cr_2O_3 and Pt epitaxially grown on Al_2O_3 substrates. The observation of anomalous Hall hysteresis serves as a clear signature of Néel vector reversal driven by an external magnetic field, as evidenced by the opposite magnetic responses detected in the top and bottom Pt layers.

We further examined the temperature dependence of the anomalous Hall hysteresis in samples with varying Cr_2O_3 thicknesses and stacking configurations. Our results reveal that, depending on both the film thickness and the choice of underlayer, the Néel vector can be driven in opposite directions under the same magnetic-field polarity.

To interpret these complex behaviors, we propose several possible mechanisms involving surface ferrimagnetism and Dzyaloshinskii–Moriya interaction (DMI), which qualitatively account for the observed thickness and temperature dependence. However, our results are not yet conclusive. Additional factors, such as oxygen vacancies [162], flexomagnetism [218], and interfacial electric-field–induced magnetic imbalance [176], may also contribute to the observed effects.

This study is still in progress. Further insights are expected through more precisely controlled epitaxial growth, systematic thickness- and temperature-dependent measurements, and magnetometry characterizations (see **Section 4.8.5** for preliminary result of a 600 nm thin film). A more comprehensive understanding of the anomalous Hall effect in Cr_2O_3 could ultimately pave the way toward its integration in future spintronic applications.

4.8 Supporting Information

In this section, I present additional experimental details, complementary measurements, and discussions that are essential for a comprehensive understanding of this work.

4.8.1 Pulsed Laser Deposition and Reflective High Energy Electron Diffraction

High-quality epitaxial thin films of Cr_2O_3 were grown using pulsed laser deposition (PLD), a versatile technique particularly well-suited for complex oxide materials. In PLD, a high-power pulsed laser is focused onto a solid target, generating a plasma plume that deposits material onto a heated substrate under controlled vacuum and ambient conditions. The energetic nature of this process enables stoichiometric transfer of the target composition to the film, which is especially advantageous for multi-component oxides such as Cr_2O_3.

The PLD system shown in **Figure 4.9** consists of a high-vacuum growth chamber equipped with a pulsed ultraviolet excimer laser (KrF, $\lambda = 248$ nm), a rotating target holder, a substrate heater, and gas inlets for controlling the oxygen/ozone partial pressure. The key parameters governing film quality include laser fluence, repetition rate, substrate temperature, and background gas pressure. By optimizing these parameters, one can precisely control the film thickness, crystallinity, and stoichiometry.

During deposition, in-situ reflection high-energy electron diffraction (RHEED) is employed to monitor the film growth in real time. In a RHEED system, a high-energy

electron beam impinges the substrate surface at a grazing angle, and the diffracted electrons form a characteristic pattern on a phosphor screen. The RHEED pattern provides direct information about the surface morphology, crystallinity, and growth mode of the film. For instance, the appearance of sharp streaks indicates a smooth, well-ordered surface typical of layer-by-layer (2D) growth, while spotty or ring-like patterns correspond to rough or polycrystalline surfaces.

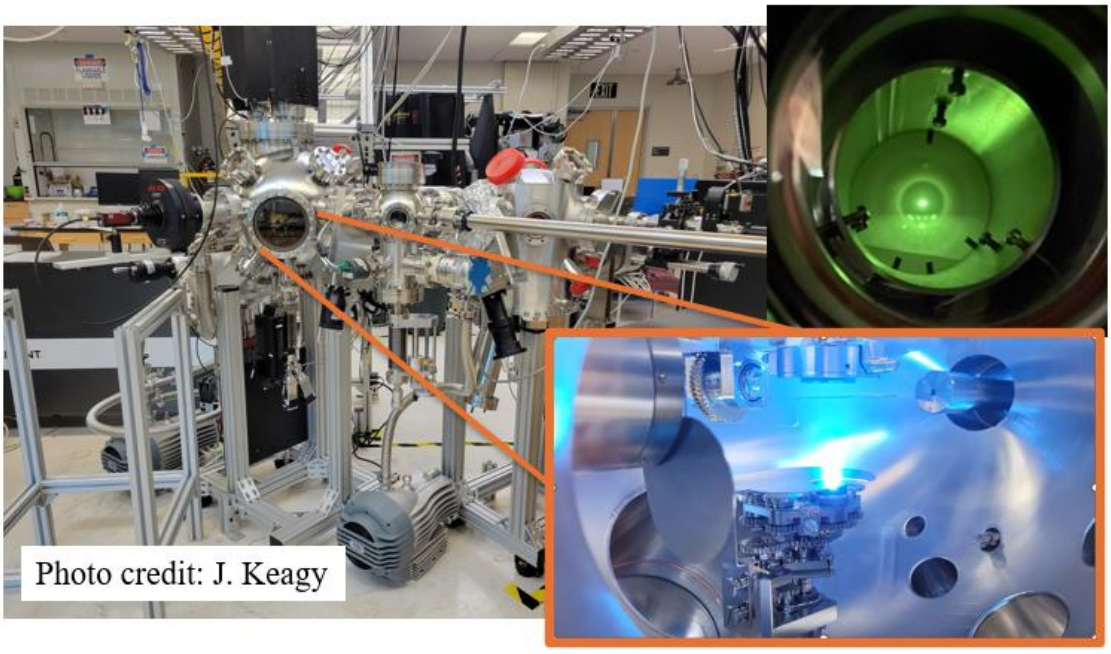


Figure 4.9 Pulsed Laser Deposition (PLD) and Reflection High Energy Electron Diffraction (RHEED) PLD system equipped with in-situ RHEED for real-time growth monitoring, located in Dr. Jing Shi's lab at UC Riverside.

4.8.2 Device Fabrication

Cr_2O_3/Pt Hall bar devices were fabricated using standard microfabrication techniques. For Cr_2O_3/Pt heterostructures, platinum layers were first deposited onto the Cr_2O_3 surface by DC magnetron sputtering under standard deposition conditions. The device geometry was subsequently defined through photolithography, followed by argon ion milling to pattern the Hall crosses. After patterning, a lift-off process was performed to remove excess resist and complete device definition. The samples were then annealed using rapid thermal annealing in oxygen environment at 450℃ for 2 mins to improve the interface quality and stabilize the film properties.

For Pt/Cr_2O_3 structures, the Hall cross geometry was defined by photolithography prior to etching through both the Cr_2O_3 and underlying Pt layers to ensure full isolation of the active region.

For Pt/Cr_2O_3/Pt trilayer devices, after etching through the top Cr_2O_3 and Pt layers, a thin Al_2O_3 capping layer was deposited to passivate the exposed edges and suppress potential edge leakage currents. The top Pt electrode pattern was then defined and deposited to complete the device fabrication.

4.8.3 Spin-Flop Transition in Epitaxial Cr_2O_3 Thin Films

The spin flop transition fields in Cr_2O_3 thin film samples are determined as described in **Figure 4.10(a)**. The nonlinear anomalous Hall response at high-field region is extracted from the loop (inset of **Figure 4.10(a)**) and differentiates to find the point with maxima slope. This field is defined as spin-flop transition field for thin film samples.

Figure 4.10(b) show spin-flop transition field for Cr_2O_3 single crystal and two selected thin film samples (corresponding to the samples in **Figure 4.5(a)** and **4.5(e)**). Surprisingly, while the 11 nm top Pt sample shows spin-flop transition field larger than single crystal, the 20-30 nm bottom Pt sample show H_{SF} very close to the crystal. The relation between H_{SF} and stacking sequence and thickness are yet to be investigated.

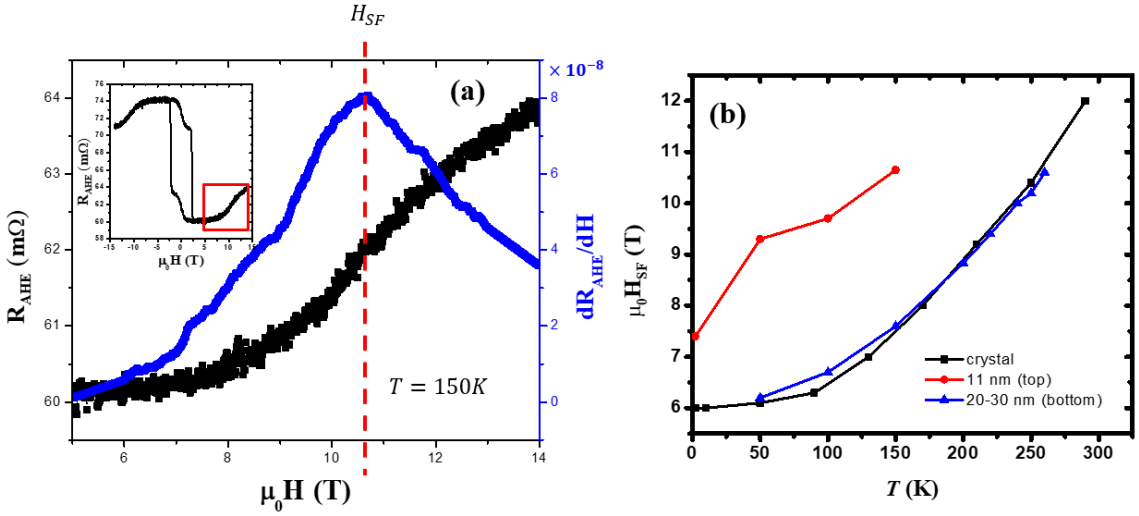


Figure 4.10 Spin-Flop Transition in Cr_2O_3 Thin Film (a) Spin-flop transition in 11 nm top Pt sample at 150K. (b) Temperature dependence of H_{SF} in different samples.

4.8.4 Simulation Details

The magnetic behavior of Cr_2O_3 was modeled using a two-sublattice antiferromagnetic system, where each sublattice magnetization vector ($\mathbf{m}_1$, $\mathbf{m}_2$) is normalized to unity. The total free energy density includes Zeeman, uniaxial anisotropy, exchange, and Dzyaloshinskii–Moriya interaction (DMI) terms,

$$F = -\mu_0 M_s \mathbf{H} \cdot (\mathbf{m}_1 + \mathbf{m}_2) - K_u[(\mathbf{m}_{1z})^2 + (\mathbf{m}_{2z})^2] - J\,\mathbf{m}_1 \cdot \mathbf{m}_2 - D(\mathbf{m}_1 \times \mathbf{m}_2) \cdot \hat{x}$$

where $\hat{z}$ is the easy axis and the DMI vector is along $\hat{x}$. The dynamics of each sublattice were calculated by numerically integrating the coupled Landau–Lifshitz–Gilbert (LLG) equations.

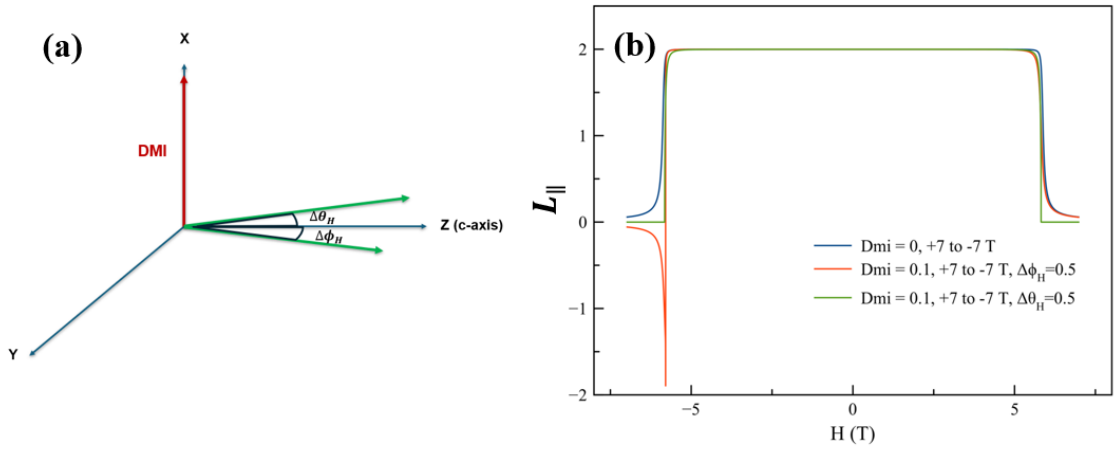


Figure 4.11 Simulation Detail (a) Simulation configuration. (b) Magnetic field misalign towards y axis induced the Néel vector reversal while misalign towards x axis not.

The external magnetic field was applied nominally along the c-axis (z-axis) with a small tilt either toward x (θ_H) or toward y (ϕ_H) to simulate experimental misalignment. Field sweeps were performed from $+7$ T to -7 T and back in discrete steps, with the

steady-state solutions at each step serving as the initial condition for the next. The Néel vector $\mathbf{L} = \mathbf{m}_1 - \mathbf{m}_2$ was recorded as a function of field, and its z-component (L_z) was used to construct the hysteresis loop. Interestingly, only small ϕ_H will induce Néel vector reversal.

4.8.5 Magnetometry Characterization on Epitaxial Cr_2O_3 Thin Film

Figure 4.12 shows the magnetic moment as a function of the out-of-plane magnetic field (H ∥ c-axis) for a 600-nm-thick epitaxial Cr_2O_3 thin film, measured at temperatures ranging from 10 K to 330 K. At low temperatures (T ≤ 250 K), the moment exhibits a characteristic upturn above 4 T (and a downturn below -4 T), consistent with the emergence of a canted magnetic moment associated with the spin-flop transition in antiferromagnetic Cr_2O_3. This field-induced canting appears at a noticeably lower field compared to bulk Cr_2O_3 as shown by the top curve, which is measured at 10K and normalized in terms of thickness, likely reflecting the broadened spin-flop transition commonly observed in thin-film geometries [169]. For temperatures above 300 K, the M–H curves become nearly flat, as expected when the film is driven above its Néel temperature and long-range antiferromagnetic order is lost. In addition, a relatively large moment near H = 0 T is observed across all temperatures. This feature may indicate the presence of parasitic ferrimagnetic contributions, potentially arising from interfacial effects, defects, or uncompensated surface spins, and is the subject of ongoing investigation.

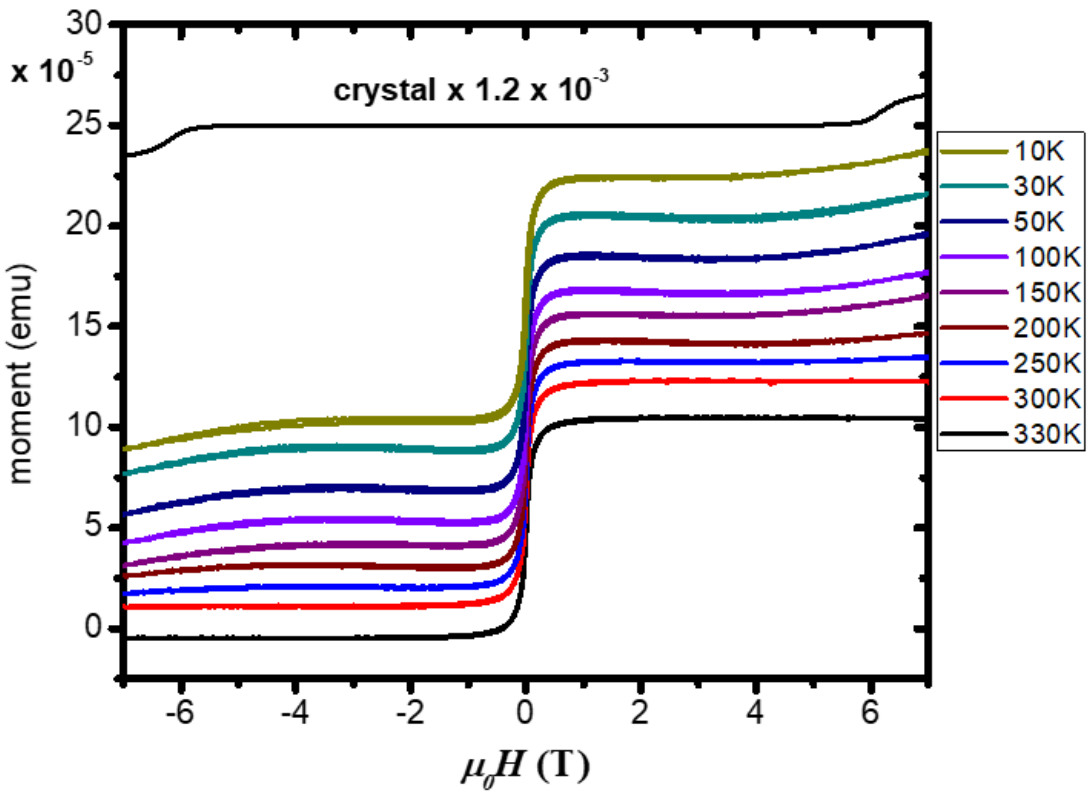


Figure 4.12 Magnetometry Characterization of 600 nm Cr_2O_3 Thin Film The top curve displays the M-H curve of Cr_2O_3 crystal (thickness = 0.5 mm) measured at 10K normalized by relative thickness.

4.8.6 Magnetoelectric Effect in Cr_2O_3 Thin Films

We investigated the magnetoelectric effect in a Cr_2O_3 thin film grown on an Al_2O_3/Pt substrate. To prevent leakage during gate manipulation, we transferred an hBN/graphite top gate onto the device, forming a multilayer stack as shown in **Fig. 4.13(a)**. The gate voltage is applied between the top graphite gate and the bottom Pt detector, and the anomalous Hall signal is measured through the same Pt detector. We estimate the Cr_2O_3 thickness to be 14 nm and the hBN thickness to be 50 nm.

As with the previous devices discussed in this chapter, we observe a clear AHE hysteresis loop during magnetic-field sweeps. Importantly, the coercive field changes systematically with the applied electric field, as shown in **Fig. 4.13(b)**. A positive electric field increases the coercive field, while a negative electric field decreases it. This behavior is consistent with the presence of a small spontaneous ferrimagnetic moment together with a magnetoelectric contribution to the interfacial moment.

To gain a simple quantitative estimate, we model the system using a Stoner–Wohlfarth–type coherent-rotation picture. The free energy is written as

$$F = -\mu_0 MH\cos\theta - K_u\cos^2\theta$$

Solving for the switching condition gives the critical field

$$H_c = \frac{2K_u}{\mu_0 M}$$

In practice, the measured switching field is much smaller due to domain dynamics such as nucleation and domain wall motion, so we replace K_u with an effective value $K_{\text{eff}} < K_u$. In our case, we assume that the total moment contains two contributions: a

spontaneous ferrimagnetic moment M_{FM}, and a magnetoelectrically induced moment $\mu_0 M_{\mathrm{ME}} = \alpha E$. The critical field then becomes

$$H_c = \frac{2K_{eff}}{\mu_0 M_{FM} + \alpha E}$$

Or equivalently,

$$\frac{1}{H_c} = \frac{\alpha}{2K_{eff}} E + \frac{\mu_0 M_{FM}}{2K_{eff}}$$

Thus, a plot of $1/H_c$ versus E yields a slope of $\alpha/(2K_{\mathrm{eff}})$ and an intercept of $(\mu_0 M_{\mathrm{FM}})/(2K_{\mathrm{eff}})$, enabling estimates of both the magnetoelectric-induced moment and the spontaneous ferrimagnetic moment. **Figure 4.13(c)** shows this plot for the present sample (black dots), together with a linear fit (red line). From the fit we obtain $\frac{\alpha}{2K_{eff}} \approx 8 \times 10^{-16}$ and $\frac{\mu_0 M_{\mathrm{FM}}}{2K_{\mathrm{eff}}} \approx 10^{-6}$.

Taking a typical magnetoelectric coefficient $\alpha \sim 10^{-12}$ $(\frac{s}{m})$, we estimate an effective anisotropy $K_{\mathrm{eff}} \sim 10^3$–$10^4$ $\left(\frac{J}{m^3}\right)$, which is smaller than the Cr_2O_3 intrinsic uniaxial anisotropy $K_u \sim 2 \times 10^4$ $(\frac{J}{m^3})$. The spontaneous ferrimagnetic moment can be extracted using

$$M_{FM} = \frac{\alpha}{\mu_0}\left(\frac{\mu_0 M_{FM}}{2K_{eff}}\right)\left(\frac{\alpha}{2K_{eff}}\right)^{-1} \sim \left(\frac{10^{-12}}{4\pi \times 10^{-7}}\right)\frac{(10^{-6})}{8 \times 10^{-16}} \sim 1000\frac{A}{m} \; or \; 1 \; \frac{emu}{cm^3}$$

This value can be compared with bulk magnetometry by multiplying by the Cr_2O_3 film volume:

$$M_{total} = M_{FM} \times V_{Cr_2O_3} \sim 1 \; \frac{emu}{cm^3} \times 0.5 \; cm \times 0.5 \; cm \times 14 \; nm \sim 3.5 \times 10^{-7} \; emu$$

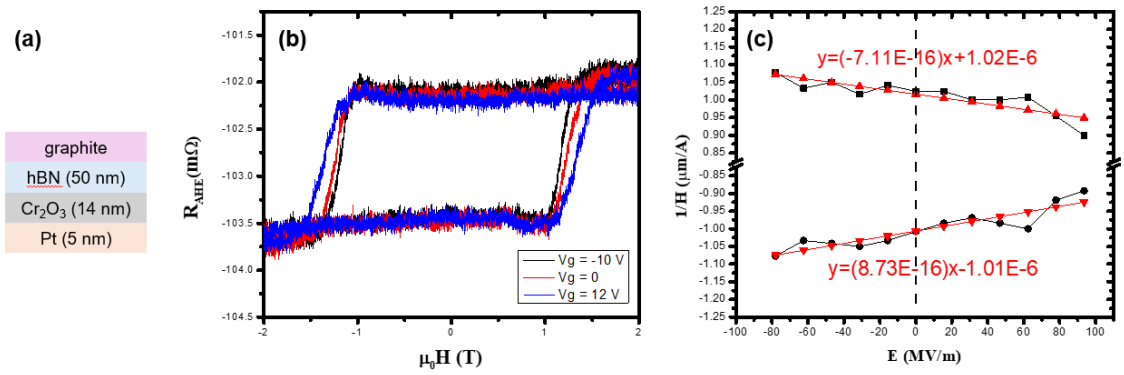


Figure 4.13 Magnetoelectric Effect and Spontaneous Ferrimagnetism in Cr_2O_3 Thin Films (a) Schematic of the gated Cr_2O_3 device. (b) Anomalous Hall hysteresis loops measured under different applied electric fields. (c) Plot of $1/H_c$ as a function of electric field E (black dots), together with linear fit (red line).

Chapter 5 Probing Magnetism and Proximity Phenomena in 2D Antiferromagnetic $MnPS_3$ Heterostructures

$MnPS_3$ is a 2D van der Waals antiferromagnet and linear magnetoelectric material. In this chapter, I will discuss our preliminary results on the investigation of $MnPS_3$ heterostructures. In $MnPS_3$/Pt heterostructure, we observed robust and nearly isotropic negative magnetoresistance (MR), which indicates a strong interfacial magnetic interaction at the magnetic-heavy metal interface. Furthermore, high-field nonlinear Hall feature emerges below its Néel temperature, indicating detection of the spin-flop transition in $MnPS_3$ using Pt layer. In the $MnPS_3$/WTe_2 heterostructure, proximity effect lowers the onset field of quantum oscillations. We attribute this phenomenon to a proximity-induced exchange field interacting with the strong intrinsic spin-orbit coupling of the WTe_2, enabled by spin-flop transition in $MnPS_3$. Overall, this chapter demonstrates the rich interfacial physics enabled by $MnPS_3$ heterostructures, offering new platforms for studying 2D magnetoelectric antiferromagnet spintronics.

5.1 Motivation and Background

$MnPS_3$ is a rare example of a two-dimensional (2D) van der Waals (vdW) linear magnetoelectric (ME) antiferromagnet, offering a unique platform to explore antiferromagnetism and magnetoelectric coupling in reduced dimensions. Its linear ME properties have been experimentally confirmed by neutron polarimetry [228] and second harmonic generation (SHG) studies [229], which reveal that the ME response originates from its distinct antiferromagnetic spin arrangement. The ME tensor of $MnPS_3$ corresponds to a ferrotoroidic order [228], distinguishing it from related compounds such as $FePS_3$ and $NiPS_3$, which lack linear ME coupling due to their different spin symmetries.

Importantly, antiferromagnetic order in $MnPS_3$ exhibits below its Néel temperature of 78 K [230,231] and persists down to the monolayer limit [232], making it one of the known 2D materials that retain long-range magnetic order at the atomic scale. Beyond its magnetoelectric behavior, $MnPS_3$ has been investigated for magnonic transport and thermal effects [233–235], and exchange bias [236] phenomena, positioning it as a versatile material for studying fundamental spin interactions and for developing future spintronic and magnetoelectric device concepts.

Due to large bandgap over 3eV, it is challenging to directly probe $MnPS_3$ through electrical means. In this chapter, we explored how $MnPS_3$ imprint its magnetism when brought into proximity with other materials, including Pt and 2D Weyl semimetal WTe_2.

5.2 Magnetic Properties of $MnPS_3$ Bulk Crystal

The magnetic properties of the $MnPS_3$ single crystal were characterized using magnetometry, as shown in **Fig. 5.1(a)**. A magnetic field is applied along the c-axis of the crystal. Below its Néel temperature $T_N = 78\,\mathrm{K}$, we observe a nonlinear increase in magnetization around 6 T, characteristic of the spin-flop transition. As the temperature is further reduced to 10 K, the spin-flop field H_{SF} decreases to approximately 4 T. In addition, a small jump near $H = 0$ is observed at low temperatures, which may originate from magnetic impurities. The temperature dependence of H_{SF} is plotted in **Fig. 5.1(b)**, indicating that the spin-flop transition field of bulk $MnPS_3$ lies in the range of 4–6 T.

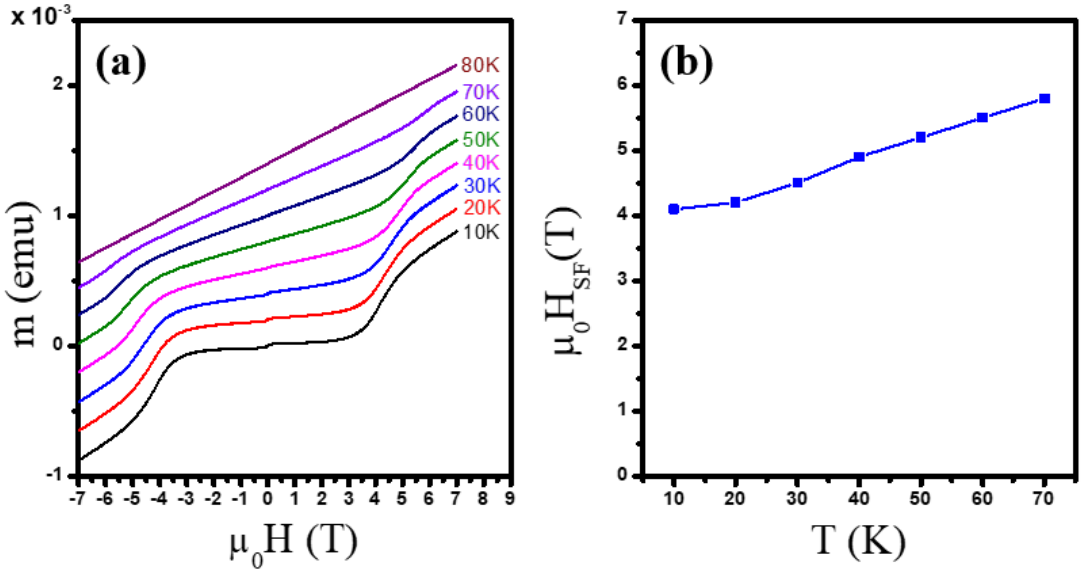


Figure 5.1 Magnetic Properties of $MnPS_3$ Single Crystal (a) m-H curves at different temperatures. (b) H_{SF} vs. T.

5.3 Fabrication of $MnPS_3$ Heterostructure Devices

$MnPS_3$ flakes were mechanically exfoliated from a commercial crystal on a Si/SiO_2 substrate inside a glovebox filled with argon gas to minimize degradation and oxidation. The selected flakes were then immediately transferred into a magnetron sputtering chamber, where a 5 nm Pt layer was deposited on top to form $MnPS_3$/Pt heterostructures. Standard electron-beam lithography and Ar ion etching were subsequently employed to define the Hall bar geometry. For comparison, a Pt control device is simultaneously fabricated on the same substrate using a spare area under identical conditions to ensure consistency in film quality and measurement environment.

$WTe_2/MnPS_3$ heterostructure devices were fabricated using a fully inert-atmosphere exfoliation and assembly process. Bulk WTe_2 and $MnPS_3$ crystals were mechanically exfoliated inside an argon-filled glovebox to obtain thin flakes on Si/SiO_2 substrates. Suitable $MnPS_3$ (~20 nm) and WTe_2 (~10 nm) flakes were then sequentially picked up and transferred onto prepatterned metal electrodes using a dry-transfer technique as described in **Section 5.7.1**, ensuring clean interfaces and minimal exposure to ambient conditions. After assembly, the heterostructure was encapsulated with a hexagonal boron nitride (hBN) layer to protect the air-sensitive materials and to enhance device stability during measurements. A WTe_2 control device was fabricated following the same procedure but without incorporating $MnPS_3$. This approach ensures high-quality interfaces and reliable comparison between the heterostructure and control samples.

5.4 Magnetoresistance and AHE in $MnPS_3$/Pt

We performed four-terminal longitudinal and transverse resistance measurements on both the Pt control device (**Figure 5.2(a)**) and the $MnPS_3$/Pt device (**Figure 5.2(d)**) under an external magnetic field applied along the c-axis, i.e., the out-of-plane direction of the sample. The corresponding magnetoresistance ($MR = \Delta R_{xx}/R_{xx}$) and Hall resistance as functions of the applied field are shown in **Figures 5.2(b,c)** and **5.2(e,f)**, respectively.

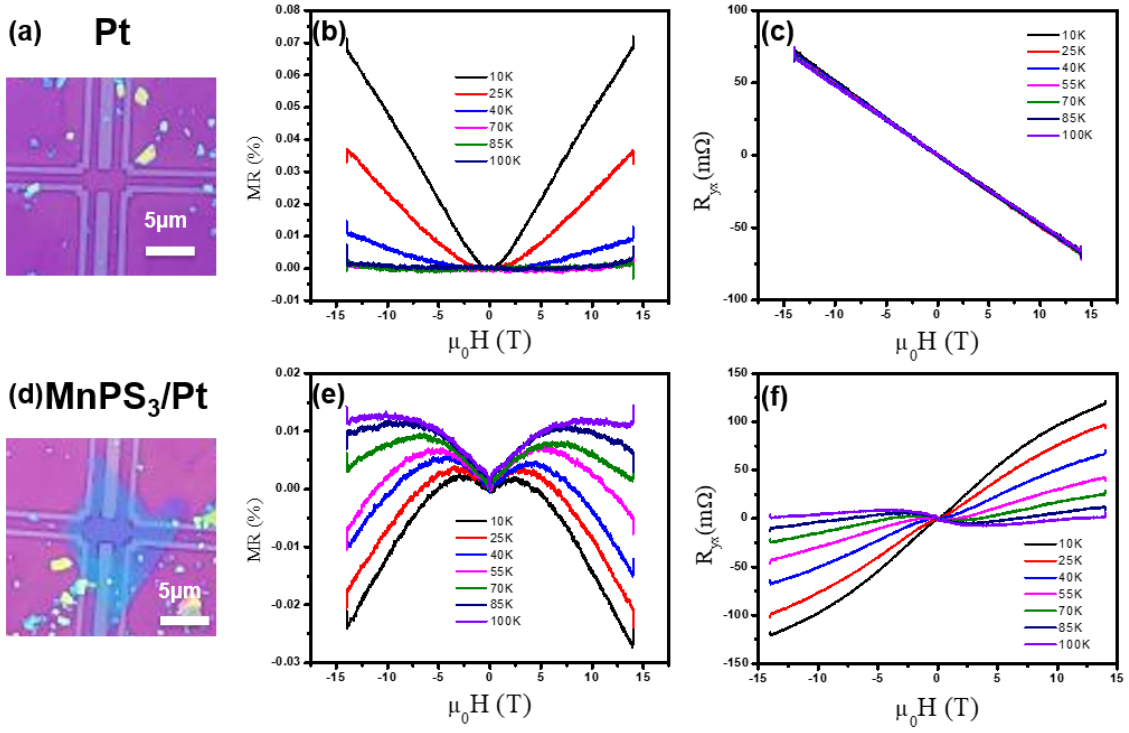


Figure 5.2 Comparison Between Pt and $MnPS_3$/Pt Magnetoresistance and Hall (a) Optical image of Pt control device. (b) Magnetoresistance of Pt control device. (c) Hall resistance of Pt control device. (d) Optical image of $MnPS_3$/Pt device. (e) Magnetoresistance of $MnPS_3$/Pt device. (f) Hall resistance of $MnPS_3$/Pt device.

Clear differences emerge between the two devices. The Pt control sample exhibits a conventional positive magnetoresistance that increases with magnetic field (**Figure 5.2(b)**). In contrast, the $MnPS_3$/Pt heterostructure shows a pronounced suppression of resistance at high fields (**Figure 5.2(e)**), resulting in a negative MR that remains unsaturated up to H = 14 T. This behavior provides direct evidence of strong interfacial magnetic interactions in the $MnPS_3$/Pt system that substantially influence charge transport in the Pt layer.

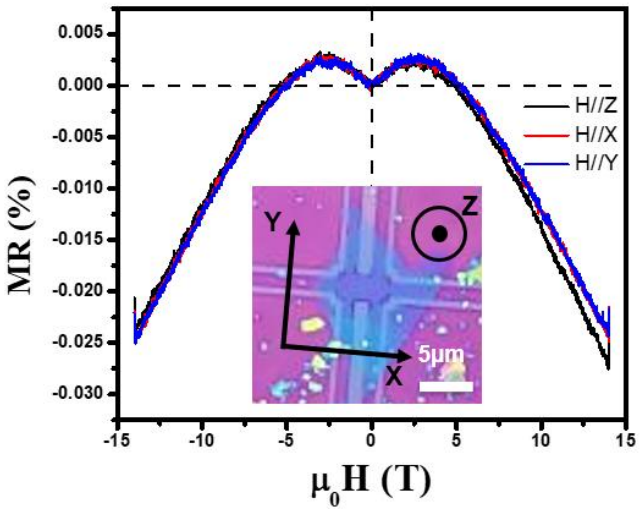


Figure 5.3 Magnetoresistance of the $MnPS_3$/Pt Device Measured at T = 10 K The three curves correspond to magnetic fields applied along the z, x, and y directions as defined by the inset.

Interestingly, this high-field MR suppression is nearly isotropic when the field is applied along the x, y, or z directions as shown in **Figure 5.3**. The isotropic nature and the absence of correlation with the Néel temperature or spin-flop transition of $MnPS_3$ suggests that this effect does not directly arise from the long-range antiferromagnetic order. Instead,

it likely originates from spin-dependent scattering at the $MnPS_3$/Pt interface. We notice that a recent study on $MnPSe_3$/Pt shows a similar negative magnetoresistance due to the formation of spin disordered interface [237], and a similar mechanism may be at play in our $MnPS_3$/Pt device. The applied magnetic field may align interfacial spins or reduce spin disorder, thereby decreasing spin-flip scattering and leading to the observed negative MR.

In Hall measurements, the $MnPS_3$/Pt heterostructure exhibits a clear contrast to the Pt control sample. The Pt control shows a typical linear ordinary Hall effect with a negative slope (**Figure 5.2(c)**), consistent with electrons being the dominant charge carriers. In contrast, the $MnPS_3$/Pt device displays a reversed slope and pronounced nonlinearity in the Hall response with respect to the applied magnetic field (**Figure 5.2(f)**). This behavior suggests the emergence of an additional contribution beyond the ordinary Hall effect, potentially arising from proximity-induced magnetism at the $MnPS_3$/Pt interface.

Figure 5.4(a) presents the anomalous Hall resistance R_{AHE} of the $MnPS_3$/Pt heterostructure after subtraction of the linear ordinary Hall background from **Figure 5.2(f)**. A pronounced nonlinear increase in the Hall signal is observed at high magnetic fields below T_N, indicating an additional magnetic contribution. This nonlinear feature can be attributed to the spin-flop transition of $MnPS_3$, suggesting that the Pt layer is sensitive to the canted moment through proximity coupling. In **Figure 5.4(b)**, we plot $\frac{dR_{AHE}}{dH}$ as a function of temperatures at different magnetic fields larger than the spin-flop transition field H_{SF}, which clearly shows the emerging nonlinearity below T_N.

This interpretation is further supported by comparing the extracted AHE signal from Pt with magnetometry data measured on bulk $MnPS_3$ single crystals as shown in

Figure 5.4(c). The overall field dependence of the Pt AHE closely resembles the M–H curve of $MnPS_3$, confirming that the Hall response reflects the spin reorientation of the antiferromagnetic sublattices. Notably, the observed spin-flop field of the $MnPS_3$/Pt is larger than that in the $MnPS_3$ single crystal, which can be attributed to finite-size effects, strain, or interface-induced modification of the magnetic anisotropy. These results demonstrate that Pt can serve as an effective probe of the $MnPS_3$ magnetic state through magnetic proximity effect. A comparison between AHE in $MnPS_3$/Pt and Cr_2O_3/Pt is provided in **Section 5.7.2**.

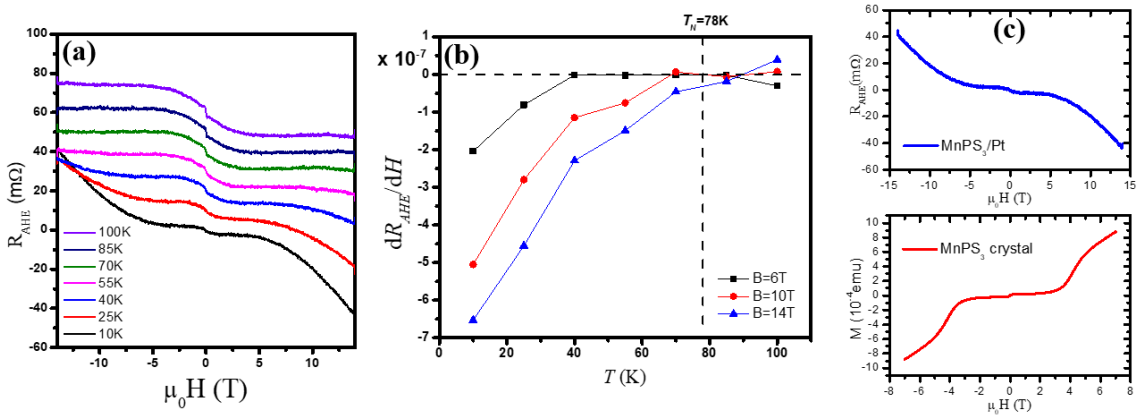


Figure 5.4 Anomalous Hall Effect in $MnPS_3$/Pt (a) $R_{AHE} - H$ at different temperatures. (b) $\frac{dR_{AHE}}{dH} - T$ at different magnetic fields. (c) Comparison between $R_{AHE} - H$ and $M - H$ curves.

5.5 Quantum Oscillations in $WTe_2/MnPS_3$

2D/2D interfaces formed between two layered materials offer atomically sharp and chemically clean interface without the constraints of lattice matching or interdiffusion, making them ideal platforms for investigating interfacial spin transport and proximity effects. Tungsten ditelluride (WTe_2) is a topological semimetal [104,105] and transition metal dichalcogenide possessing strong spin–orbit coupling, giving rise to large spin Hall effects. By integrating WTe_2 with $MnPS_3$, we form a 2D/2D magnetic heterostructure to investigate how magnetic coupling influence the transport property across a van der Waals interface.

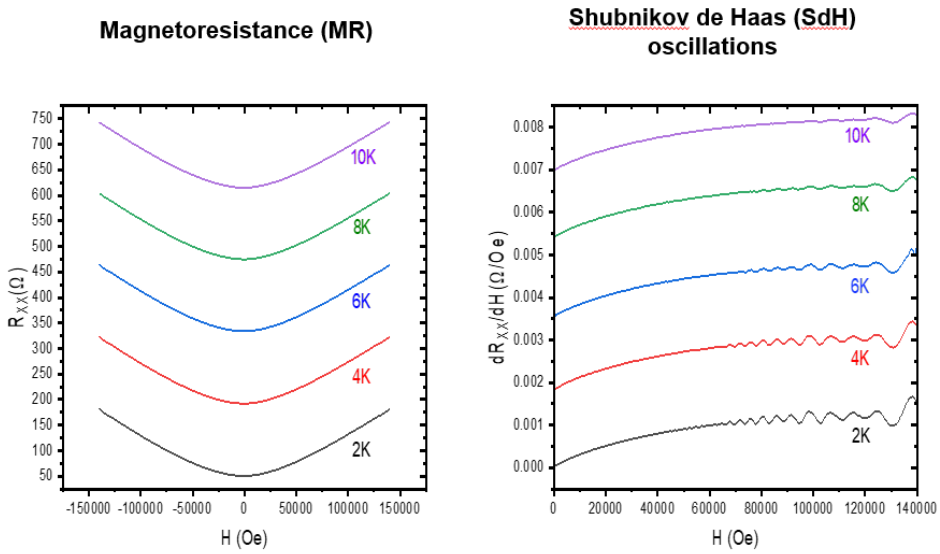


Figure 5.5 Magnetoresistance and SdH Oscillations in $WTe_2/MnPS_3$ $R_{xx} - H$ measured between 2-10K. By taking derivatives, the SdH oscillations are clearly shown at high fields.

Figure 5.5 presents the measured magnetoresistance R_{xx} and $\frac{dR_{xx}}{dH}$ as functions of applied magnetic field for the $WTe_2/MnPS_3$ sample. Magnetotransport measurements were performed at low temperatures with magnetic fields applied perpendicular to the sample plane. By taking derivative, we observe pronounced Shubnikov–de Haas (SdH) quantum oscillations, confirming the high crystalline quality of the exfoliated WTe_2 flakes consistent with previous study on WTe_2 [238].

Figure 5.6(a) compares the SdH oscillations of the $WTe_2/MnPS_3$ heterostructure with the WTe_2 control device. A clear difference is observed in the onset field of the SdH oscillations. In the WTe_2 control sample, SdH oscillations become visible only above approximately 6.6 T, whereas in the $WTe_2/MnPS_3$ device they appear at a substantially lower field of around 4.4 T. Since the onset magnetic field for SdH oscillations scales inversely with carrier mobility, $H_{SdH} \propto \mu^{-1}$, we extracted the carrier mobilities of both samples from Fourier analysis of their oscillation frequencies (see **Section 5.7.3**). Despite the heterostructure exhibiting slightly lower mobility, it nevertheless shows a lower SdH onset field. This inconsistency indicates that the reduced onset field cannot be explained solely by mobility, scattering, or sample quality.

We therefore attribute the lowered SdH onset field in the $WTe_2/MnPS_3$ heterostructure to an interfacial proximity effect. As illustrated in **Figure 5.6(b)**, at approximately 4.4 T, consistent with the spin-flop transition field of $MnPS_3$, the reoriented antiferromagnetic moments can induce an exchange field that couples to the charge carriers in WTe_2. Through spin–orbit interaction, this coupling may modify the quantum coherence

conditions required for SdH oscillations. Further investigation is needed to fully understand the underlying mechanism of this phenomenon.

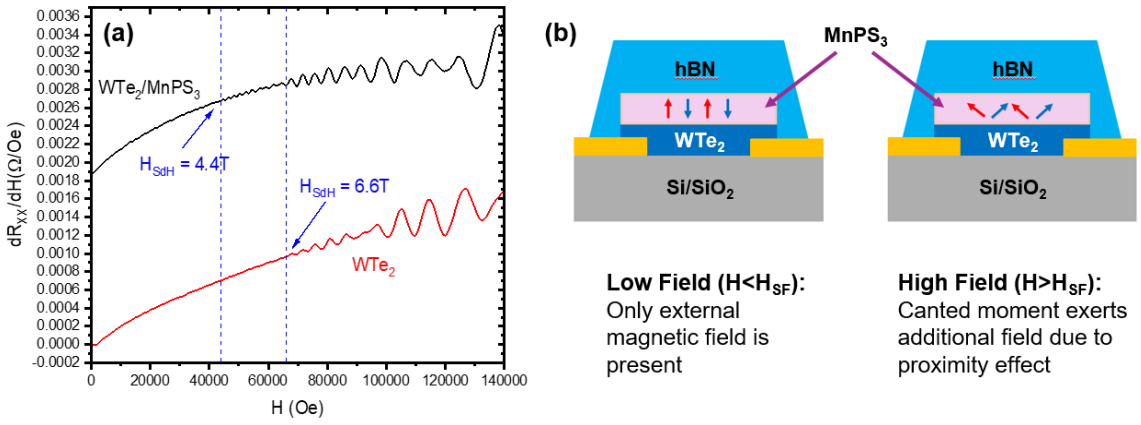


Figure 5.6 Proximity-Enhanced Quantum Oscillations in $WTe_2/MnPS_3$ (a) SdH oscillations for $WTe_2/MnPS_3$ heterostructure and WTe_2 control sample. (b) Canted antiferromagnetic moments exserts additional field due to proximity effect.

5.6 Summary

In summary, we explored heterostructures based on 2D antiferromagnet $MnPS_3$, including $MnPS_3$/Pt and $MnPS_3$/WTe_2. These results demonstrate that $MnPS_3$ imprints its magnetization in the adjacent Pt and WTe_2 layer, establishing a powerful way of investigating magnetism in 2D insulating antiferromagnets, which can potentially work for magnetoelectric and antiferromagnetic spintronic devices.

5.7 Supporting Information

In this section, I present additional experimental details, complementary measurements, and discussions for a comprehensive understanding of this work.

5.7.1 2D Materials Exfoliation and Stacking Techniques

2D materials such as $MnPS_3$ and WTe_2 are mechanically exfoliated from bulk crystals into few-layer flakes on Si/SiO_2 substrates using simple mechanical exfoliation with Scotch tape or Nitto SPV 224 blue tape. The desired flakes are then assembled into heterostructures using a dry transfer technique. In our process, we employ a polycarbonate (PC) thin film supported on a polydimethylsiloxane (PDMS) block and a glass slide as the transfer stamp. The PC thin film is prepared by dissolving commercial polycarbonate pellets in chloroform to form a 6–8% solution, which is cast onto a clean glass slide and left to dry overnight, producing a uniform thin film suitable for picking up 2D materials.

The dry transfer procedure consists of three main steps: picking up, aligning, and releasing the flakes. During pickup, the PC/PDMS/glass stamp is brought into gentle contact with the target flake and lifted at temperatures typically between 80 and 110 °C to retrieve it. The stamp is then aligned with subsequent flakes under an optical microscope. Finally, the assembled stack is released onto the target substrate by gradually lowering the stage and heating to soften the PC, allowing the entire PC/flake stack to fully attach to the substrate. After transfer, the PC layer is dissolved by rinsing the sample in chloroform,

leaving the clean stacked heterostructure on the substrate. The entire process is performed inside an Ar-filled glovebox with O_2 and H_2O concentrations kept below 0.1 ppm.

5.7.2 Comparison of AHE Between Cr_2O_3/Pt and $MnPS_3$/Pt

Both Cr_2O_3 and $MnPS_3$ are insulating magnetoelectric antiferromagnets. However, Cr_2O_3 possesses an uncompensated surface moment along its (0001) plane, whereas $MnPS_3$ is a Néel-type antiferromagnet with fully compensated moments within each layer. As a result, in Cr_2O_3/Pt bilayers, the Pt primarily senses a single sublattice of Cr_2O_3, giving rise to a field-symmetric AHE. In contrast, in $MnPS_3$/Pt, the AHE originates from the canted moments that appear above the spin-flop transition, leading to a field-antisymmetric AHE response.

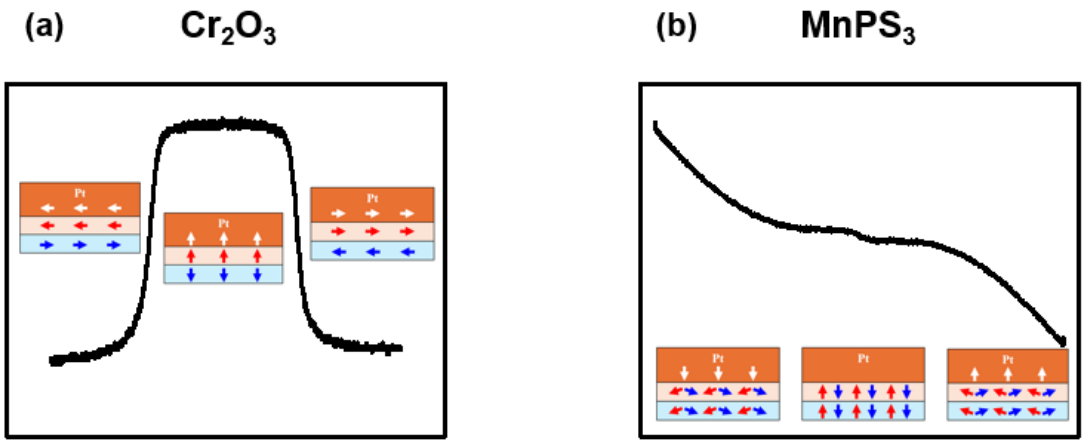
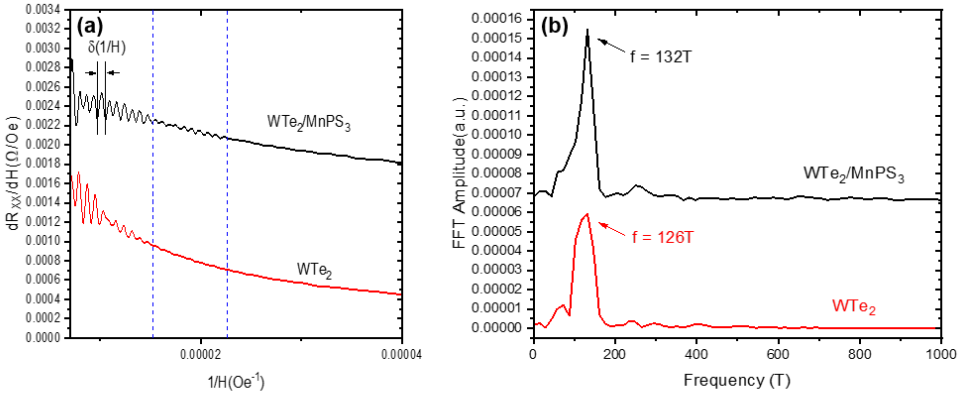


Figure 5.7 Comparison Between AHE in Cr_2O_3/Pt and $MnPS_3$/Pt (a) Cr_2O_3(0001)/Pt (b) $MnPS_3$/Pt.

5.7.3 Determination of Carrier Mobility from Quantum Oscillations

Carrier mobility is a key parameter governing a material's electrical conductivity. Higher mobility generally leads to higher conductivity. Within the Drude model, the conductivity is given by $\sigma = \mu ne$, where μ is the carrier mobility, n is the carrier density, and e is the electron charge. While conductivity can be directly obtained from four-terminal transport measurements, determining the mobility requires an estimate of the carrier density.

We extract the carrier density n from the Shubnikov–de Haas (SdH) oscillations. When plotted as a function of $1/B$, the oscillation period is related to the carrier density through $n = 2ef/h$, where f is the SdH frequency. We plot the oscillations versus $1/B$ in **Figure 5.8(a)** and perform a fast Fourier transform in **Figure 5.8(b)**, obtaining peaks near 132 T and 126 T for the $MnPS_3/WTe_2$ heterostructure and the WTe_2 control sample, respectively. Using these frequencies, we extract the corresponding carrier densities. With both the carrier density and sheet conductivity, the carrier mobility can then be calculated. The values are listed in **Figure 5.8(c)**.



(c)

	n (cm^{-2})	σ_s (S)	μ (cm^2/Vs)	Estimated H_{SdH}	Experimental H_{SdH}
$WTe_2/MnPS_3$	6.4 x 10^{12}	2 x 10^{-2}	1.96 x 10^4	Higher	**Lower**
WTe_2	6.1 x 10^{12}	3.3 x 10^{-2}	3.4 x 10^4	Lower	**Higher**

Figure 5.8 Determination of Carrier Mobility (a) dRxx/dH v.s. 1/H. (b) Fast Fourier transform. (c) Calculated carrier mobility.

References:

[1] W. Thomson, On the electro-dynamic qualities of metals:—Effects of magnetization on the electric conductivity of nickel and of iron, Proc. R. Soc. Lond. **8**, 546 (1857).

[2] E. H. Hall, On a New Action of the Magnet on Electric Currents, Am. J. Math. **2**, 287 (1879).

[3] E. H. Hall, On the "Rotational Coefficient" in Nickel and Cobalt, Proc. Phys. Soc. Lond. **4**, 325 (1880).

[4] N. F. Mott, The electrical conductivity of transition metals, Proc. R. Soc. Lond. Ser. - Math. Phys. Sci. **153**, 699 (1936).

[5] P. Ritzinger and K. Výborný, Anisotropic magnetoresistance: materials, models and applications, R. Soc. Open Sci. **10**, 230564 (2023).

[6] M. N. Baibich, J. M. Broto, A. Fert, F. Nguyen Van Dau, and F. Petroff, Giant Magnetoresistance of (001)Fe/(001)Cr Magnetic Superlattices, Phys. Rev. Lett. **61**, 2472 (1988).

[7] G. Binasch, P. Grünberg, F. Saurenbach, and W. Zinn, Enhanced magnetoresistance in layered magnetic structures with antiferromagnetic interlayer exchange, Phys. Rev. B **39**, 4828 (1989).

[8] S. S. P. Parkin, N. More, and K. P. Roche, Oscillations in exchange coupling and magnetoresistance in metallic superlattice structures: Co/Ru, Co/Cr, and Fe/Cr, Phys. Rev. Lett. **64**, 2304 (1990).

[9] M. Julliere, Tunneling between ferromagnetic films, Phys. Lett. A **54**, 225 (1975).

[10] J. S. Moodera, Large Magnetoresistance at Room Temperature in Ferromagnetic Thin Film Tunnel Junctions, Phys. Rev. Lett. **74**, 3273 (1995).

[11] T. Miyazaki and N. Tezuka, Giant magnetic tunneling effect in Fe/Al_2O_3/Fe junction, J. Magn. Magn. Mater. **139**, L231 (1995).

[12] S. Tehrani, J. M. Slaughter, E. Chen, M. Durlam, J. Shi, and M. DeHerren, Progress and outlook for MRAM technology, IEEE Trans. Magn. **35**, 2814 (1999).

[13] S. Tehrani et al., Magnetoresistive random access memory using magnetic tunnel junctions, Proc. IEEE **91**, 703 (2003).

[14] J. C. Slonczewski, Current-driven excitation of magnetic multilayers, J. Magn. Magn. Mater. **159**, L1 (1996).

[15] L. Berger, Emission of spin waves by a magnetic multilayer traversed by a current, Phys. Rev. B **54**, 9353 (1996).

[16] E. B. Myers, D. C. Ralph, J. A. Katine, R. N. Louie, and R. A. Buhrman, Current-Induced Switching of Domains in Magnetic Multilayer Devices, Science **285**, 867 (1999).

[17] J. A. Katine, Current-Driven Magnetization Reversal and Spin-Wave Excitations in Co/Cu/Co Pillars, Phys. Rev. Lett. **84**, 3149 (2000).

[18] Y. Huai, F. Albert, P. Nguyen, M. Pakala, and T. Valet, Observation of spin-transfer switching in deep submicron-sized and low-resistance magnetic tunnel junctions, Appl. Phys. Lett. **84**, 3118 (2004).

[19] G. D. Fuchs, N. C. Emley, I. N. Krivorotov, P. M. Braganca, E. M. Ryan, S. I. Kiselev, J. C. Sankey, D. C. Ralph, R. A. Buhrman, and J. A. Katine, Spin-transfer effects in nanoscale magnetic tunnel junctions, Appl. Phys. Lett. **85**, 1205 (2004).

[20] W. H. Butler, X.-G. Zhang, and T. C. Schulthess, Spin-dependent tunneling conductance of Fe|MgO|Fe sandwiches, Phys. Rev. B **63**, (2001).

[21] S. Yuasa, T. Nagahama, A. Fukushima, Y. Suzuki, and K. Ando, Giant room-temperature magnetoresistance in single-crystal Fe/MgO/Fe magnetic tunnel junctions, Nat. Mater. **3**, 868 (2004).

[22] S. S. P. Parkin, C. Kaiser, A. Panchula, P. M. Rice, B. Hughes, M. Samant, and S.-H. Yang, Giant tunnelling magnetoresistance at room temperature with MgO (100) tunnel barriers, Nat. Mater. **3**, 862 (2004).

[23] S. Ikeda, K. Miura, H. Yamamoto, K. Mizunuma, H. D. Gan, M. Endo, S. Kanai, J. Hayakawa, F. Matsukura, and H. Ohno, A perpendicular-anisotropy CoFeB–MgO magnetic tunnel junction, Nat. Mater. **9**, 721 (2010).

[24] M. I. Dyakonov and V. I. Perel, Current-induced spin orientation of electrons in semiconductors, Phys. Lett. A **35**, 459 (1971).

[25] J. E. Hirsch, Spin Hall Effect, Phys. Rev. Lett. **83**, 1834 (1999).

[26] Y. K. Kato, R. C. Myers, A. C. Gossard, and D. D. Awschalom, Observation of the Spin Hall Effect in Semiconductors, Science **306**, 1910 (2004).

[27] J. Wunderlich, B. Kästner, J. Sinova, and T. Jungwirth, Experimental Observation of the Spin-Hall Effect in a Two-Dimensional Spin-Orbit Coupled Semiconductor System, Phys. Rev. Lett. **94**, (2005).

[28] S. O. Valenzuela and M. Tinkham, Direct electronic measurement of the spin Hall effect, Nature **442**, 176 (2006).

[29] T. Kimura, Y. Otani, T. Sato, S. Takahashi, and S. Maekawa, Room-Temperature Reversible Spin Hall Effect, Phys. Rev. Lett. **98**, 249901 (2007).

[30] Q. Shao et al., Roadmap of Spin–Orbit Torques, IEEE Trans. Magn. **57**, 1 (2021).

[31] I. M. Miron, K. Garello, G. Gaudin, P.-J. Zermatten, M. V. Costache, S. Auffret, S. Bandiera, B. Rodmacq, A. Schuhl, and P. Gambardella, Perpendicular switching of a single ferromagnetic layer induced by in-plane current injection, Nature **476**, 189 (2011).

[32] L. Liu, C.-F. Pai, Y. Li, H. W. Tseng, D. C. Ralph, and R. A. Buhrman, Spin-Torque Switching with the Giant Spin Hall Effect of Tantalum, Science **336**, 555 (2012).

[33] M. Alghamdi, M. Lohmann, J. Li, P. R. Jothi, Q. Shao, M. Aldosary, T. Su, B. P. T. Fokwa, and J. Shi, Highly Efficient Spin–Orbit Torque and Switching of Layered Ferromagnet Fe_3GeTe_2, Nano Lett. **19**, 4400 (2019).

[34] X. Wang et al., Current-driven magnetization switching in a van der Waals ferromagnet Fe_3GeTe_2, Sci. Adv. **5**, eaaw8904 (2019).

[35] H. Nakayama et al., Spin Hall Magnetoresistance Induced by a Nonequilibrium Proximity Effect, Phys. Rev. Lett. **110**, 206601 (2013).

[36] C. Kittel, On the Theory of Ferromagnetic Resonance Absorption, Phys. Rev. **73**, 155 (1948).

[37] H. Suhl, Ferromagnetic Resonance in Nickel Ferrite Between One and Two Kilomegacycles, Phys. Rev. **97**, 555 (1955).

[38] Y. Tserkovnyak and A. Brataas, Enhanced Gilbert Damping in Thin Ferromagnetic Films, Phys. Rev. Lett. **88**, 117601 (2002).

[39] S. Mizukami, Y. Ando, and T. Miyazaki, Effect of spin diffusion on Gilbert damping for a very thin permalloy layer in Cu/permalloy/Cu/Pt films, Phys. Rev. B **66**, 104413 (2002).

[40] E. Saitoh, M. Ueda, H. Miyajima, and G. Tatara, Conversion of spin current into charge current at room temperature: Inverse spin-Hall effect, Appl. Phys. Lett. **88**, 182509 (2006).

[41] K. Uchida, S. Takahashi, K. Harii, J. Ieda, W. Koshibae, K. Ando, S. Maekawa, and E. Saitoh, Observation of the spin Seebeck effect, Nature **455**, 778 (2008).

[42] J. Li et al., Spin current from sub-terahertz-generated antiferromagnetic magnons, Nature **578**, 70 (2020).

[43] W. Yuan, J. Li, and J. Shi, Spin current generation and detection in uniaxial antiferromagnetic insulators, Appl. Phys. Lett. **117**, 100501 (2020).

[44] Y. Wang et al., Magnetization switching by magnon-mediated spin torque through an antiferromagnetic insulator, Science **366**, 1125 (2019).

[45] S. Datta and B. Das, Electronic analog of the electro-optic modulator, Appl. Phys. Lett. **56**, 665 (1990).

[46] S. S. P. Parkin, M. Hayashi, and L. Thomas, Magnetic Domain-Wall Racetrack Memory, Science **320**, 190 (2008).

[47] S. Parkin and S.-H. Yang, Memory on the racetrack, Nat. Nanotechnol. **10**, 195 (2015).

[48] I. Žutić, A. Matos-Abiague, B. Scharf, H. Dery, and K. Belashchenko, Proximitized materials, Mater. Today **22**, 85 (2019).

[49] M. Alghamdi, P. R. Jothi, W.-C. Liao, S. Coh, X. Lin, B. P. T. Fokwa, and J. Shi, Layer-dependence study of two-dimensional ferromagnets: Fe_3GeTe_2 and $Fe_5Ge_2Te_2$, Appl. Phys. Lett. **124**, 192404 (2024).

[50] N. Nagaosa, J. Sinova, S. Onoda, A. H. MacDonald, and N. P. Ong, Anomalous Hall effect, Rev. Mod. Phys. **82**, 1539 (2010).

[51] J. Smit, The spontaneous hall effect in ferromagnetics I, Physica **21**, 877 (1955).

[52] J. Smit, The spontaneous hall effect in ferromagnetics II, Physica **24**, 39 (1958).

[53] L. Berger, Side-Jump Mechanism for the Hall Effect of Ferromagnets, Phys. Rev. B **2**, 4559 (1970).

[54] R. Karplus and J. M. Luttinger, Hall Effect in Ferromagnetics, Phys. Rev. **95**, 1154 (1954).

[55] K. Kim et al., Large anomalous Hall current induced by topological nodal lines in a ferromagnetic van der Waals semimetal, Nat. Mater. **17**, 794 (2018).

[56] T. Miyasato, N. Abe, T. Fujii, A. Asamitsu, S. Onoda, Y. Onose, N. Nagaosa, and Y. Tokura, Crossover Behavior of the Anomalous Hall Effect and Anomalous Nernst Effect in Itinerant Ferromagnets, Phys. Rev. Lett. **99**, 086602 (2007).

[57] T. Fukumura, H. Toyosaki, K. Ueno, M. Nakano, T. Yamasaki, and M. Kawasaki, A Scaling Relation of Anomalous Hall Effect in Ferromagnetic Semiconductors and Metals, Jpn. J. Appl. Phys. **46**, L642 (2007).

[58] H. Chen, Q. Niu, and A. H. MacDonald, Anomalous Hall Effect Arising from Noncollinear Antiferromagnetism, Phys. Rev. Lett. **112**, 017205 (2014).

[59] S. Nakatsuji, N. Kiyohara, and T. Higo, Large anomalous Hall effect in a non-collinear antiferromagnet at room temperature, Nature **527**, 212 (2015).

[60] A. K. Nayak et al., Large anomalous Hall effect driven by a nonvanishing Berry curvature in the noncolinear antiferromagnet Mn_3Ge, Sci. Adv. **2**, e1501870 (2016).

[61] Y. Zhang, Y. Sun, H. Yang, J. Železný, S. P. P. Parkin, C. Felser, and B. Yan, Strong anisotropic anomalous Hall effect and spin Hall effect in the chiral antiferromagnetic compounds Mn_3X (X = Ge, Sn, Ga, Ir, Rh, and Pt), Phys. Rev. B **95**, 075128 (2017).

[62] M. Ikhlas, T. Tomita, T. Koretsune, M.-T. Suzuki, D. Nishio-Hamane, R. Arita, Y. Otani, and S. Nakatsuji, Large anomalous Nernst effect at room temperature in a chiral antiferromagnet, Nat. Phys. **13**, 1085 (2017).

[63] H. Yang, Y. Sun, Y. Zhang, W.-J. Shi, S. S. P. Parkin, and B. Yan, Topological Weyl semimetals in the chiral antiferromagnetic materials Mn_3Ge and Mn_3Sn, New J. Phys. **19**, 015008 (2017).

[64] L. Šmejkal, R. González-Hernández, T. Jungwirth, and J. Sinova, Crystal time-reversal symmetry breaking and spontaneous Hall effect in collinear antiferromagnets, Sci. Adv. **6**, eaaz8809 (2020).

[65] Z. Feng et al., An anomalous Hall effect in altermagnetic ruthenium dioxide, Nat. Electron. **5**, 735 (2022).

[66] L. Šmejkal, A. H. MacDonald, J. Sinova, S. Nakatsuji, and T. Jungwirth, Anomalous Hall antiferromagnets, Nat. Rev. Mater. **7**, 482 (2022).

[67] H. Tan, Y. Liu, and B. Yan, Unconventional anomalous Hall effect from magnetization parallel to the electric field, Phys. Rev. B **103**, 214438 (2021).

[68] J. Zhou et al., Heterodimensional superlattice with in-plane anomalous Hall effect, Nature **609**, 46 (2022).

[69] C.-Z. Chang, C.-X. Liu, and A. H. MacDonald, Colloquium: Quantum anomalous Hall effect, Rev. Mod. Phys. **95**, 011002 (2023).

[70] C.-Z. Chang et al., Experimental Observation of the Quantum Anomalous Hall Effect in a Magnetic Topological Insulator, Science **340**, 167 (2013).

[71] Y. Deng, Y. Yu, M. Z. Shi, Z. Guo, Z. Xu, J. Wang, X. H. Chen, and Y. Zhang, Quantum anomalous Hall effect in intrinsic magnetic topological insulator $MnBi_2Te_4$, Science **367**, 895 (2020).

[72] M. Serlin, C. L. Tschirhart, H. Polshyn, Y. Zhang, J. Zhu, K. Watanabe, T. Taniguchi, L. Balents, and A. F. Young, Intrinsic quantized anomalous Hall effect in a moiré heterostructure, Science **367**, 900 (2020).

[73] T. Li et al., Quantum anomalous Hall effect from intertwined moiré bands, Nature **600**, 641 (2021).

[74] A. Neubauer, C. Pfleiderer, B. Binz, A. Rosch, R. Ritz, P. G. Niklowitz, and P. Böni, Topological Hall Effect in the *A* Phase of MnSi, Phys. Rev. Lett. **102**, 186602 (2009).

[75] N. Kanazawa, Y. Onose, T. Arima, D. Okuyama, S. Wakimoto, K. Kakurai, S. Ishiwata, and Y. Tokura, Large Topological Hall Effect in a Short-Period Helimagnet MnGe, Phys. Rev. Lett. **106**, 156603 (2011).

[76] Z. Qiao, S. A. Yang, W. Feng, W.-K. Tse, J. Ding, Y. Yao, J. Wang, and Q. Niu, Quantum anomalous Hall effect in graphene from Rashba and exchange effects, Phys. Rev. B **82**, 161414 (2010).

[77] S. Y. Huang, X. Fan, D. Qu, Y. P. Chen, W. G. Wang, J. Wu, T. Y. Chen, J. Q. Xiao, and C. L. Chien, Transport Magnetic Proximity Effects in Platinum, Phys. Rev. Lett. **109**, 107204 (2012).

[78] Y. M. Lu, Y. Choi, C. M. Ortega, X. M. Cheng, J. W. Cai, S. Y. Huang, L. Sun, and C. L. Chien, Pt Magnetic Polarization on $Y_3Fe_5O_{12}$ and Magnetotransport Characteristics, Phys. Rev. Lett. **110**, 147207 (2013).

[79] Q. Shao et al., Exploring interfacial exchange coupling and sublattice effect in heavy metal/ferrimagnetic insulator heterostructures using Hall measurements, x-ray magnetic circular dichroism, and neutron reflectometry, Phys. Rev. B **99**, 104401 (2019).

[80] J.-U. Lee, S. Lee, J. H. Ryoo, S. Kang, T. Y. Kim, P. Kim, C.-H. Park, J.-G. Park, and H. Cheong, Ising-Type Magnetic Ordering in Atomically Thin $FePS_3$, Nano Lett. **16**, 7433 (2016).

[81] C. Gong et al., Discovery of intrinsic ferromagnetism in two-dimensional van der Waals crystals, Nature **546**, 265 (2017).

[82] B. Huang et al., Layer-dependent ferromagnetism in a van der Waals crystal down to the monolayer limit, Nature **546**, 270 (2017).

[83] M. Bonilla, S. Kolekar, Y. Ma, H. C. Diaz, V. Kalappattil, R. Das, T. Eggers, H. R. Gutierrez, M.-H. Phan, and M. Batzill, Strong room-temperature ferromagnetism in VSe_2 monolayers on van der Waals substrates, Nat. Nanotechnol. **13**, 289 (2018).

[84] Z. Fei et al., Two-dimensional itinerant ferromagnetism in atomically thin Fe_3GeTe_2, Nat. Mater. **17**, 778 (2018).

[85] M. Lohmann et al., Probing Magnetism in Insulating $Cr_2Ge_2Te_6$ by Induced Anomalous Hall Effect in Pt, Nano Lett. **19**, 2397 (2019).

[86] T. Su et al., Current-induced CrI_3 surface spin-flop transition probed by proximity magnetoresistance in Pt, 2D Mater. **7**, 045006 (2020).

[87] Y. Zhang, Y.-W. Tan, H. L. Stormer, and P. Kim, Experimental observation of the quantum Hall effect and Berry's phase in graphene, Nature **438**, 201 (2005).

[88] Y. Yao, F. Ye, X.-L. Qi, S.-C. Zhang, and Z. Fang, Spin-orbit gap of graphene: First-principles calculations, Phys. Rev. B **75**, 041401 (2007).

[89] M. Gmitra, S. Konschuh, C. Ertler, C. Ambrosch-Draxl, and J. Fabian, Band-structure topologies of graphene: Spin-orbit coupling effects from first principles, Phys. Rev. B **80**, 235431 (2009).

[90] C. L. Kane and E. J. Mele, Quantum Spin Hall Effect in Graphene, Phys. Rev. Lett. **95**, 226801 (2005).

[91] F. D. M. Haldane, Model for a Quantum Hall Effect without Landau Levels: Condensed-Matter Realization of the "Parity Anomaly," Phys. Rev. Lett. **61**, 2015 (1988).

[92] Z. Qiao, W. Ren, H. Chen, L. Bellaiche, Z. Zhang, A. H. MacDonald, and Q. Niu, Quantum Anomalous Hall Effect in Graphene Proximity Coupled to an Antiferromagnetic Insulator, Phys. Rev. Lett. **112**, 116404 (2014).

[93] H. Takenaka, S. Sandhoefner, A. A. Kovalev, and E. Y. Tsymbal, Magnetoelectric control of topological phases in graphene, Phys. Rev. B **100**, 125156 (2019).

[94] Z. Wang, C. Tang, R. Sachs, Y. Barlas, and J. Shi, Proximity-Induced Ferromagnetism in Graphene Revealed by the Anomalous Hall Effect, Phys. Rev. Lett. **114**, 016603 (2015).

[95] P. Wei et al., Strong interfacial exchange field in the graphene/EuS heterostructure, Nat. Mater. **15**, 711 (2016).

[96] Y.-F. Wu et al., Magnetic proximity effect in graphene coupled to a $BiFeO_3$ nanoplate, Phys. Rev. B **95**, 195426 (2017).

[97] D. V. Averyanov, I. S. Sokolov, A. M. Tokmachev, O. E. Parfenov, I. A. Karateev, A. N. Taldenkov, and V. G. Storchak, High-Temperature Magnetism in Graphene Induced by Proximity to EuO, ACS Appl. Mater. Interfaces **10**, 20767 (2018).

[98] H. Yang, M. Gobbi, F. Herling, V. T. Pham, F. Calavalle, B. Martín-García, A. Fert, L. E. Hueso, and F. Casanova, A seamless graphene spin valve based on proximity to van der Waals magnet $Cr_2Ge_2Te_6$, Nat. Electron. **8**, 15 (2025).

[99] C. Tang, Z. Zhang, S. Lai, Q. Tan, and W. Gao, Magnetic Proximity Effect in Graphene/$CrBr_3$ van der Waals Heterostructures, Adv. Mater. **32**, 1908498 (2020).

[100] I. Vobornik, U. Manju, J. Fujii, F. Borgatti, P. Torelli, D. Krizmancic, Y. S. Hor, R. J. Cava, and G. Panaccione, Magnetic Proximity Effect as a Pathway to Spintronic Applications of Topological Insulators, Nano Lett. **11**, 4079 (2011).

[101] M. Lang et al., Proximity Induced High-Temperature Magnetic Order in Topological Insulator - Ferrimagnetic Insulator Heterostructure, Nano Lett. **14**, 3459 (2014).

[102] F. Katmis et al., A high-temperature ferromagnetic topological insulating phase by proximity coupling, Nature **533**, 513 (2016).

[103] C. Tang et al., Above 400-K robust perpendicular ferromagnetic phase in a topological insulator, Sci. Adv. **3**, e1700307 (2017).

[104] A. A. Soluyanov, D. Gresch, Z. Wang, Q. Wu, M. Troyer, X. Dai, and B. A. Bernevig, Type-II Weyl semimetals, Nature **527**, 495 (2015).

[105] P. Li, Y. Wen, X. He, Q. Zhang, C. Xia, Z.-M. Yu, S. A. Yang, Z. Zhu, H. N. Alshareef, and X.-X. Zhang, Evidence for topological type-II Weyl semimetal WTe2, Nat. Commun. **8**, 2150 (2017).

[106] S. Tang et al., Quantum spin Hall state in monolayer 1T'-WTe_2, Nat. Phys. **13**, 683 (2017).

[107] S. Wu, V. Fatemi, Q. D. Gibson, K. Watanabe, T. Taniguchi, R. J. Cava, and P. Jarillo-Herrero, Observation of the quantum spin Hall effect up to 100 kelvin in a monolayer crystal, Science **359**, 76 (2018).

[108] Y. Shi et al., Imaging quantum spin Hall edges in monolayer WTe_2, Sci. Adv. **5**, eaat8799 (2019).

[109] W. Zhao et al., Magnetic proximity and nonreciprocal current switching in a monolayer WTe_2 helical edge, Nat. Mater. **19**, 503 (2020).

[110] J. Li et al., Proximity-magnetized quantum spin Hall insulator: monolayer 1 T' $WTe_2/Cr_2Ge_2Te_6$, Nat. Commun. **13**, 5134 (2022).

[111] Y.-T. Chen, S. Takahashi, H. Nakayama, M. Althammer, S. T. B. Goennenwein, E. Saitoh, and G. E. W. Bauer, Theory of spin Hall magnetoresistance, Phys. Rev. B **87**, 144411 (2013).

[112] M. Althammer et al., Quantitative study of the spin Hall magnetoresistance in ferromagnetic insulator/normal metal hybrids, Phys. Rev. B **87**, 224401 (2013).

[113] M. Isasa, A. Bedoya-Pinto, S. Vélez, F. Golmar, F. Sánchez, L. E. Hueso, J. Fontcuberta, and F. Casanova, Spin Hall magnetoresistance at $Pt/CoFe_2O_4$ interfaces and texture effects, Appl. Phys. Lett. **105**, 142402 (2014).

[114] C. O. Avci, K. Garello, A. Ghosh, M. Gabureac, S. F. Alvarado, and P. Gambardella, Unidirectional spin Hall magnetoresistance in ferromagnet/normal metal bilayers, Nat. Phys. **11**, 570 (2015).

[115] J. Fischer et al., Spin Hall magnetoresistance in antiferromagnet/heavy-metal heterostructures, Phys. Rev. B **97**, 014417 (2018).

[116] R. Lebrun et al., Anisotropies and magnetic phase transitions in insulating antiferromagnets determined by a Spin-Hall magnetoresistance probe, Commun. Phys. **2**, 50 (2019).

[117] H. Liu, H. Zhang, J. Keagy, Q. Gao, L. Li, J. Li, R. Cheng, and J. Shi, Anisotropic field suppression of Morin transition temperature in epitaxially grown hematite thin films, Phys. Rev. Mater. **9**, 034410 (2025).

[118] J. Nogués, J. Sort, V. Langlais, V. Skumryev, S. Suriñach, J. S. Muñoz, and M. D. Baró, Exchange bias in nanostructures, Phys. Rep. **422**, 65 (2005).

[119] P. K. Manna and S. M. Yusuf, Two interface effects: Exchange bias and magnetic proximity, Phys. Rep. **535**, 61 (2014).

[120] L. Néel, *Magnetism and the Local Molecular Field*, in *Nobel Lectures Physics 1963-1970*, edited by Elsevier (1972).

[121] W. H. Meiklejohn and C. P. Bean, New Magnetic Anisotropy, Phys. Rev. **102**, 1413 (1956).

[122] T. Jungwirth, X. Marti, P. Wadley, and J. Wunderlich, Antiferromagnetic spintronics, Nat. Nanotechnol. **11**, 231 (2016).

[123] V. Baltz, A. Manchon, M. Tsoi, T. Moriyama, T. Ono, and Y. Tserkovnyak, Antiferromagnetic spintronics, Rev. Mod. Phys. **90**, 015005 (2018).

[124] S. M. Rezende, A. Azevedo, and R. L. Rodríguez-Suárez, Introduction to antiferromagnetic magnons, J. Appl. Phys. **126**, 151101 (2019).

[125] J. Han, R. Cheng, L. Liu, H. Ohno, and S. Fukami, Coherent antiferromagnetic spintronics, Nat. Mater. **22**, 684 (2023).

[126] J. Železný, H. Gao, K. Výborný, J. Zemen, J. Mašek, A. Manchon, J. Wunderlich, J. Sinova, and T. Jungwirth, Relativistic Néel-Order Fields Induced by Electrical Current in Antiferromagnets, Phys. Rev. Lett. **113**, 157201 (2014).

[127] P. Wadley et al., Electrical switching of an antiferromagnet, Science **351**, 587 (2016).

[128] S. Y. Bodnar, L. Šmejkal, I. Turek, T. Jungwirth, O. Gomonay, J. Sinova, A. A. Sapozhnik, H.-J. Elmers, M. Kläui, and M. Jourdan, Writing and reading antiferromagnetic Mn_2Au by Néel spin-orbit torques and large anisotropic magnetoresistance, Nat. Commun. **9**, 348 (2018).

[129] M. Meinert, D. Graulich, and T. Matalla-Wagner, Electrical Switching of Antiferromagnetic Mn_2Au and the Role of Thermal Activation, Phys. Rev. Appl. **9**, 064040 (2018).

[130] X. Z. Chen et al., Antidamping-Torque-Induced Switching in Biaxial Antiferromagnetic Insulators, Phys. Rev. Lett. **120**, 207204 (2018).

[131] I. Gray et al., Spin Seebeck Imaging of Spin-Torque Switching in Antiferromagnetic Pt/NiO Heterostructures, Phys. Rev. X **9**, 041016 (2019).

[132] Y. Cheng, S. Yu, M. Zhu, J. Hwang, and F. Yang, Electrical Switching of Tristate Antiferromagnetic Néel Order in $\alpha - Fe_2O_3$ Epitaxial Films, Phys. Rev. Lett. **124**, 027202 (2020).

[133] C. C. Chiang, S. Y. Huang, D. Qu, P. H. Wu, and C. L. Chien, Absence of Evidence of Electrical Switching of the Antiferromagnetic Néel Vector, Phys. Rev. Lett. **123**, 227203 (2019).

[134] R. Lebrun, A. Ross, S. A. Bender, A. Qaiumzadeh, L. Baldrati, J. Cramer, A. Brataas, R. A. Duine, and M. Kläui, Tunable long-distance spin transport in a crystalline antiferromagnetic iron oxide, Nature **561**, 222 (2018).

[135] W. Yuan et al., Experimental signatures of spin superfluid ground state in canted antiferromagnet Cr_2O_3 via nonlocal spin transport, Sci. Adv. **4**, eaat1098 (2018).

[136] R. Cheng, J. Xiao, Q. Niu, and A. Brataas, Spin Pumping and Spin-Transfer Torques in Antiferromagnets, Phys. Rev. Lett. **113**, 057601 (2014).

[137] P. Vaidya, S. A. Morley, J. Van Tol, Y. Liu, R. Cheng, A. Brataas, D. Lederman, and E. Del Barco, Subterahertz spin pumping from an insulating antiferromagnet, Science **368**, 160 (2020).

[138] N. A. Hill, Why Are There so Few Magnetic Ferroelectrics?, J. Phys. Chem. B **104**, 6694 (2000).

[139] M. Fiebig, Revival of the magnetoelectric effect, J. Phys. Appl. Phys. **38**, R123 (2005).

[140] W. Eerenstein, N. D. Mathur, and J. F. Scott, Multiferroic and magnetoelectric materials, Nature **442**, 759 (2006).

[141] I. E. Dzyaloshinskii, On the magneto-electrical effects in antiferromagnets, Sov. Phys. JETP **10**, 628 (1960).

[142] D. N. Astrov, The Magnetoelectric Effect in Antiferromagnetics, Sov. Phys. JETP **11**, 708 (1960).

[143] D. N. Astrov, Magnetoelectric Effect in Chromium Oxide, Sov. Phys. JETP **13**, 729 (1961).

[144] T. J. Martin and J. C. Anderson, Magneto-electric annealing effects of Cr_2O_3, Phys. Lett. **11**, 109 (1964).

[145] T. Martin and J. Anderson, Antiferromagnetic domain switching in Cr_2O_3, IEEE Trans. Magn. **2**, 446 (1966).

[146] P. Borisov, A. Hochstrat, X. Chen, W. Kleemann, and C. Binek, Magnetoelectric Switching of Exchange Bias, Phys. Rev. Lett. **94**, 117203 (2005).

[147] X. He, Y. Wang, N. Wu, A. N. Caruso, E. Vescovo, K. D. Belashchenko, P. A. Dowben, and C. Binek, Robust isothermal electric control of exchange bias at room temperature, Nat. Mater. **9**, 579 (2010).

[148] T. Ashida, M. Oida, N. Shimomura, T. Nozaki, T. Shibata, and M. Sahashi, Isothermal electric switching of magnetization in Cr_2O_3/Co thin film system, Appl. Phys. Lett. **106**, 132407 (2015).

[149] T. Kosub et al., Purely antiferromagnetic magnetoelectric random access memory, Nat. Commun. **8**, 13985 (2017).

[150] W.-C. Liao, H. Liu, W. Tan, J. Keagy, J. Chen, and J. Shi, Electrical Detection of Single-Domain Néel Vector Reorientation across the Spin–Flop Transition in Cr_2O_3 Crystals, Nano Lett. **25**, 9794 (2025).

[151] F. B. Anderson, Statistical Mechanics and Field-Induced Phase Transitions of the Heisenberg Antiferromagnet, Phys. Rev. **136**, A1068 (1964).

[152] A. N. Bogdanov, A. V. Zhuravlev, and U. K. Rößler, Spin-flop transition in uniaxial antiferromagnets: Magnetic phases, reorientation effects, and multidomain states, Phys. Rev. B **75**, 094425 (2007).

[153] L. Landau and E. Lifshits, ON THE THEORY OF THE DISPERSION OF MAGNETIC PERMEABILITY IN FERROMAGNETIC BODIES, Phys. Zeitsch. der Sow. **8**, 153 (1935).

[154] T. L. Gilbert, A phenomenological theory of damping in ferromagnetic materials, IEEE Trans. Magn. **40**, 3443 (2004).

[155] R. Cheng, D. Xiao, and A. Brataas, Terahertz Antiferromagnetic Spin Hall Nano-Oscillator, Phys. Rev. Lett. **116**, 207603 (2016).

[156] C. Kittel, Theory of Antiferromagnetic Resonance, Phys. Rev. **82**, 565 (1951).

[157] F. Keffer and C. Kittel, Theory of Antiferromagnetic Resonance, Phys. Rev. **85**, 329 (1952).

[158] V. Lauter-Pasyuk, H. J. Lauter, B. P. Toperverg, L. Romashev, and V. Ustinov, Transverse and Lateral Structure of the Spin-Flop Phase in FeCr Antiferromagnetic Superlattices, Phys. Rev. Lett. **89**, 167203 (2002).

[159] A. Zheludev, E. Ressouche, I. Tsukada, T. Masuda, and K. Uchinokura, Structure of multiple spin-flop states in $BaCu_2Si_2O_7$, Phys. Rev. B **65**, 174416 (2002).

[160] N. Qureshi, M. Valldor, L. Weber, A. Senyshyn, Y. Sidis, and M. Braden, Magnetic spin-flop transition and interlayer spin-wave dispersion in $PrCaFeO_4$ revealed by neutron diffraction and inelastic neutron scattering, Phys. Rev. B **91**, 224402 (2015).

[161] G. Gitgeatpong, Y. Zhao, P. Piyawongwatthana, Y. Qiu, L. W. Harriger, N. P. Butch, T. J. Sato, and K. Matan, Nonreciprocal Magnons and Symmetry-Breaking in the Noncentrosymmetric Antiferromagnet, Phys. Rev. Lett. **119**, 047201 (2017).

[162] J. Nogués, L. Morellon, C. Leighton, M. R. Ibarra, and I. K. Schuller, Antiferromagnetic spin flop and exchange bias, Phys. Rev. B **61**, R6455 (2000).

[163] M. Wang et al., Spin flop and crystalline anisotropic magnetoresistance in CuMnAs, Phys. Rev. B **101**, 094429 (2020).

[164] Y.-H. Zhang, T.-C. Chuang, D. Qu, and S.-Y. Huang, Detection and manipulation of the antiferromagnetic Néel vector in Cr_2O_3, Phys. Rev. B **105**, 094442 (2022).

[165] S. Foner, High-Field Antiferromagnetic Resonance in Cr_2O_3, Phys. Rev. **130**, 183 (1963).

[166] S. M. Wu, W. Zhang, A. Kc, P. Borisov, J. E. Pearson, J. S. Jiang, D. Lederman, A. Hoffmann, and A. Bhattacharya, Antiferromagnetic Spin Seebeck Effect, Phys. Rev. Lett. **116**, 097204 (2016).

[167] D. Reitz, J. Li, W. Yuan, J. Shi, and Y. Tserkovnyak, Spin Seebeck effect near the antiferromagnetic spin-flop transition, Phys. Rev. B **102**, 020408 (2020).

[168] J. Li, H. T. Simensen, D. Reitz, Q. Sun, W. Yuan, C. Li, Y. Tserkovnyak, A. Brataas, and J. Shi, Observation of Magnon Polarons in a Uniaxial Antiferromagnetic Insulator, Phys. Rev. Lett. **125**, 217201 (2020).

[169] J. Keagy, H. Liu, J. Tang, W. Tan, W. Yuan, S. Mahesh, R. Cheng, and J. Shi, Disorder-induced suppression of antiferromagnetic magnon transport in Cr_2O_3, Phys. Rev. Appl. **24**, L011005 (2025).

[170] N. Vlietstra, J. Shan, V. Castel, B. J. van Wees, and J. Ben Youssef, Spin-Hall magnetoresistance in platinum on yttrium iron garnet: Dependence on platinum thickness and in-plane/out-of-plane magnetization, Phys. Rev. B **87**, 184421 (2013).

[171] K. L. Dudko, V. V. Eremenko, and L. M. Semenenko, Magnetostriction of Antiferromagnetic Cr_2O_3 in Strong Magnetic Fields, Phys. Status Solidi B **43**, 471 (1971).

[172] V. V. Eremenko and V. A. Sirenko, *Magnetostriction and Spin-Flopping of Uniaxially Compressed Antiferromagnets*, in *Modern Trends in Magnetostriction Study and Application*, edited by M. R. J. Gibbs (Springer Netherlands, Dordrecht, 2001), pp. 223–247.

[173] A. Mahmood et al., Voltage controlled Néel vector rotation in zero magnetic field, Nat. Commun. **12**, 1674 (2021).

[174] K. Ujimoto, H. Sameshima, K. Toyoki, Y. Kotani, T. Moriyama, K. Nakamura, R. Nakatani, and Y. Shiratsuchi, Direct observation of antiferromagnetic domains and field-induced reversal in $Pt/Cr_2O_3/Pt$ epitaxial trilayers, Appl. Phys. Lett. **123**, 022407 (2023).

[175] T. Moriyama, Y. Shiratsuchi, T. Iino, H. Aono, M. Suzuki, T. Nakamura, Y. Kotani, R. Nakatani, K. Nakamura, and T. Ono, Giant Anomalous Hall Conductivity at the Pt/Cr_2O_3 Interface, Phys. Rev. Appl. **13**, 034052 (2020).

[176] Y. Ji, J. Miao, K. K. Meng, Z. Y. Ren, B. W. Dong, X. G. Xu, Y. Wu, and Y. Jiang, Spin Hall magnetoresistance in an antiferromagnetic magnetoelectric Cr_2O_3/heavy-metal W heterostructure, Appl. Phys. Lett. **110**, 262401 (2017).

[177] Y. Ji, J. Miao, Y. M. Zhu, K. K. Meng, X. G. Xu, J. K. Chen, Y. Wu, and Y. Jiang, Negative spin Hall magnetoresistance in antiferromagnetic Cr_2O_3/Ta bilayer at low temperature region, Appl. Phys. Lett. **112**, 232404 (2018).

[178] R. Schlitz, T. Kosub, A. Thomas, S. Fabretti, K. Nielsch, D. Makarov, and S. T. B. Goennenwein, Evolution of the spin hall magnetoresistance in Cr_2O_3/Pt bilayers close to the Néel temperature, Appl. Phys. Lett. **112**, 132401 (2018).

[179] P. Daniil and E. Cohen, Low field Hall effect magnetometry, J. Appl. Phys. **53**, 8257 (1982).

[180] T. Kosub, M. Kopte, F. Radu, O. G. Schmidt, and D. Makarov, All-Electric Access to the Magnetic-Field-Invariant Magnetization of Antiferromagnets, Phys. Rev. Lett. **115**, 097201 (2015).

[181] P. J. Brown, J. B. Forsyth, and F. Tasset, A study of magnetoelectric domain formation in Cr_2O_3, J. Phys. Condens. Matter **10**, 663 (1998).

[182] L. Fallarino, A. Berger, and C. Binek, Magnetic field induced switching of the antiferromagnetic order parameter in thin films of magnetoelectric chromia, Phys. Rev. B **91**, 054414 (2015).

[183] K. Du, X. Xu, C. Won, K. Wang, S. A. Crooker, S. Rangan, R. Bartynski, and S.-W. Cheong, Topological surface magnetism and Néel vector control in a magnetoelectric antiferromagnet, Npj Quantum Mater. **8**, 1 (2023).

[184] O. V. Pylypovskyi, S. F. Weber, P. Makushko, I. Veremchuk, N. A. Spaldin, and D. Makarov, Surface-Symmetry-Driven Dzyaloshinskii-Moriya Interaction and Canted Ferrimagnetism in Collinear Magnetoelectric Antiferromagnet Cr_2O_3, Phys. Rev. Lett. **132**, 226702 (2024).

[185] X. Wang, K. Toyoki, R. Nakatani, and Y. Shiratsuchi, Magnetic-field and temperature dependence of anomalous Hall effect in Pt/Cr_2O_3/Pt trilayer, AIP Adv. **12**, 035216 (2022).

[186] C. Sürgers, G. Fischer, P. Winkel, and H. v Löhneysen, Large topological Hall effect in the non-collinear phase of an antiferromagnet, Nat. Commun. **5**, 3400 (2014).

[187] Y. Cheng, S. Yu, M. Zhu, J. Hwang, and F. Yang, Evidence of the Topological Hall Effect in Pt/Antiferromagnetic Insulator Bilayers, Phys. Rev. Lett. **123**, 237206 (2019).

[188] Q. Shao, Y. Liu, G. Yu, S. K. Kim, X. Che, C. Tang, Q. L. He, Y. Tserkovnyak, J. Shi, and K. L. Wang, Topological Hall effect at above room temperature in heterostructures composed of a magnetic insulator and a heavy metal, Nat. Electron. **2**, 182 (2019).

[189] V. J. Folen, G. T. Rado, and E. W. Stalder, Anisotropy of the Magnetoelectric Effect in Cr_2O_3, Phys. Rev. Lett. **6**, 607 (1961).

[190] G. T. Rado and V. J. Folen, Observation of the Magnetically Induced Magnetoelectric Effect and Evidence for Antiferromagnetic Domains, Phys. Rev. Lett. **7**, 310 (1961).

[191] K. D. Belashchenko, Equilibrium Magnetization at the Boundary of a Magnetoelectric Antiferromagnet, Phys. Rev. Lett. **105**, 147204 (2010).

[192] T. Ashida, M. Oida, N. Shimomura, T. Nozaki, T. Shibata, and M. Sahashi, Observation of magnetoelectric effect in Cr_2O_3/Pt/Co thin film system, Appl. Phys. Lett. **104**, 152409 (2014).

[193] K. Toyoki, Y. Shiratsuchi, T. Nakamura, C. Mitsumata, S. Harimoto, Y. Takechi, T. Nishimura, H. Nomura, and R. Nakatani, Equilibrium surface magnetization of α-Cr_2O_3 studied through interfacial chromium magnetization in Co/α-Cr_2O_3 layered structures, Appl. Phys. Express **7**, 114201 (2014).

[194] K. Toyoki, Y. Shiratsuchi, A. Kobane, C. Mitsumata, Y. Kotani, T. Nakamura, and R. Nakatani, Magnetoelectric switching of perpendicular exchange bias in Pt/Co/α-Cr_2O_3/Pt stacked films, Appl. Phys. Lett. **106**, 162404 (2015).

[195] Y. Shiratsuchi, K. Toyoki, and R. Nakatani, Magnetoelectric control of antiferromagnetic domain state in Cr_2O_3 thin film, J. Phys. Condens. Matter **33**, 243001 (2021).

[196] E. Bousquet, E. Lelièvre-Berna, N. Qureshi, J.-R. Soh, N. A. Spaldin, A. Urru, X. H. Verbeek, and S. F. Weber, On the sign of the linear magnetoelectric coefficient in Cr_2O_3, J. Phys. Condens. Matter **36**, 155701 (2024).

[197] S. Mugiraneza and A. M. Hallas, Tutorial: a beginner's guide to interpreting magnetic susceptibility data with the Curie-Weiss law, Commun. Phys. **5**, 95 (2022).

[198] A. N. Hong et al., Metal-Mediated Directional Capping of Rod-Packing Metal–Organic Frameworks, Chem. – Eur. J. **28**, e202201576 (2022).

[199] X. He, W. Echtenkamp, and Ch. Binek, Scaling of the Magnetoelectric Effect in Chromia Thin Films, Ferroelectrics **426**, 81 (2012).

[200] J. Lanier, J. Michel, J. Flores, and F. Yang, Robust Biaxial Anisotropy and Switchable Néel Vectors in $LaFeO_3$ Epitaxial Films, Nano Lett. **25**, 4667 (2025).

[201] B. N. Brockhouse, Antiferromagnetic Structure in Cr_2O_3, J. Chem. Phys. **21**, 961 (1953).

[202] Y. Chang, J. Wang, W. Wang, C. Liu, B. You, M. Liu, S. Zheng, M. Shi, C. Lu, and J.-M. Liu, Linear magnetoelectric memory and training effect in the honeycomb antiferromagnet $Co_4Nb_2O_9$, Phys. Rev. B **107**, 014412 (2023).

[203] A. Iyama and T. Kimura, Magnetoelectric hysteresis loops in Cr_2O_3 at room temperature, Phys. Rev. B **87**, 180408 (2013).

[204] P. J. Brown, J. B. Forsyth, and F. Tasset, Precision determination of antiferromagnetic form factors, Phys. B Condens. Matter **267–268**, 215 (1999).

[205] L. L. Tao, Q. Zhang, H. Li, H. J. Zhao, X. Wang, B. Song, E. Y. Tsymbal, and L. Bellaiche, Layer Hall Detection of the Néel Vector in Centrosymmetric Magnetoelectric Antiferromagnets, Phys. Rev. Lett. **133**, 096803 (2024).

[206] J. Mohapatra, J. Fischbacher, M. Gusenbauer, M. Y. Xing, J. Elkins, T. Schrefl, and J. P. Liu, Coercivity limits in nanoscale ferromagnets, Phys. Rev. B **105**, 214431 (2022).

[207] S. Ducharme, V. M. Fridkin, A. V. Bune, S. P. Palto, L. M. Blinov, N. N. Petukhova, and S. G. Yudin, Intrinsic Ferroelectric Coercive Field, Phys. Rev. Lett. **84**, 175 (2000).

[208] J. Shi, S. Tehrani, T. Zhu, Y. F. Zheng, and J.-G. Zhu, Magnetization vortices and anomalous switching in patterned NiFeCo submicron arrays, Appl. Phys. Lett. **74**, 2525 (1999).

[209] C. Liu et al., Electric field control of magnon spin currents in an antiferromagnetic insulator, Sci. Adv. **7**, eabg1669 (2021).

[210] X. J. Lou, Polarization fatigue in ferroelectric thin films and related materials, J. Appl. Phys. **105**, 024101 (2009).

[211] X. J. Lou, M. Zhang, S. A. T. Redfern, and J. F. Scott, Local Phase Decomposition as a Cause of Polarization Fatigue in Ferroelectric Thin Films, Phys. Rev. Lett. **97**, 177601 (2006).

[212] J. F. Scott and M. Dawber, Oxygen-vacancy ordering as a fatigue mechanism in perovskite ferroelectrics, Appl. Phys. Lett. **76**, 3801 (2000).

[213] M. Dawber, K. M. Rabe, and J. F. Scott, Physics of thin-film ferroelectric oxides, Rev. Mod. Phys. **77**, 1083 (2005).

[214] T. Y. Lee et al., Ferroelectric Polarization-Switching Dynamics and Wake-Up Effect in Si-Doped HfO_2, ACS Appl. Mater. Interfaces **11**, 3142 (2019).

[215] P. Jiang, Q. Luo, X. Xu, T. Gong, P. Yuan, Y. Wang, Z. Gao, W. Wei, L. Tai, and H. Lv, Wake-Up Effect in HfO_2-Based Ferroelectric Films, Adv. Electron. Mater. **7**, 2000728 (2021).

[216] W. Zhu, F. He, J. Hayden, Z. Fan, J. I. Yang, J.-P. Maria, and S. Trolier-McKinstry, Wake-Up in $Al_{1-x}B_xN$ Ferroelectric Films, Adv. Electron. Mater. **8**, 2100931 (2022).

[217] J. Íñiguez, First-Principles Approach to Lattice-Mediated Magnetoelectric Effects, Phys. Rev. Lett. **101**, 117201 (2008).

[218] A. Malashevich, S. Coh, I. Souza, and D. Vanderbilt, Full magnetoelectric response of Cr_2O_3 from first principles, Phys. Rev. B **86**, 094430 (2012).

[219] M. Mostovoy, A. Scaramucci, N. A. Spaldin, and K. T. Delaney, Temperature-Dependent Magnetoelectric Effect from First Principles, Phys. Rev. Lett. **105**, 087202 (2010).

[220] K. Toyoki, Y. Shiratsuchi, A. Kobane, S. Harimoto, S. Onoue, H. Nomura, and R. Nakatani, Switching of perpendicular exchange bias in Pt/Co/Pt/α-Cr_2O_3/Pt layered structure using magneto-electric effect, J. Appl. Phys. **117**, 17D902 (2015).

[221] Y. Shiratsuchi, S. Watanabe, S. Yonemura, T. Shibata, and R. Nakatani, Frustration and relaxation of antiferromagnetic domains reversed by magneto-electric field cooling in a Pt/Co/Au/Cr_2O_3/Pt-stacked film, AIP Adv. **8**, 125313 (2018).

[222] Y. Shiratsuchi, K. Toyoki, T. Yiran, H. Aono, and R. Nakatani, Realization of magnetoelectric effect in 50-nm-thick Cr_2O_3 thin film, Appl. Phys. Express **13**, 043003 (2020).

[223] Y. Shiratsuchi, H. Yoshida, Y. Kotani, K. Toyoki, T. V. A. Nguyen, T. Nakamura, and R. Nakatani, Antiferromagnetic domain wall creep driven by magnetoelectric effect, APL Mater. **6**, 121104 (2018).

[224] I. Iino, T. Tada, K. Toyoki, R. Nakatani, and Y. Shiratsuchi, Anomalous Hall effect in Pt/Al-doped Cr_2O_3 epitaxial film, AIP Adv. **13**, 015035 (2023).

[225] Y. Liu, J. Li, and Z. Xu, Temperature dependence of anomalous hall effect in Pt/Cr_2O_3 heterostructure, J. Phys. Conf. Ser. **3030**, 012002 (2025).

[226] S. F. Weber, A. Urru, S. Bhowal, C. Ederer, and N. A. Spaldin, Surface Magnetization in Antiferromagnets: Classification, Example Materials, and Relation to Magnetoelectric Responses, Phys. Rev. X **14**, 021033 (2024).

[227] A. Hrabec, N. A. Porter, A. Wells, M. J. Benitez, G. Burnell, S. McVitie, D. McGrouther, T. A. Moore, and C. H. Marrows, Measuring and tailoring the Dzyaloshinskii-Moriya interaction in perpendicularly magnetized thin films, Phys. Rev. B **90**, 020402 (2014).

[228] E. Ressouche, M. Loire, V. Simonet, R. Ballou, A. Stunault, and A. Wildes, Magnetoelectric $MnPS_3$ as a candidate for ferrotoroidicity, Phys. Rev. B **82**, 100408 (2010).

[229] H. Chu, C. J. Roh, J. O. Island, C. Li, S. Lee, J. Chen, J.-G. Park, A. F. Young, J. S. Lee, and D. Hsieh, Linear Magnetoelectric Phase in Ultrathin $MnPS_3$ Probed by Optical Second Harmonic Generation, Phys. Rev. Lett. **124**, 027601 (2020).

[230] D. J. Goossens, A. R. Wildes, C. Ritter, and T. J. Hicks, Ordering and the nature of the spin flop phase transition in $MnPS_3$, J. Phys. Condens. Matter **12**, 1845 (2000).

[231] G. Long et al., Isolation and Characterization of Few-Layer Manganese Thiophosphite, ACS Nano **11**, 11330 (2017).

[232] G. Long, H. Henck, M. Gibertini, D. Dumcenco, Z. Wang, T. Taniguchi, K. Watanabe, E. Giannini, and A. F. Morpurgo, Persistence of Magnetism in Atomically Thin $MnPS_3$ Crystals, Nano Lett. **20**, 2452 (2020).

[233] A. R. Wildes, B. Roessli, B. Lebech, and K. W. Godfrey, Spin waves and the critical behaviour of the magnetization in $MnPS_3$, J. Phys. Condens. Matter **10**, 6417 (1998).

[234] F. Feringa, J. M. Vink, and B. J. van Wees, Spin-flop transition in the quasi-two-dimensional antiferromagnet $MnPS_3$ detected via thermally generated magnon transport, Phys. Rev. B **106**, 224409 (2022).

[235] M. Nawwar, R. R. Neumann, J. Wen, I. Mertig, A. Mook, and J. P. Heremans, Large thermal Hall effect in $MnPS_3$, Rep. Prog. Phys. **88**, 080503 (2025).

[236] A. Puthirath Balan et al., Identifying the Origin of Thermal Modulation of Exchange Bias in $MnPS_3/Fe_3GeTe_2$ van der Waals Heterostructures, Adv. Mater. **36**, 2403685 (2024).

[237] S. Catalano, J. M. Gomez-Perez, M. X. Aguilar-Pujol, A. Chuvilin, M. Gobbi, L. E. Hueso, and F. Casanova, Spin Hall Magnetoresistance Effect from a Disordered Interface, ACS Appl. Mater. Interfaces **14**, 8598 (2022).

[238] M. N. Ali et al., Large, non-saturating magnetoresistance in WTe_2, Nature **514**, 205 (2014).